Spring 4-30-2019

INTERROGATION OF SPENT NUCLEAR FUEL CASKS USING COSMIC-RAY MUON COMPUTED TOMOGRAPHY

Daniel C. Poulson
University of New Mexico

Daniel Poulson

Candidate

Nuclear Engineering

Department

This dissertation is approved, and it is acceptable in quality and form for publication:

Approved by the Dissertation Committee:

Dr. Adam A. Hecht , Chairperson

Dr. Cassiano R. E. de Oliveira

Dr. Douglas E. Fields

Dr. Christopher L. Morris

INTERROGATION OF SPENT NUCLEAR FUEL CASKS USING COSMIC-RAY MUON COMPUTED TOMOGRAPHY

by

DANIEL POULSON

B.A., Physics, University of Colorado, 2013

DISSERTATION

Submitted in Partial Fulfillment of the
Requirements for the Degree of

Doctor of Philosophy
Engineering

The University of New Mexico
Albuquerque, New Mexico

July, 2019

DEDICATION

This work would never have been accomplished without the constant love and support of my wonderful wife, Gretchen. Thank you for always helping me to keep my drive and direction focused on what matters most, our family. We have grown from just us to include Adele, Eve, and Iyla. I can't wait to see what we do next!

ACKNOWLEDGEMENTS

This work would never have been accomplished without the countless individuals who have positively affected my life including co-workers, friends, and family. My parents and in-laws have been completely supportive throughout this time, and no one has helped me more than my wife. I want to thank them for the moral support that they have given me.

The Los Alamos National Laboratory Threat Reduction Team has been phenomenal to work and perform research with. The leading members Dr. Chris Morris, Dr. Matt Durham, Dr. Elena Guardincerri, and Jeff Bacon have shown me the amazing things that a small group of people can accomplish when they are united and dedicated. My time with them will only have made me more determined to contribute more to the field of applied physics.

I am especially grateful to Dr. Adam Hecht for his patience and willingness to work with me as a distance student. He was always willing to offer new perspectives on the work I was doing, and supportive as I worked my way through the degree requirements. I would not have been able to accomplish this without his advice and direction.

Thank you Dr. Oliveira and Dr. Fields for taking time out from your own responsibilities and research to serve on my committee. I am thankful to have the input from those outside of my immediate research that can lend a new perspective to the work.

INTERROGATION OF SPENT NUCLEAR FUEL CASKS USING COSMIC-RAY MUON COMPUTED TOMOGRAPHY

by

Daniel Poulson

B.A., Physics, University of Colorado, 2013

Ph.D., Engineering, University of New Mexico, 2019

ABSTRACT

Properly accounting and safeguarding spent nuclear fuel are key components in the International Atomic Energy Agency's mission of non-proliferation. Currently, no instruments are deployed that are able to verify the spent nuclear fuel contents of dry storage casks. Cosmic-ray muons provide an ideal probe for the heavily shielded casks due to their ability to penetrate thick, dense materials. Coulombic scattering of the muons, to first order, is proportional to the Z^2/A of the material; this makes it especially sensitive to actinides, such as uranium and plutonium. The combination of these traits allows muons to be used to image and verify the contents of a sealed cask *in situ*.

Here the analysis of the first muon scattering measurements of spent nuclear fuel dry casks is presented, which show a 2.3 σ confidence in the identification of a missing fuel bundle. Geant4 simulations are benchmarked against measurement data and show good agreement. Using the benchmarked simulations, the first study of computed tomography using cosmic-ray muon scattering is presented and further applied to the fingerprinting and monitoring of spent nuclear fuel casks. Finally, the feasibility of using cosmic-ray muons to perform a final verification of spent nuclear fuel-prior to permanent deposition in a geological repository-is investigated.

Contents

List of Figures

List of Tables

Chapter 1

Introduction

As uranium fuel is irradiated in a nuclear reactor, plutonium is produced by neutron capture on ^{238}U, which then undergoes two β decays to produce ^{239}Pu. The concentration of ^{239}Pu increases with time spent in the reactor. Approximately 1% of the initial ^{238}U has typically undergone transmutation to ^{239}Pu by the time the fuel is removed from the reactor core. Spent reactor fuel is then kept in cooling pools for several years, allowing shorter-lived fission products to decay away. After cooling in the water pools, the spent fuel is stored in dry casks. Spent fuel that is stored in dry casks is often kept indefinitely on the same site as the reactor or at an interim storage facility. The plutonium content of spent nuclear fuel can be chemically removed and purified. Once extracted, plutonium can be recycled for use in reactors or radioisotope thermal generators [1–3]. However, extracted plutonium also serves as fissile material for nuclear explosives, making spent nuclear fuel a proliferation risk.

Most nations in the world are signatories to the Treaty on the Non-Proliferation of Nuclear Weapons (NPT) [4]. The NPT divides the signatories into nuclear weapons states and non-weapons states. The five weapons states are those which had manufactured and detonated a nuclear explosive device prior to January 1, 1967: China, France, Russia, the United Kingdom, and the United States. By signing the NPT, weapons states pledged to not directly or indirectly facilitate the transfer of nuclear weapons to non-weapon states or facilitate the acquisition or control of nuclear weapons. Conversely, the non-weapon states pledged to accept safeguards by the

International Atomic Energy Agency (IAEA).

It is the mission of the IAEA to (acting independently of any one nation): assist member states in the use nuclear science and technology for peaceful purposes, develop nuclear safety standards, and verify through inspection that non-weapon states comply with their NPT agreements [5]. To fulfill its mission, the IAEA collects member state's declarations, analyzes open-source data and information, and conducts inspections of nuclear facilities. One aspect of the IAEA inspector's responsibilities is to maintain accountability of the contents inside of spent nuclear fuel casks. This is done by applying tamper-indicating seals to the lids of the casks, which are verified during inspections.

Occasionally, casks seals can be corroded by weather or damaged during the handling of the casks. When this occurs, continuity of knowledge of the cask's contents is lost and requires that the cask be returned to a cooling pool in order to be safely opened and re-verified. The handling, transporting, and opening of the cask are costly, time-consuming, and disruptive to operations at the nuclear facility under inspection. However, the goal of the IAEA is to detect the diversion of significant quantities of nuclear material within certain timeliness goals, as shown in Table 1.1. For this reason, the IAEA lists the development of real-time monitoring of nuclear material in spent fuel casks as one of its developmental goals [6].

Special Nuclear Material	Significant Quantities	Timeliness Goal
Plutonium ($< 80\%$ ^{238}Pu)	8 kg total Pu	Irradiated = 3 months Unirradiated = 1 month
Highly Enriched Uranium ($> 20\%$ ^{235}U)	25 kg ^{235}U	Irradiated = 3 months Unirradiated = 1 month
Low Enriched Uranium ($< 20\%$ ^{235}U) includes depleted (DU) and natural (NU) uranium	725 kg ^{235}U (or 10 t NU or 20 t DU)	12 months

Table 1.1: The timeliness goals for detecting the diversion of a significant quantity of different nuclear materials [7].

The use of neutrons or photons as radiographic probes for storage casks is limited by the heavy shielding used to contain the radiation emitted by the fuel, as well as self-shielding effects from fuel. Previous work was performed that detected thermal neutrons and low energy gamma-rays emanating from spent nuclear fuel dry storage casks; however, it was determined that exiting radiation was mostly scattered and had thus lost any radiographic information [8]. Additional work has also been performed which attempted to "fingerprint" the contents of the casks by comparing the signal from escaping neutrons to that of the same cask at a later date [9, 10]. The neutron fingerprinting method required corrections that accounted for decays of fission products in the fuel—which required knowledge of the fuel burnup— and potentially large variations in the background between measurements at the reactor site and later measurements at an interim storage facility. Simulations using 4 MeV X-rays as an external radiographic probe have also been performed [11]. The simulations showed reasonable results, but the analysis was done neglecting any background or statistical noise. Application of the method would also require the use of a linac X-ray source which would not allow for measurements of the casks *in situ*. Antineutrinos produced by beta-decay of fission products were proposed as an alternative method for monitoring spent fuel [12]. Unfortunately, the required detector would need a mass on the order of 10 tons and counting times on the order of 1 year.

Recently, cosmic-ray muons have been investigated as radiographic probes for dry storage casks, due to their highly penetrating nature [13–21]. In this dissertation work, cosmic-ray muon interrogation of spent nuclear dry casks is presented using both simulation and experimental data. Chapter 2 provides a condensed history of cosmic-ray muon imaging methods and applications. General theoretical principles are presented in Chapter 3, including muon interactions with matter as well as simulation and data analysis methods. Descriptions of the first cosmic-ray muon

experimental measurement campaigns on a dry storage cask at Idaho National Laboratory, data analysis, and simulation benchmarking are presented in Chapter 4. The first application of cosmic-ray muon scattering analysis to computed tomography is presented in Chapter 5. The methodology of cosmic-ray computed tomography is applied to simulation data of dry storage casks containing different fuel burnups in Chapter 6. Finally, the feasibility of using muons to perform a final fuel content verification on spent fuel casks, prior to burial in an underground repository, is shown in Chapter 7. A summary of the work is included in Chapter 8 and recommendations for future work are given in Chapter 9.

Chapter 2

History of Muon Imaging

Cosmic-ray muons were first used as a radiographic probe in the mid-1950s, when E. P. George undertook to measure the overburden of ice and rock above the Guthega-Munyang tunnel using a Geiger counter telescope [22]. A little over a decade later, George's method was improved upon by Louis W. Alverez. Alverez and his colleagues utilized a spark chamber with digital read-outs, which had been developed a few years earlier, to measure the attenuation of muons inside of the Second Pyramid of Giza [23]. Alverez's muon attenuation measurement was benchmarked against simulation in order to provide a thorough search, through 19% of the volume pyramid, for hidden chambers. Latter unpublished work verified that additional measurements had not found any hidden chambers within the Second Pyramid [24].

Decades later, in the mid-1990s, interest in cosmic-ray muon radiography and tomography was rekindled, starting with measurements by Nagamine [25] to measure the internal structure of Mt. Tsukuba with a muon telescope. The methodology proposed by Nagamine was further developed with Tanaka [26], and was used to create the first muon image of a volcano [27]. Tanaka also extended the muon imaging of volcanoes by imaging Mt. Asama with two muon telescopes in order to provide a 3-dimensional tomograph of the volcano's internal structure [28]. Additional geological muon imaging efforts were made by the DIAPHANE project, which used a scintillator muon telescope to make measurements of Mt. Etna in Italy [29]. At the same time, the MU-RAY project developed a scintillator telescope and used it to measure

the internal structure of Mt. Vesuvius [30, 31]. Tanaka and the DIAPHANE project collaborated to obtain a 3-dimensional tomographic image of the Showa-Shinzan lava dome via inversion of muon attenuation and gravimetric data, using a topographic map of the volcano as a prior [32]. A similar inversion method was recently used by the Los Alamos National Laboratory's (LANL) Threat Reduction team to invert muon attenuation data taken from an underground tunnel, but without using any topographical prior. The 3-dimensional reconstructed tomograph contained information about the overhead structure and matched the rock air surface interface obtained by LIDAR measurements (within the resolution of the muon tomograph). The success of geological imaging with muons has led to an emerging interest in the development of borehole muon detectors to be used below ground and will serve to identify geological objects like cavities, mineral deposits, reservoirs, etc [33–35].

Cosmic-ray muon attenuation radiography has also seen a resurgence in measurements of pyramids. In 2013, Aguilar presented preliminary results on data taken on the Pyramid of the Sun at Teotihuacan [36]. A new large scale collaboration effort named ScanPyramids, which involved muon radiography work by Nagoya University, KEK (Japan's high energy physics research institution), and the French Alternative Energies and Atomic Energy Commission (CEA) began imaging the Great Pyramid of Giza in 2015. Nagoya University deployed nuclear emulsions which recorded muon tracks over 238 days in 2 positions, within the pyramid. KEK deployed a scintillator muon telescope in two positions outside of the pyramid, with over a year of overall counting time. The CEA deployed two micro-mesh gas detector muon telescopes in front of the north face of the pyramid, with a counting time of 2 months. The results from the independent analysis of all data found a candidate for an undiscovered corridor and chamber, with confidences between 5-13 σ [37]

During the renaissance of muon attenuation radiography, LANL developed the method of muon scattering radiography [38, 39]. Muon scattering radiography made

use of the multiple coulomb scattering of the muons as they passed through material. The process was well understood and had been applied previously to charged particle radiography with accelerator beams [40–43]. Unlike attenuation radiography, muon scattering radiography required tracking a muon's position and direction in two detectors in order to calculate the scatter that the muon had undergone and the approximate path it had taken. Muon scattering radiography was initially developed as a means of detecting special nuclear material inside of shipping containers. Several groups across the world quickly instigated muon scattering radiography research with drift chambers and drift tubes [44, 45], scintillator detectors [46, 47], gas electron multiplier detectors [48], micro-mesh gas detectors [49], and resistive plate chambers [50].

As research into muon scattering radiography matured, a number of image reconstruction algorithms were proposed and developed. There now exist several muon scattering analysis algorithms; however, most are classified as being variations of the point of closest approach (POCA) method or the maximum likelihood expectation maximization (MLEM) method. POCA algorithms organize muon scattering data by assigning the muon's scatter to a single position in the space between the two muon detectors. This is accomplished by calculating a vector of minimal distance between the incident and exiting muon tracks, bisecting it, and assigning that position as the point in space of the muon's scatter. POCA methods typically diverge in the exact method of calculating the point of closest approach and/or the method of quantifying the scattering data after it has been distributed in space. Some variations of the algorithm are described in [51–54].

MLEM methods also rely on the correlation of incident and exiting muon tracks, but aim to form a most likely path of the muons through the volume between the detectors. This is done by dividing the volume into finite volume elements (voxels) and iteratively solving for their scattering densities so that the likelihood of the recon-

structed muon paths is maximized. MLEM methods are intrinsically more complex than POCA methods, which results in increased computation times for reconstruction solutions. For this reason, MLEM methods are not typically employed for real-time analysis. Some variations of the MLEM algorithm are described in [55–57].

Several applications of scattering muon radiography have been suggested over the last decade and a half. Initially, most applications were related to homeland security and involved scanning cargo containers for fissile materials. Scanning US-bound, seaborne cargo containers was mandated by Congress in 2007 and was scheduled to be fully implemented in 2018 [58]. Much of the initial muon scattering research was devoted to providing passive scanning methods that would help alleviate cargo scanning needs and fulfill the congressional mandate [39, 44, 48, 54, 59, 60].

Soon after the Fukushima accident, both muon attenuation and muon scattering radiography were proposed to image the internal structure of the Fukushima reactors [61–63]. Use of muon detectors would have allowed the deployment of muon tracking detectors outside of reactor buildings in order to monitor the state of the reactors after they went offline. Specifically, the muon images would have produced information about the containment of the melted nuclear fuel; whether or not it had melted through and dropped out of the containment vessel. The LANL Threat Reduction Team performed a measurement on the University of New Mexico's Research Reactor to construct tomographic images of the reactor core as well as the reactor's graphite reflector, lead shielding, and water tank [62]. The measurement by the LANL team indicated that muon scattering radiography could be used as a helpful tool for determining appropriate cleanup procedures in the case of the Fukushima reactors.

Muon scattering radiography was also suggested for use in industrial applications. Recent work by Hu used muon scattering radiography to show that muons could function as an appropriate probe for *in situ* measurements of components of a blast furnace [64]. These results came from measurement on several material samples,

including cores that had been removed from an experimental blast furnace. It was determined that measuring the linear scattering density with cosmic-ray muons was sufficient to discriminate coke and ferrous pellets, as well as image the burden lares in the shaft and the components of the materials in the hearth. Other work by the LANL team demonstrated that muon scattering radiography could be used for *in situ* measurements of valves and pipes [65]. This would be most useful in cases where a scan was needed without shutting down flow through the pipes or if the pipe is well insulated and removal of the insulation would be undesirable. Results indicated that severe corrosion of pipe walls could be identified with an hour of data, while a few hours of data could determine if a valve was open or shut.

Ongoing work by the LANL team has also shown that muon scattering radiography can be used to identify iron rods within a thick concrete wall [66, 67]. The thickness of the concrete and size of the smallest iron rod were chosen to imitate the inside of Brunelleschi's copula that sits atop the Cathedral of Santa Maria del Fiore in Florence. It is unknown if the Florentine cathedral contains iron supports inside, though records show that large quantities of iron were purchased during the construction of the dome. The measurement demonstrated that roughly 20 days of cosmic-ray muon scattering data was sufficient to identify a 2×3 cm^2 cross-section iron bar contained within a 1.73 m thick concrete wall. If the measurement were carried out on Brunelleschi's copula, muon scattering radiography would invaluably provide critical structural information of the dome, thus assisting in the preservation of the historic cathedral.

A third method of using cosmic-ray muons for the identification of fissionable material was also developed at LANL. Rather than measuring the attenuation or scattering of muons through a material, muons that stopped within an object and had a correlated (in time) neutron signal recorded from a scintillating neutron detector were used for analysis. This method was called tagged muon radiography, referring to the correlation/tagging of muons with a neutron signal. The method

was able to use the tagged muon tracks to identify an LEU target's spatial position, without offering composition information [68]. This technique was thought to have pertinent applications to warhead verification in treaty scenarios. Additional work was performed using three uranium cubes which were shielded with 2.5 cm of steel and located 150 cm below a muon tracking detector [69]. The three uranium cubes were correctly located in space using 93 hrs of data.

Muon radiography has undergone rapid expansion and development in the last three decades. Muon attenuation is an important part of geological measurement and survey, with applications to volcanoes, archaeology, and natural resource reservoirs. Muon scattering radiography has a number of applications to cargo scanning and homeland security, nuclear reactor imaging, industry, and interrogating thick concrete structures. Recent work also indicates that neutron tagged muon imaging could serve as a useful aid in treaty verification.

Chapter 3

Theory

Muon tomography and radiography provide the ability to passively image objects or structures with purely background radiation. Cosmic-ray muons are produced at the edge of the atmosphere; they are the daughter products of hadronic showers from impinging extraterrestrial cosmic-rays. The heavier and shorter-lived mesons quickly decay, producing muons and neutrinos which reach the earth's surface. The differential cosmic-ray muon intensity follows an approximately $\cos^2(\theta_z)$ distribution (with θ_z being angle off of the zenith) and is nearly uniform across the azimuth. The integrated flux of cosmic-ray muons at sea level is roughly 1 muon/cm^2/min with a mean momentum of 4 GeV[70]. The constant, uniform bombardment of muons provides an ideal passive probe for radiography.

Muons, like electrons, are leptons which cannot interact via the strong nuclear force and are dominated by electromagnetic interactions as they pass through matter. However, unlike electrons, muons have a mass of 105.6 MeV/c^2 which limits energy loss to bremsstrahlung radiation below momenta of hundreds of GeV. At momenta typical of cosmic-ray muons, muon interactions are dominated by energy loss due to ionization and multiple coulomb scattering. Charged particle imaging techniques are generally categorized into two methods: those that utilize the stopping of particles and those that utilize the scattering of particles [71].

3.1 Muon Stopping

At energies typical of cosmic-ray muons, the stopping power of a muon in a material is described by the Bethe-Bloch equation:

$$\left\langle -\frac{dE}{dx} \right\rangle = \frac{N_A}{4\pi m_e} \left(\frac{e^2}{\epsilon_0 c} \right)^2 z^2 \frac{Z}{A} \frac{1}{\beta} \left[\frac{1}{2} \ln \left(\frac{2m_e c^2 \beta^2 \gamma^2 T_{\max}}{I^2} \right) - \beta^2 - \frac{\delta(\beta\gamma)}{2} \right], \quad (3.1)$$

where N_A is Avagadro's number, m_e is the electron mass, e is the electron charge, ϵ_0 is the vacuum permittivity, c is the speed of light, z is the unit charge of the particle, Z is the atomic number of the material, A is the atomic mass of the material, β and γ are typical relativistic quantities, $T_{\max}$ is the maximum energy that can be transferred in a single collision, I is the mean excitation energy of the material, and δ is a material density correction term.

As indicated by the Bethe-Bloch equation, the mean energy loss of muons or stopping power is (to first order) proportional to the ratio Z/A of the material. The ratio Z/A varies slightly across the periodic table from near 1/2 for light elements to approximately 2/5 for actinides. As shown in Figure 3.1, the energy loss of muons with energy ranges from 1-100 GeV/c is typically $\sim$ 1-2 MeV/g/cm^2 in most materials. It is possible for all of the muon energy to be deposited in the material and for the muon to stop and decay; though, for cosmic-ray muons, it typically would require several meters of material to do so.

When using muon stopping for attenuation radiography, it is assumed that the ratio of the number of muons exiting an object over the number of muons entering an object is given as:

$$\frac{N_o}{N_i} = \exp\left[-\frac{\ell}{\lambda} \right], \quad (3.2)$$

where N_o is the number of muons the exit, N_i is the number of incident muons, ℓ

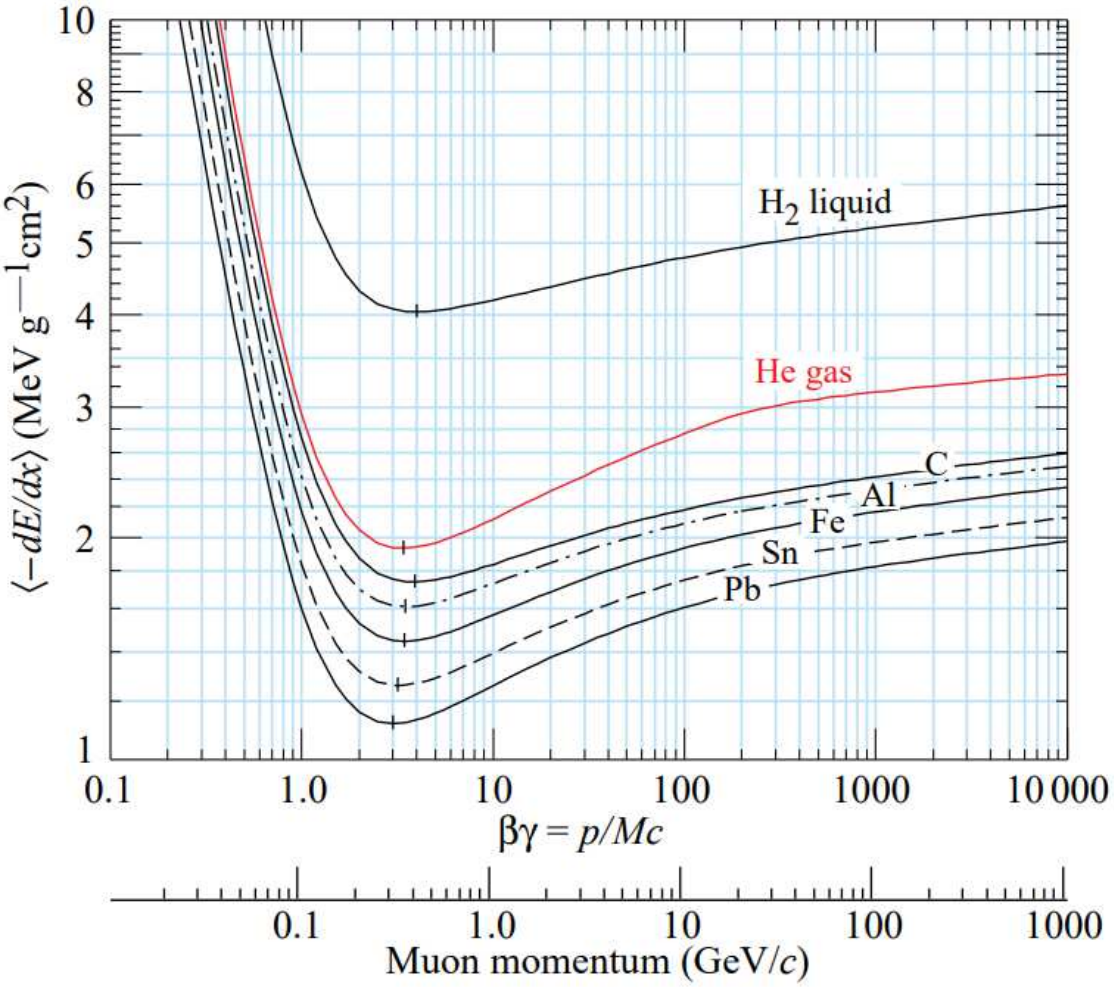

Figure 3.1: The stopping power of muons in different materials over several orders of magnitude of muon momentum[70].

is the distance the muons traverse in the object, and λ is the mean free path of the muons in the material (in terms of stopping). Muon stopping is typically used for imaging large and optically thick (dimensions on the order or greater than λ) objects, including geological and archaeological features. When imaging large volumes, the recorded muon signal is compared against the unimpeded muon signal of the open sky. The ratio may be used to create a radiograph[22, 23, 30] or a 3D tomograph via inversion methods [72, 73].

3.2 Muon Scattering

If the direction of the muons before and after traversing a material is known, then the scattering angle of the muon can be calculated and compared with multiple coulomb scattering (MCS) theory. As evidenced in the name, MCS involves a series of small coulombic scatters of a charged particle as it traverses a material. The theory of multiple coulomb scattering was well formulated by Molière and presented by Bethe[74]. Rossi and Greisen also presented a simpler model of scattering in a single plane (Figure 3.2). They searched for a solution to:

$$\frac{\partial F}{\partial t} = -\theta_u \frac{\partial F}{\partial u} + \left(\frac{E_s}{2p\beta}\right)^2 \frac{\partial^2 F}{\partial \theta_u^2}, [75] \tag{3.3}$$

where t is the distance traversed in the material in radiation lengths, u is the distance change in the transverse direction in radiation lengths, p is the particle momentum, β is the relativistic speed, E_s is a constant, and θ_u is the angle between the incident and exiting muon path. Rossi and Griesen presented a solution that neglected energy loss and resulted in the 2D multivariate-Gaussian:

$$F(t, u, \theta_u) = \frac{\sqrt{3}}{2\pi}\left(\frac{2p\beta}{E_s t}\right)^2 \exp\left[-\left(\frac{2p\beta}{E_s}\right)^2 \left(\frac{\theta_u^2}{t} - \frac{3u\theta_u}{t^2} + \frac{3u^2}{t^2}\right)\right] \tag{3.4}$$

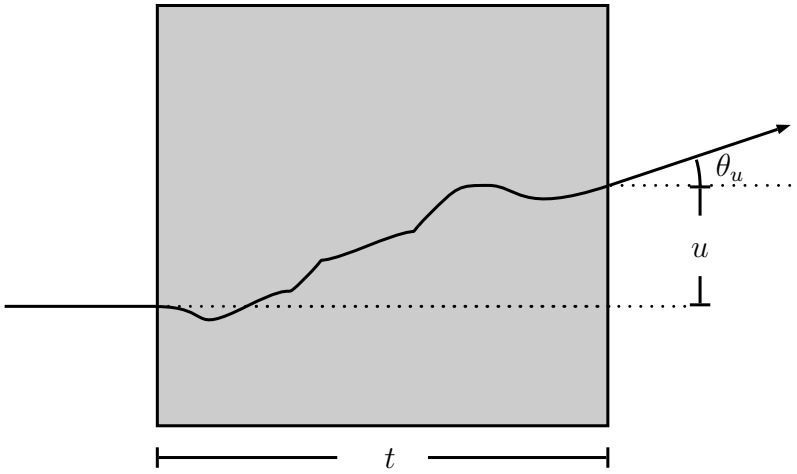

Figure 3.2: An exaggerated example of multiple coulomb scattering of a particle as it traverses a medium. The labeled quantities t, u, and θ_u are the same as the labels in [75].

which, after integrating u over the interval $(-\infty, \infty)$, results in

$$F(t, \theta_u) = \frac{1}{2\sqrt{\pi}} \left(\frac{2p\beta}{E_s t^{1/2}} \right) \exp \left[-\frac{1}{4} \left(\frac{2p\beta}{E_s} \right)^2 \frac{\theta_u^2}{t} \right] \tag{3.5}$$

Eyges expanded upon the solution to incorporate energy loss and produced:

$$F(t, u, \theta_u) = \frac{1}{2\pi\sqrt{B(t)}} \exp \left[-\frac{\theta_u^2 A_2(t) - 2u\theta_u A_1(t) + u^2 A_0(t)}{4A_0(t)B(t)} \right], [76] \tag{3.6}$$

with

$$\begin{aligned} A_0(t) &= \int_0^t \left(\frac{E_s}{2p(\eta)\beta(\eta)} \right)^2 d\eta, \\ A_1(t) &= \int_0^t (t-\eta) \left(\frac{E_s}{2p(\eta)\beta(\eta)} \right)^2 d\eta, \\ A_2(t) &= \int_0^t (t-\eta)^2 \left(\frac{E_s}{2p(\eta)\beta(\eta)} \right)^2 d\eta, \\ B(t) &= A_0(t)A_2(t) - A_1^2(t). \end{aligned} \tag{3.7}$$

More recent work by Lynch and Dahl adjusted the integrals from Eyges by fitting

the Gaussian scattering to distributions predicted by Molière to produce the fitted integrals:

$$\begin{aligned} A_0(t) &= E_0^2 \left(1 + 0.038 \ln[t]\right)^2 \int_0^t \frac{1}{p^2(\eta)\beta^2(\eta)} d\eta \\ A_1(t) &= E_0^2 \left(1 + 0.038 \ln[t]\right)^2 \int_0^t \frac{(t-\eta)}{p^2(\eta)\beta^2(\eta)} d\eta \\ A_2(t) &= E_0^2 \left(1 + 0.038 \ln[t]\right)^2 \int_0^t \frac{(t-\eta)^2}{p^2(\eta)\beta^2(\eta)} d\eta, \end{aligned} \tag{3.8}$$

with $E_0 = 13.6$ MeV/c and the natural log providing corrections that accurately reproduce the Molière predictions to within 11% or better in the range $t \in (10^{-3}, 100)$[77].

In muon scattering radiography, muon momentum is not easily measured and it is typical to ignore energy loss as a result. Neglecting energy loss in the Eyges solution reproduces the solution put forward by Rossi and Greisen, though the Lynch and Dahl correction remains. The corrected muon scattering in a single plane is then given by:

$$F(t, \theta_u) = \frac{p\beta}{\sqrt{2\pi} E_0 (1 + 0.038 \ln[t]) \sqrt{t}} \exp\left[-\frac{\theta_u^2 p^2 \beta^2}{2E_0^2 (1 + 0.038 \ln[t])^2 t} \right]. \tag{3.9}$$

This function describes a one dimensional Gaussian with a width of

$$\theta_0 = \frac{13.6 \text{ MeV/c}}{p\beta} \sqrt{t} \left(1 + 0.038 \ln[t]\right). \tag{3.10}$$

In reality, incident muons can scatter in two transverse directions (here referred to as u and v). Treating scatters in each plane as independent, the probability density function for muons scattering in any direction can be written as:

$$F(t, \theta_u, \theta_v) = \frac{p^2\beta^2}{2\pi E_0^2 (1 + 0.038 \ln[t])^2 t} \exp\left[-\frac{(\theta_u^2 + \theta_v^2) p^2 \beta^2}{2E_0^2 (1 + 0.038 \ln[t])^2 t} \right]. \tag{3.11}$$

Furthermore, the Gaussian can be reduced to a single scattering parameter for positive

angle scatters by introducing the small angle approximation

$$\theta = \sqrt{\theta_u^2 + \theta_v^2} \tag{3.12}$$

so

$$F(t, \theta) = \frac{1}{2\pi\theta_0^2} \exp\left[-\frac{\theta^2}{2\theta_0^2}\right]. \tag{3.13}$$

Equation 3.13 is often cited as the distribution that describes charged particle scattering (see Equation (32.16) in [70]).

Equation 3.11 can be reduced beyond 3.13 to describe angles between the incoming and outgoing 3D muon directions by applying a Jacobian (which for the symmetric Gaussian is $2\pi\theta$) to project the distribution onto a single positive axis. The resulting scattering probability density function is

$$F(t, \theta) = \frac{\theta}{\theta_0^2} \exp\left[-\frac{\theta^2}{2\theta_0^2}\right]. \tag{3.14}$$

From 3.14, a given scattering distribution's Gaussian width may infer the number of radiation lengths through which the muons traveled by the relation $\theta_0 \propto \sqrt{t}$ (to first order).

The value t can be rewritten as $t = \frac{\ell\rho}{X_0}$, where ℓ is the distance traveled in cm, ρ is the mass density of the material in g/cm^3, and X_0 is the radiation length of the material with units g/cm^2. Tsai gave the empirical method for calculating X_0 in [78] as

$$\frac{1}{X_0} = 4\alpha r_e^2 \frac{N_A}{A} \left\{ Z^2[L_{\text{rad}} - f(Z)] + ZL'_{\text{rad}} \right\}, \tag{3.15}$$

where α is the fine structure constant, r_e is the classical radius of the electron, and

L_{rad}, L'_{rad}, and $f(Z)$ are empirical functions tabulated by Tsai. If $A = 1$ g/mol, $4\alpha r_e^2 N_A/A = (716.408\ \text{g/cm}^2)^{-1}$. L_{rad} and L'_{rad} are tabulated and given by Tsai and can be found in [70]. $f(Z)$ is given by an infinite sum, but is well approximated for elements up to uranium by the first terms

$$f(Z) = (\alpha Z)^2 \left\{ [1 + (\alpha Z)^2]^{-1} + 0.20206 \right. \\ \left. -0.0369(\alpha Z)^2 + 0.0083(\alpha Z)^4 - 0.002(\alpha Z)^6 \right\}. \tag{3.16}$$

When using t or θ_0^2 as a muon signal, both quantities are proportional to Z^2/A giving muon scattering an additional power of Z dependence. This method is especially useful when using cosmic-ray muons to passively identify high Z materials, such as actinides.

3.2.1 Multi-Group Modeling

As shown in 3.10, the width of the scattering Gaussian is inversely proportional to βp. When the muon momentum is not known but estimates of t are desired, assumptions must be made. For the case of cosmic-ray muons, a momentum estimator model was developed at Los Alamos National Laboratory[79, 80] multigroup (here referred to as the multi-group model).

The multi-group model assumes that the cosmic-ray muon momentum spectrum can be broken down into a finite number of momentum groups. Each group has a weighting amplitude that allows the probability density function to be written as

$$F(t, \theta) = \sum_i \frac{\alpha_i \theta}{\theta_i^2} \exp\left[-\frac{\theta^2}{2\theta_i^2} \right], \tag{3.17}$$

where α_i is the weighted amplitude of the momentum group with the requirement $\sum_i \alpha_i = 1$, θ is the scattering angle, and θ_i is identical in form to 3.10 with the $p\beta$ dependence varying with the momentum group. The weighted amplitudes may be

fitted if momentum groups are assumed and the expected θ_i are known for some muon scattering data, as is done in [79]. Once the amplitudes and momentum groups are known, estimates of $\sqrt{t}(1+0.038\ln[t])$ may be made by fitting 3.17 to muon scattering data. To good approximation

$$t(1+0.038\ln[t])^2 \simeq t = \frac{\ell\rho}{X_0}, \tag{3.18}$$

being within 20% error for t in the range $0.1-12$ and within 35% error for t in the range $0.01-70$. Making an estimate of $t(1+0.038\ln[t])^2$, using the multi-group model, is approximately equivalent to making an estimate of the number of radiation lengths the muons have passed through. In this work, the multi-group estimate $t = \ell\rho/X_0$ will be referred to as the areal density, while the quantity ρ/X_0 will be referred to as the scattering density.

3.3 Predicting Muon Momenta

Cosmic-ray muons originate tens of kilometers above the earth as high energy nuclei from cosmic events interact with nuclei in the atmosphere. The bombardment of the atmosphere by these high energy nuclei is nearly uniform in the upper atmosphere. Though the source of cosmic-rays is uniform, the flux is dominated by cosmic-ray muons and neutrinos at low altitude—within a few km of sea level— as shown in Figure 3.3. Both muons and neutrinos arise from decays of short-lived daughter particles from the initial cosmic-ray event. The particles that produce nearly all of the muons are $\pi^{\pm}$ and $K^{\pm}$ which decay as:

$$\pi^+ \rightarrow \mu^+ + \nu_\mu, \text{ at } 99.98770 \pm 0.00004\%$$
$$K^+ \rightarrow \mu^+ + \nu_\mu, \text{ at } 63.56 \pm 0.11\%$$

with the charge conjugates decaying to the conjugate particles. The relatively long lifetime of the muon (2.2 μs), combined with Lorentz time dilation, allows them to reach the earth's surface. In this work, two models were used to simulate the muon momentum spectrum.

3.3.1 The Reyna Model

The first method draws upon work done by Reyna [81], who used six data sets [82–87] of cosmic-ray muon intensity as a function of zenith angle and muon momentum (Table 3.3.1). Reyna plotted all of the data against muon momentum (Figure 3.4) and found that by plotting the data as a function of $\xi \equiv p_\mu \cos(\theta_z)$, the data aligned with a uniform shape (Figure 3.5). In order to scale the data, Reyna included an additional factor of $1/\cos^3(\theta_z)$ (Figure 3.6), which provided the basis of the model for muon intensity as a function of muon momentum and zenith angle

$$I(p_\mu, \theta_z) = \cos^3(\theta_z) I_V(\xi), \tag{3.19}$$

where function $I_V(\xi)$ predicts the vertical muon intesity. A semi-empirical for $I_V(p_\mu)$ was previously developed by Bugaev et al.[88] and has the form

$$I_V(p_\mu) = C_p^{-(\gamma_0 + \gamma_1 \log[p_\mu] + \gamma_2 \log^2[p_\mu] + \gamma_3 \log^3[p_\mu])}, \tag{3.20}$$

where C_p and γ_i are best fit parameters for the vertical muon intensity. While Bugaev et al. broke $I_V(p_\mu)$ into 4 momentum ranges, Reyna reformulated I_V to be a function of ξ and allowed the fit parameters to vary while creating a least squares best fit of $I(p_\mu, \theta_z)$ over all six data sets. Reyna's best fit parameters are:

$$C_P = 0.00253,\ \gamma_0 = 0.2455,\ \gamma_1 = 1.288,\ \gamma_2 = -0.2555,\ \text{and } \gamma_3 = 0.0209.$$

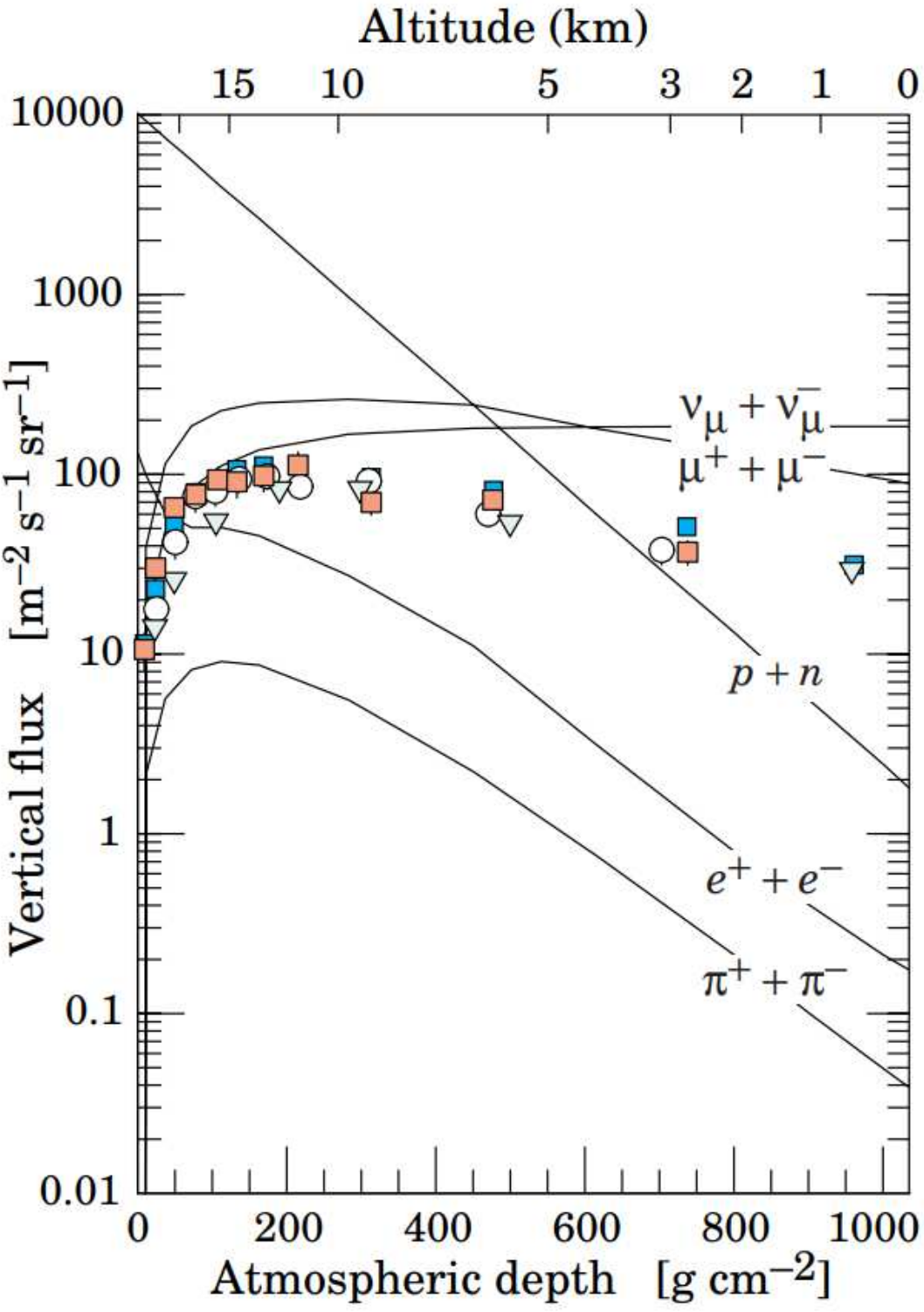

Figure 3.3: Vertical intesity of cosmic ray species as a function of atmospheric depth [70]. The points show measurements of negative muons with $E_\mu > 1$ GeV

Reyna predicted that $I(p_\mu, \theta_z)$ could be considered valid over all zenith angles and for muon momenta from $1 - 2000$ GeV.

Experiment		Zenith Angle Range (°)	p_μ(GeV)
Nadi and Sinha[82]	0°	0 - 0.3	5 - 1200
MARS [83]	0°	0 - 0.08	20 - 500
Kellogg et al.[84]	30°	25.9 - 34.1	50 - 1700
	75°	70.9 - 79.1	50 - 1700
OKAYAMA[85]	0°	0 - 1	1.5 - 250
	30°	26 - 34	2 - 250
	60°	59 - 61	3 - 250
	75°	69 - 81	3 - 250
	80°	79 - 81	3 - 250
Kiel-Desy[86]	75°	68 - 82	1 - 1000
MUTRON[87]	89°	86 - 90	100 - 20,000

Table 3.1: The experiment, angular range of the zenith angle, and range of the muon momentum for the size data set used to confine the Reyna Model. Duplicated from [81].

3.3.2 A Low Momentum Model

As mentioned in 3.2, the width of the scattering distribution is inversely proportional to the muon momentum. The Reyna model is only fit to data with momenta above 1 GeV. In an effort to predict the distribution for low muon momenta, a second muon momentum distribution was created. This was based on the following assumptions: the muon momentum spectrum at the "start" of the atmosphere is isotropic above the horizon, the muon momentum distribution at sea level is symmetric about the zenith, muon ionization energy loss can be predicted throughout the atmosphere, the atmosphere's mass density is approximately linear with height, and the mean free path through which a muon travels can be predicted from its momentum and lifetime.

In order to predict the initial muon momentum spectrum prior to traversing the atmosphere; the height, density, and energy loss needed to be predicted. A simple

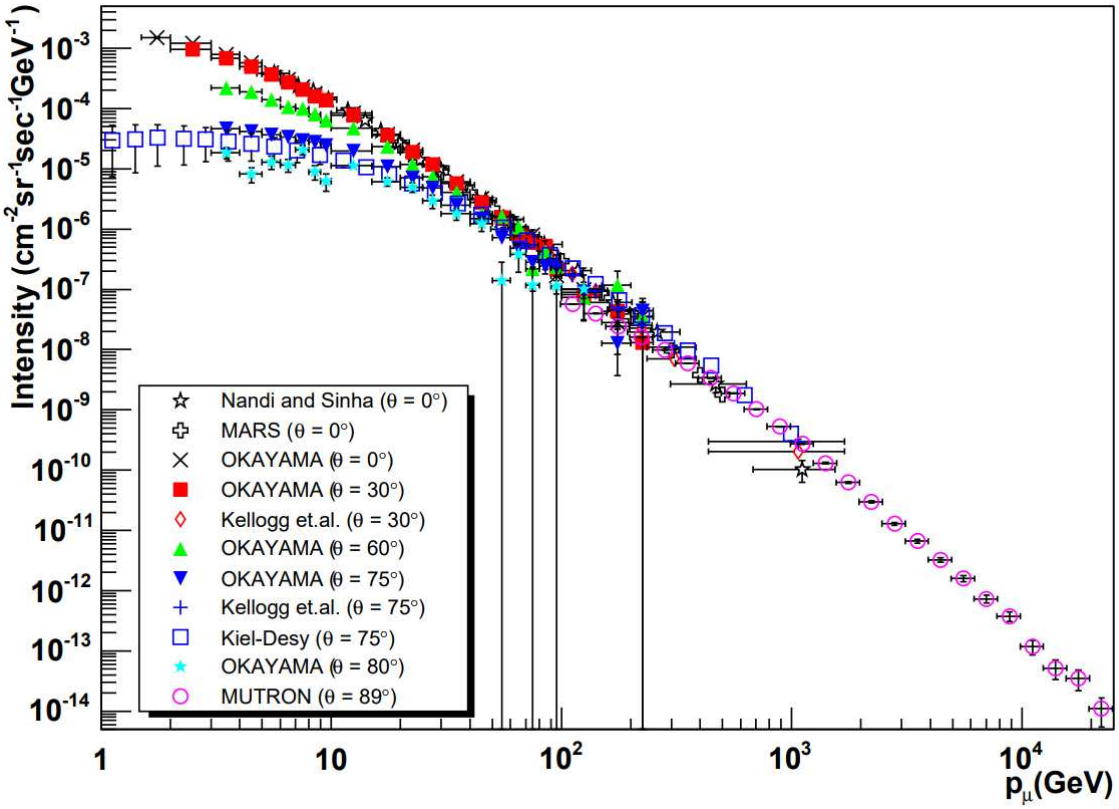

Figure 3.4: The differential surface muon intensity is plotted as a function of muon momentum for all the data[81].

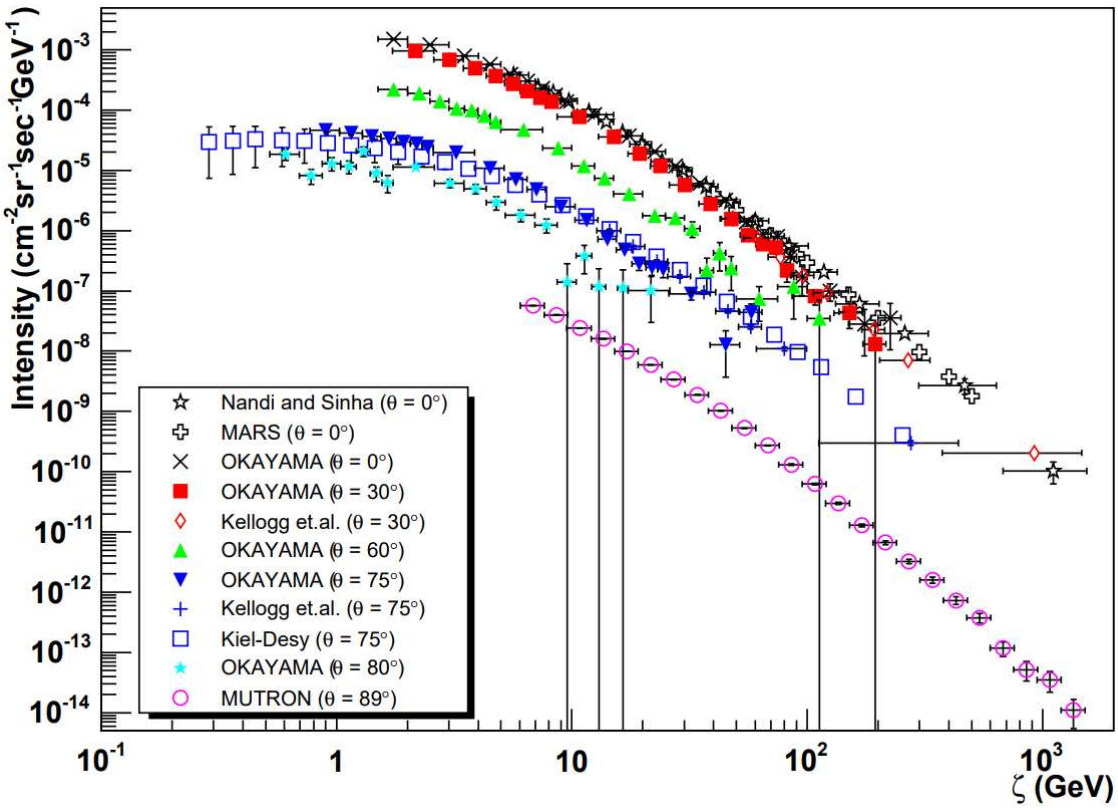

Figure 3.5: The differential surface muon intensity is plotted as a function of ξ[81].

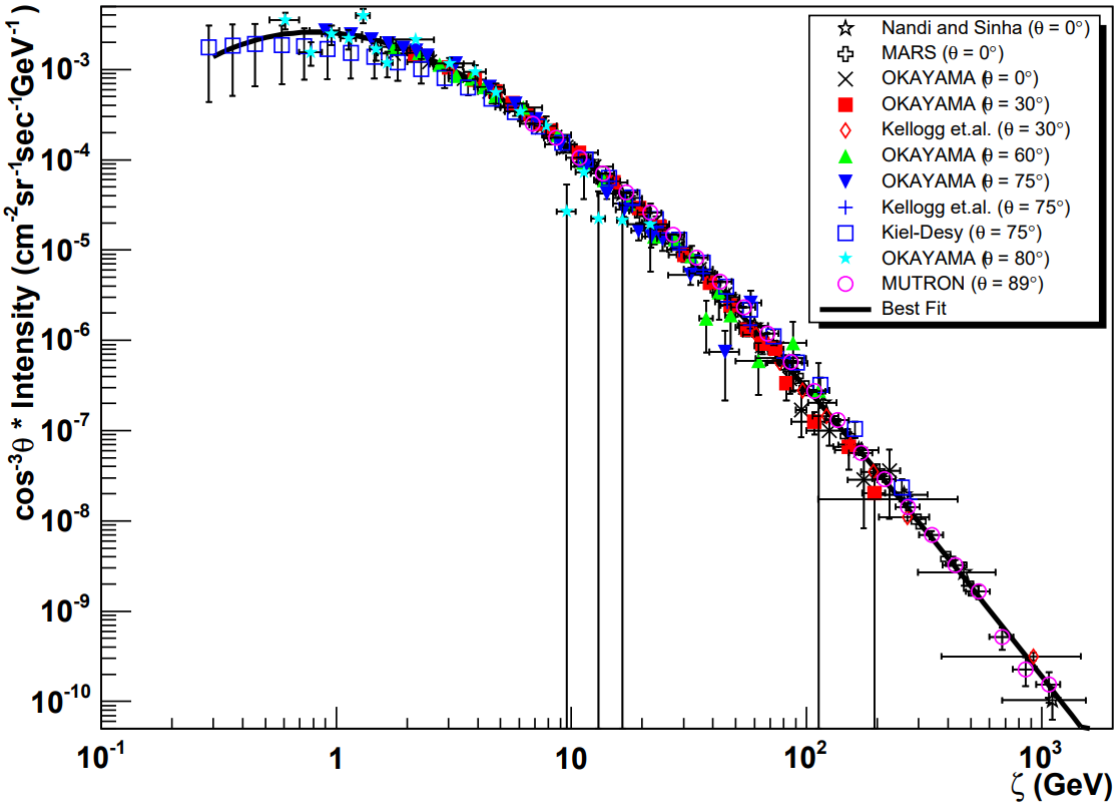

Figure 3.6: Surface muon intensity is plotted as a function of ξ and scaled by a factor $1/\cos^3(\theta_z)$[81].

model of the atmosphere was created which assumed that air mass density is linear with elevation and can be given as

$$\rho(h) = \rho_0 \left(1 - \frac{h}{H}\right), \tag{3.21}$$

where $\rho_0 = 1.5 \times 10^{-3}$ g/cm^3[70] and H is the elevation of the start of the atmosphere. To predict H, a vertical column density of 1,000 g/cm^2[89] was set equal to the integral of $\rho(h)$ from sea level to H, i.e.

$$1,000 \frac{\text{g}}{\text{cm}^2} = \int_0^H 1.5 \times 10^{-3} \frac{\text{g}}{\text{cm}^3} \left(1 - \frac{h}{H}\right) dh.$$

Solving the above produces an estimate for H of 1.33×10^6 cm.

Energy loss per unit distance is estimated by the product

$$\rho(h) * \left.\frac{dT}{d\ell}\right|_{\text{min}},$$

where $dT/d\ell|_{\text{min}} = 1.815$ MeV/g/cm^2 is the ionization energy loss rate for minimally ionizing muons. The kinetic energy of the muon as it travels through the atmosphere is then predicted as

$$T(h) = T_0 + \int_H^h \rho(h) \left.\frac{dT}{d\ell}\right|_{\text{min}} d\ell. \tag{3.22}$$

This relation is used to predict how the muon energy distribution is shifted as a function of atmosphere, with the net effect being a shifting down of the muon energy distribution by $\int_H^0 \rho(h)(dT/d\ell)|_{\text{min}} d\ell$.

However, a simple shift of the muon energy distribution does not take into account the muon life time $\tau_\mu = 2.197$ μs. A simple attenuation model predicts that the

number of muons with a given energy will follow an exponential decay of

$$N = N_0 \exp\left(-\frac{\ell}{\lambda}\right). \tag{3.23}$$

The mean free path of the muons prior to decaying, taking into account relativistic effects, is simply

$$\lambda = vt = \beta c\gamma\tau_\mu = \frac{p_\mu}{m_\mu}\tau_\mu, \tag{3.24}$$

where βc is the muon velocity and m_μ is the muon mass. The muon momentum in 3.24 is related to the muon energy in 3.22 by the relativistic formula

$$(T + mc^2)^2 = p^2c^2 + m^2c^4. \tag{3.25}$$

By combining 3.21, 3.22, 3.23, 3.24, and 3.25, it is possible to make predictions of the muon momentum spectrum as muons travel through a pathlength ℓ. The elevation of the muons as they travel along ℓ is determined by θ_z and is given by

$$h(\ell, \theta_z) = \sqrt{(R_e + \ell\cos(\theta_z))^2 + (\ell\sin(\theta_z))^2} - R_e, \tag{3.26}$$

where $R_e = 6.371 \times 10^8$ cm is the earth's radius. The geometry is illustrated in Figure 3.7.

Estimating the initial muon momentum spectrum at height H was carried out by using data from [89] which measured the vertical muon energy spectrum. Each data point was projected from sea level to elevation H using the described equations (Figure 3.8). The predicted muon data at height H was fit with a power function,

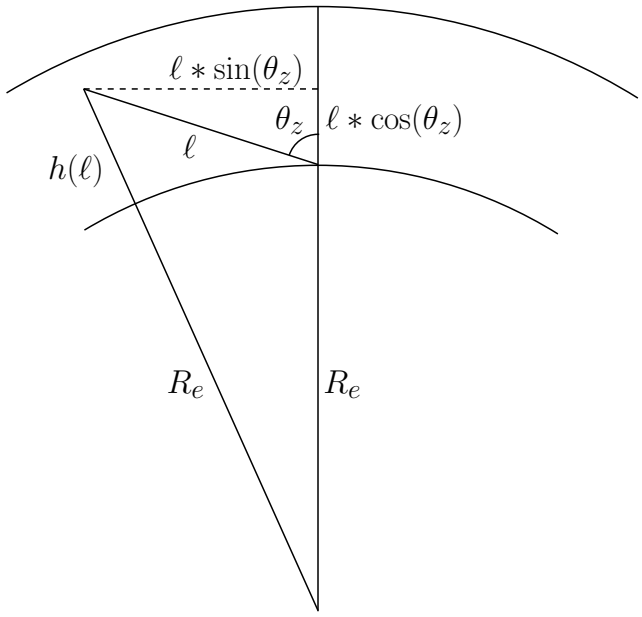

Figure 3.7: A drawing showing the geometric layout to derive a muons height as it travels along path length ℓ at angle θ_z.

which had a best fit of

$$F(T) = 7.25 \times 10^7 T^{-2.883}.$$

The best fit function was discretized into 10 MeV bins from 0 to 20 GeV and projected along ℓ from H to 0 for 90, 1-degree steps to cover the angles from the azimuth to the horizon. Plots of the resulting momentum spectrum are shown in Figures 3.9 and 3.10.

A quick test of the validity of the model is a check of the shape of the distribution against the predicted $\cos^2(\theta_z)$ differential distribution for the cosmic-ray muon flux. To do this, all of the momentum bin values were summed up in each angle bin to show the θ_z dependence of the flux. The resulting distribution was fit via least squares against a $A\cos^2(\theta_z)$ function, where A was the fit parameter. The resulting data and fit are shown in Figure 3.11. An agreement is seen between the model's prediction for the θ_z dependence of the muon flux and the assumed $\cos^2(\theta_z)$ flux shape.

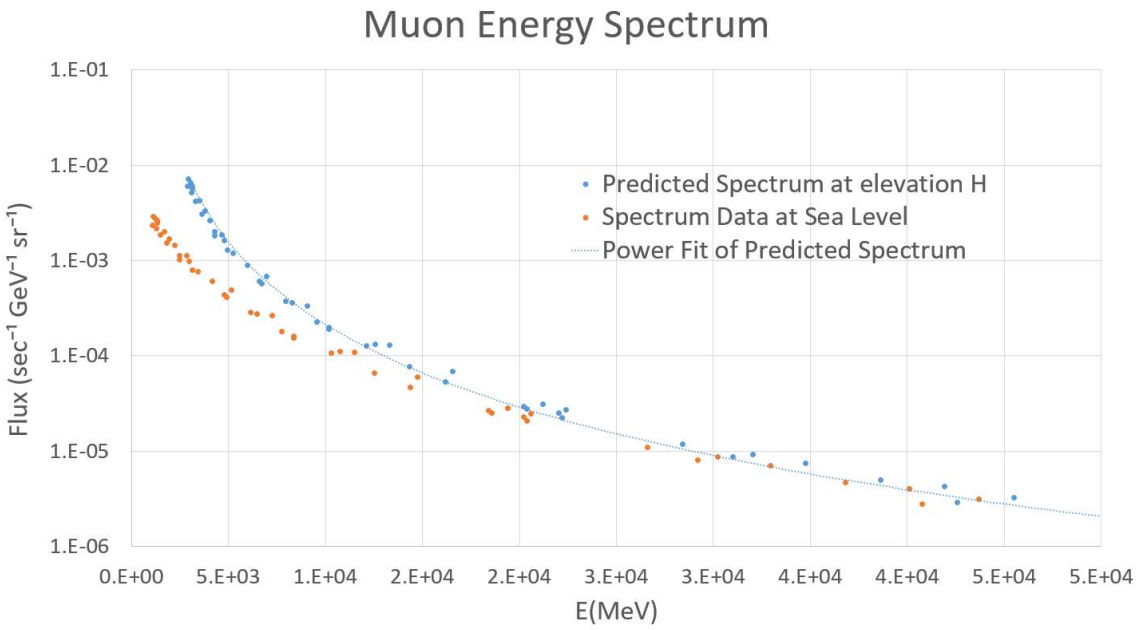

Figure 3.8: The muon energy spectrum data at sea level[89], predicted values at H for the model, and the power fit.

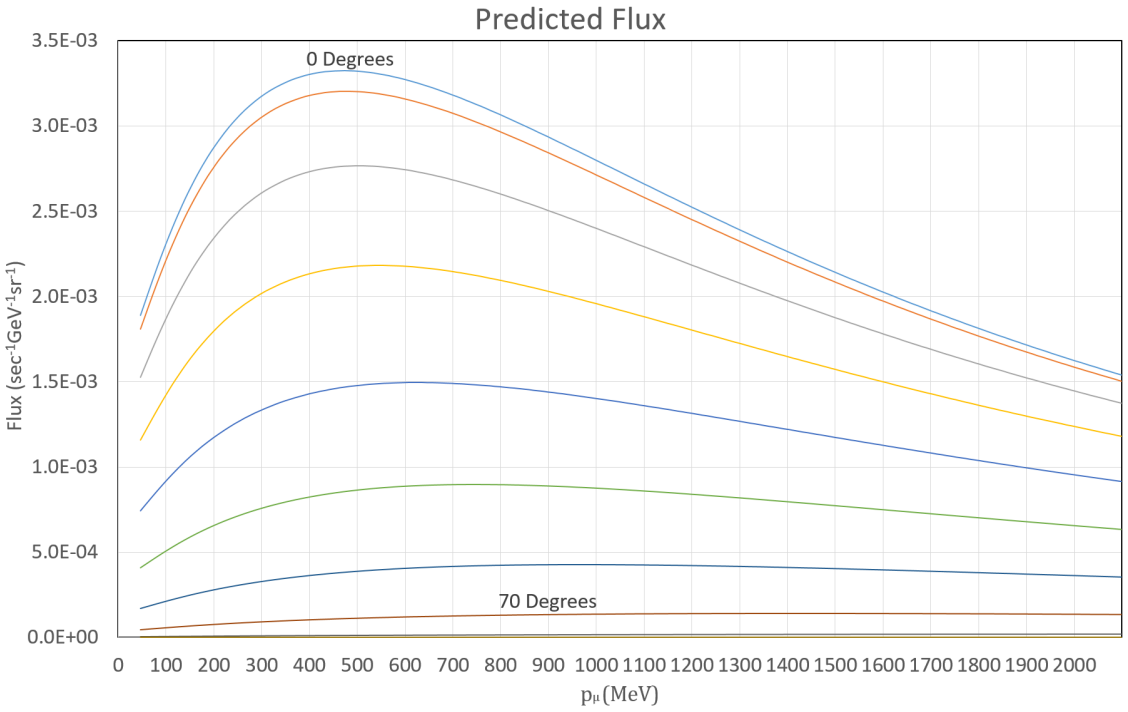

Figure 3.9: The resulting predicted muon momentum spectrum at low momentum plotted in 10 degree steps.

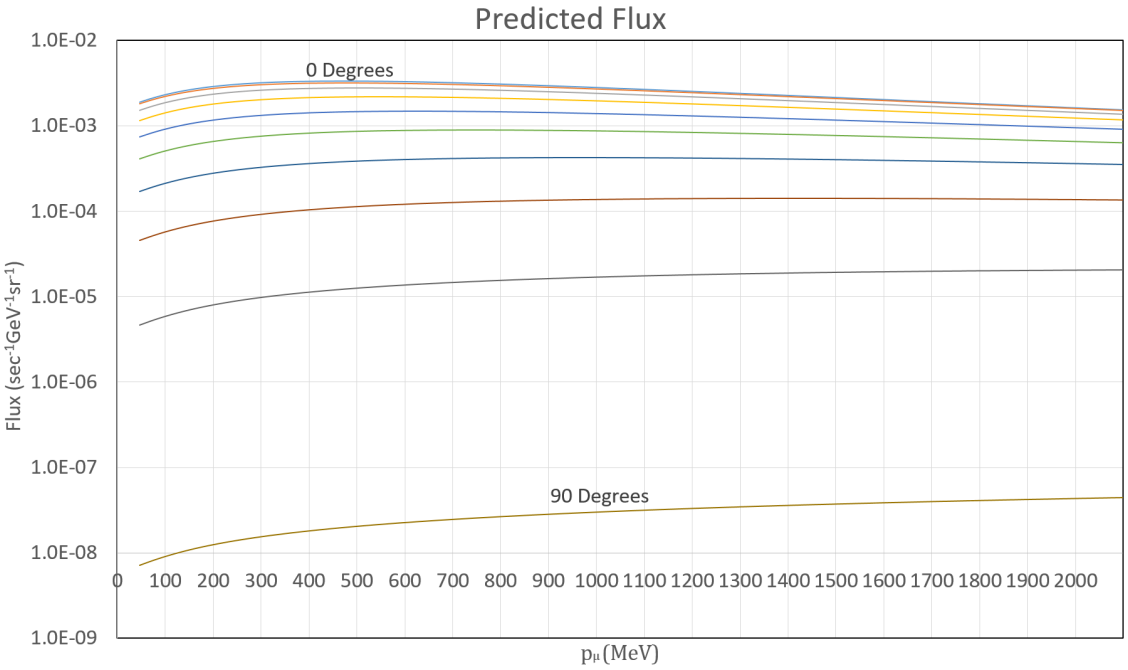

Figure 3.10: The resulting predicted muon momentum spectrum at low momentum plotted on a log scale in 10 degree steps.

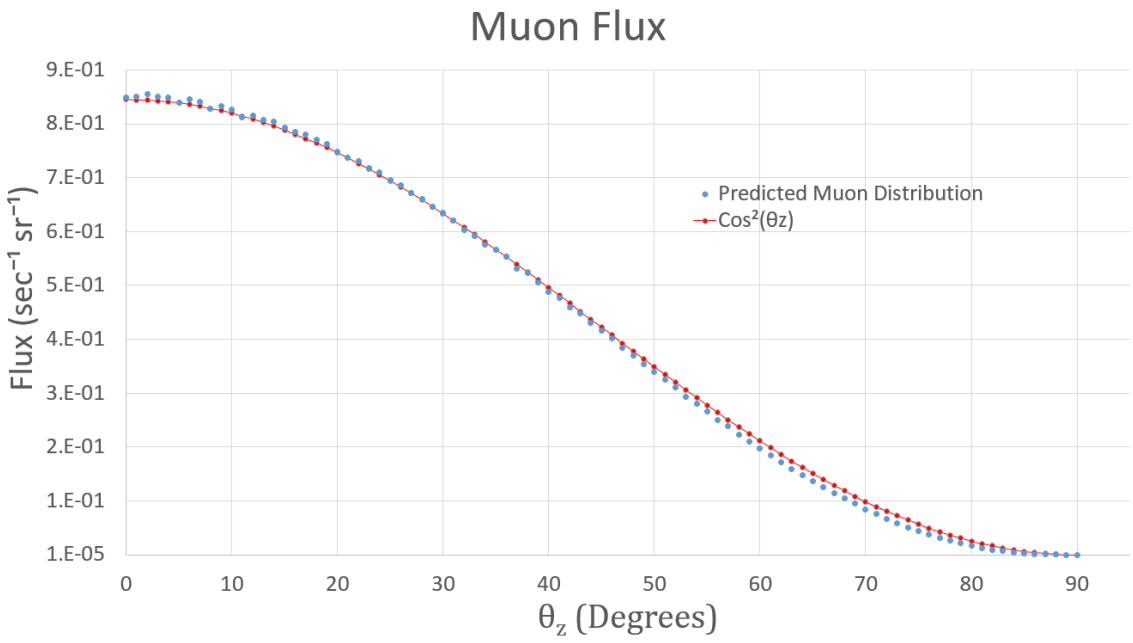

Figure 3.11: The predicted muon flux distribution compared with the predicted $\cos^2(\theta_z)$ distribution.

3.4 Image Reconstruction

The method of reconstructing multidimensional functions from a continuum of integrated projections at varying angles was first discussed by Radon[90]. Applications of this technique to produce tomographic images of the interior of the human body via a series of x-ray images were first formalized by Cormack [91, 92] and demonstrated by Hounsfield [93] and Ambrose[94]. Computed tomography techniques were soon after extended to charged particle imaging with alpha particles[95] and heavy nuclei[96]. Much of the work presented here draws on reconstructive tomographic techniques. The following presents the theory of the two methods used and draws on material presented by Kak and Slaney[97].

3.4.1 The Radon Transform

The Radon transform describes the transform of some function to a continuous function of integrated projections. A typical example of the Radon transform of a function $f(x, y)$ to a function $g(\phi, \rho)$ is shown in Figure 3.4.1. The transform itself is described as an integral along the line

$$\rho = x\cos(\phi) + y\sin(\phi) \tag{3.27}$$

such that

$$g(\phi, \rho) \equiv \int_{-\infty}^{\infty}\int_{-\infty}^{\infty} f(x, y)\delta(x\cos(\phi) + y\sin(\phi) - \rho)dxdy, \tag{3.28}$$

with ρ being the positive or negative distance away from the origin and ϕ being akin to the polar coordinate angle. While the Radon transform may be described in higher dimensions, here the focus is only on a two dimensional transform which will be referred to as a sinogram.

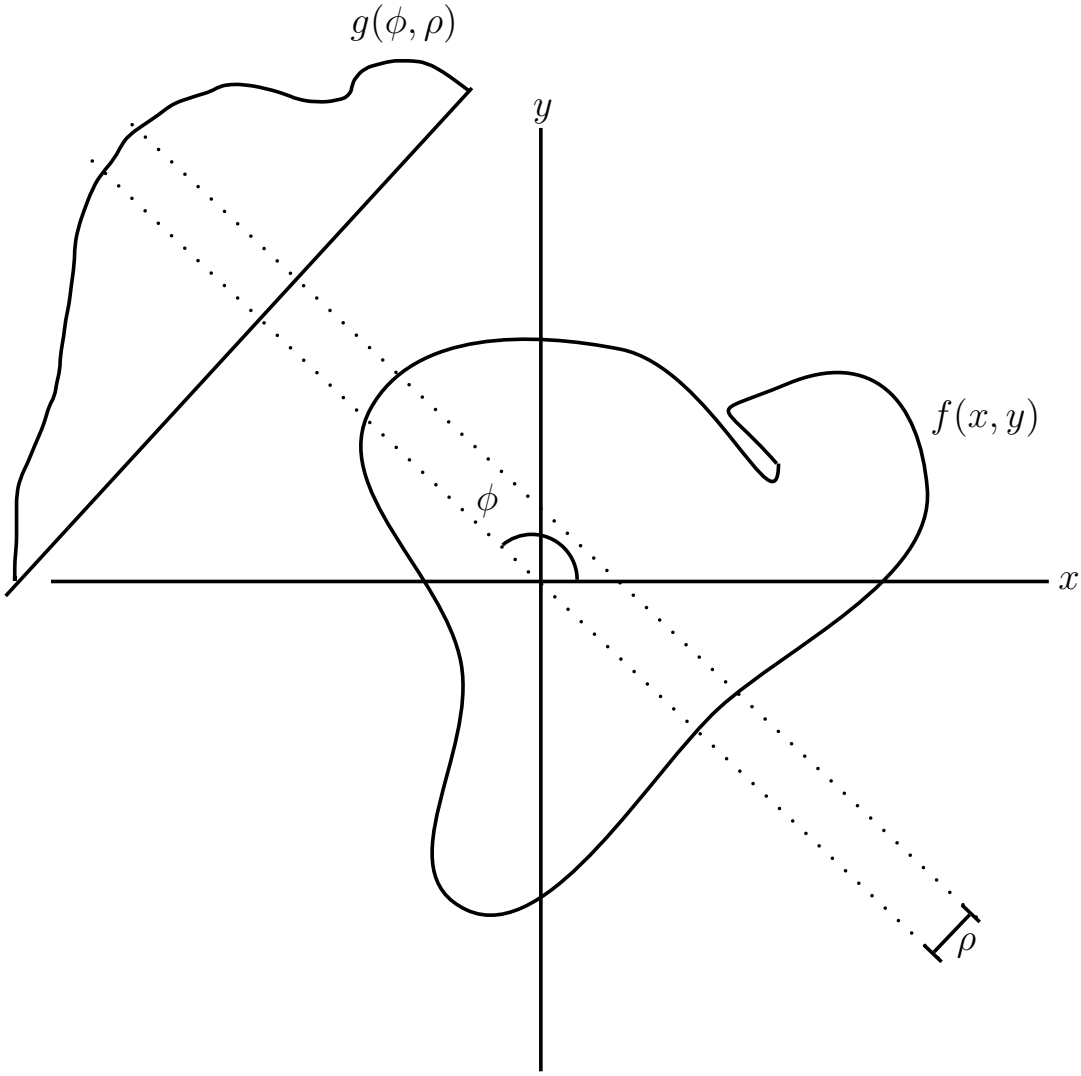

Figure 3.12: An example of the function $f(x, y)$ that is integrated along infinite parallel lines to produce the function $g(\phi, \rho)$. Shown is an example projection $g(\phi, \rho)$ at angle ϕ, though $g(\phi, \rho)$ is continuous across all values $\phi \in [0, \pi)$ and $\rho \in (-\infty, \infty)$.

3.4.2 The Inverse Radon Transform

The first class of methods for inverting the Radon transform are called direct inversion methods and draw on properties of the Fourier Slice Theorem. Simply stated, the Fourier Slice Theorem demonstrates that the one-dimensional Fourier transform of the function $g(\phi, \rho)$ is related to the two-dimensional Fourier transform of the function $f(x, y)$. This is quickly shown via:

$$\mathcal{G}(\omega, \phi) = \int_{-\infty}^{\infty} g(\phi, \rho) \exp\left[-i2\pi\omega\rho\right] d\rho$$

which, when combined with the definition of $g(\phi, \rho)$, becomes

$$\begin{aligned}\mathcal{G}(\omega, \phi) &= \int_{-\infty}^{\infty}\int_{-\infty}^{\infty}\int_{-\infty}^{\infty} f(x, y)\delta(x\cos(\phi) + y\sin(\phi) - \rho)\exp\left[-i2\pi\omega\rho\right] d\rho dx dy \\ &= \int_{-\infty}^{\infty}\int_{-\infty}^{\infty} f(x, y)\exp\left[-i2\pi\omega(x\cos(\phi) + y\sin(\phi))\right] dx dy. \end{aligned} \tag{3.29}$$

The original one-dimensional Fourier transform has now been rewritten as a two dimensional transform with frequencies $\omega\cos(\phi)$ and $\omega\sin(\phi)$, i.e.

$$\mathcal{G}(\omega, \phi) = \mathcal{F}(\omega\cos(\phi), \omega\sin(\phi)) \tag{3.30}$$

with the right-hand side being the two-dimensional Fourier transform of $f(x, y)$.

3.4.3 Filtered Back Projection

To reconstruct $f(x, y)$, the inverse Fourier transform of $\mathcal{F}(u, v)$ must be taken. A change of coordinates is used to transform $\mathcal{F}(u, v)$ to $\mathcal{F}(\omega\cos(\phi), \omega\sin(\phi))$; namely $u = \omega\cos(\phi)$ and $v = \omega\sin(\phi)$ with the additional Jacobian of the transform $dudv =$

$\omega d\omega d\phi$. Using the change of coordinates, the inverse Fourier transform becomes:

$$\begin{aligned} f(x,y) =& \frac{1}{2\pi}\int_{-\infty}^{\infty}\int_{-\infty}^{\infty}\mathcal{F}(u,v)\exp\left[i2\pi(ux+vy)\right]dudv \\ =& \frac{1}{2\pi}\int_{0}^{2\pi}\int_{0}^{\infty}\mathcal{F}(\omega\cos(\phi),\omega\sin(\phi))\exp\left[i2\pi\omega(x\cos(\phi)+y\sin(\phi))\right]\omega d\omega d\phi. \end{aligned} \tag{3.31}$$

Making use of the Fourier Slice Theorem further reduces the transform to

$$f(x,y) = \int_{0}^{2\pi}\int_{0}^{\infty}\mathcal{G}(\omega,\phi)\exp\left[i2\pi\omega(x\cos(\phi)+y\sin(\phi))\right]\omega d\omega d\phi. \tag{3.32}$$

Recognizing that $\mathcal{G}(\omega,\phi) = \mathcal{G}(-\omega,\phi+\pi)$, the inverse transform can be written as

$$f(x,y) = \frac{1}{2\pi}\int_{0}^{\pi}\int_{0}^{\infty}|\omega|\mathcal{G}(\omega,\phi)\exp\left[i2\pi\omega(x\cos(\phi)+y\sin(\phi))\right]d\omega d\phi \tag{3.33}$$

$$= \frac{1}{2\pi}\int_{0}^{\pi}\left[\int_{0}^{\infty}|\omega|\mathcal{G}(\omega,\phi)\exp\left[i2\pi\omega\rho\right]_{\rho=x\cos(\phi)+y\sin(\phi)}d\omega\right]d\phi. \tag{3.34}$$

The $|\omega|$ term is referred to as the ramp filter and is thought of as a high pass filter for the inverse transform. Since the inverse transform is valid for any $\rho = x\cos(\phi) + y\sin(\phi)$, the calculated transform can be projected back along the line that satisfies the value of ρ. Thus it is the action of filtering a slice of the Fourier transform of the integrated projection and then back projecting it along $\rho = x\cos(\phi) + y\sin(\phi)$ that gives the method its name.

3.4.4 Algebraic Reconstruction Technique

The second class of methods is based on the idea of reconstructing the image via a set of linear equations and are referred to as algebraic reconstruction methods. This class of methods does not try to find a solution via a direct inversion but rather chooses to describe the problem discretely. Here the Radon transform is thought of as a sum rather than an integral. It is assumed that the function $f(x,y)$ can be well

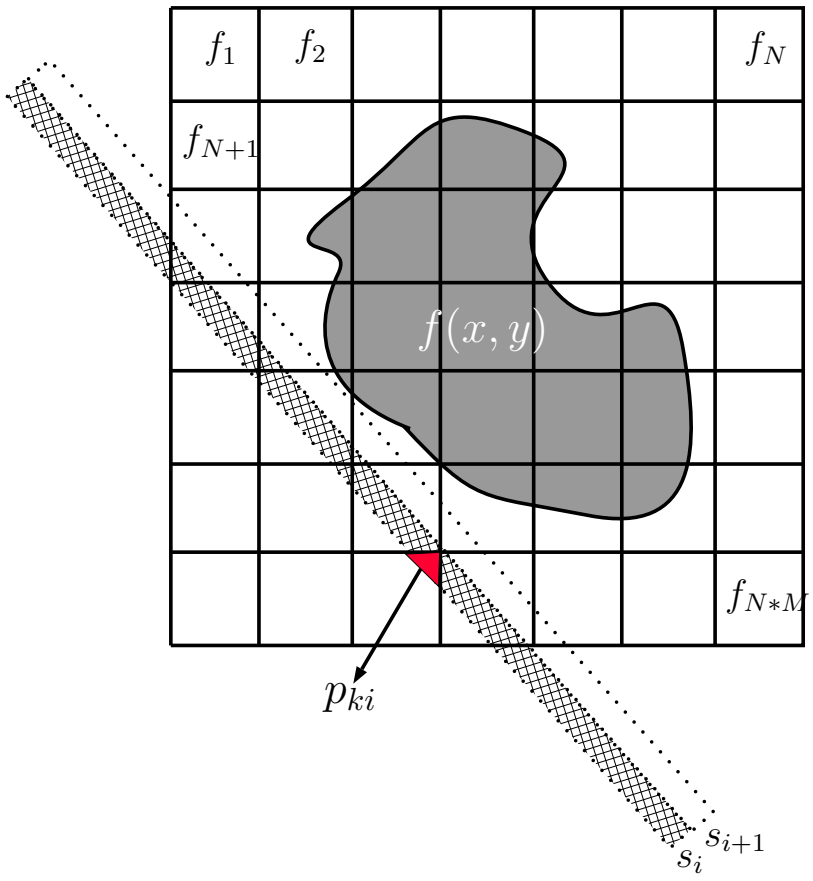

Figure 3.13: The geometric representation of $s_i = \sum_k p_{ki} f_k$.

approximated by an $M \times N$ grid of cell values (f_k, $k \in [0, N*M]$), similar to a digital picture. A sinogram of finite elements (s_i, $i \in [0, I]$) represents the number of sums along some ray paths of the intersected cells of the grid. Each sinogram element can be written as

$$s_i = \sum_k p_{ki} f_k, \tag{3.35}$$

where k represents the index of the cell values, i is the index of the sinogram values, and p_{ki} is the fraction of the area of cell k that is passed through by the ray used to create s_i (see Figure 3.4.4).

It is easy to extend the series of equations described by 3.35 to a matrix equation

$$\boldsymbol{s} = \boldsymbol{P}\boldsymbol{f} \tag{3.36}$$

which solution for $\boldsymbol{f}$ is given by

$$\boldsymbol{f} = \boldsymbol{P}^{-1}\boldsymbol{s}. \tag{3.37}$$

In most cases the size of P prohibits solving 3.36 by direct inversion due to memory requirements. Additionally, the system of equations described by 3.36 is underdetermined due to $M \times N > I$. Most algebraic methods make use of the Kaczmarz method [98] to find a suitable solution. The Kaczmarz method requires the iterative projection of solution $\boldsymbol{f}^{(t-1)}$ onto the row $\boldsymbol{P}_i$ of $\boldsymbol{P}$ and comparing it against s_i, i.e.

$$\boldsymbol{f}^{(t)} = \boldsymbol{f}^{(t-1)} - \frac{(\boldsymbol{P}_i \cdot \boldsymbol{f}^{(t-1)} - s_i)}{\boldsymbol{P}_i \cdot \boldsymbol{P}_i}\boldsymbol{P}_i.$$

The most popular of these methods are known as Simultaneous Algebraic Reconstruction Techniques (SART) and Simultaneous Iterative Reconstruction Techniques (SIRT). However, in this work iterative techniques were not needed.

3.4.5 Dry Cask Modeling

In this work, assumptions of the imaged volume were made. Rather than assuming a grid of $N \times M$ cells could approximate the dry storage cask, a simple two-dimensional model was made that approximated the interior cross-section of the cask; as shown in Figure 3.14. By simplifying the cask to a model with relatively few elements, the size of $\boldsymbol{P}$ decreases substantially from $I \times N \times M$ to $I \times \#$ of model elements, with the number of elements being much less than $N \times M$. Additionally, here it is assumed that the number of sinogram elements (I) is much larger than the number of model

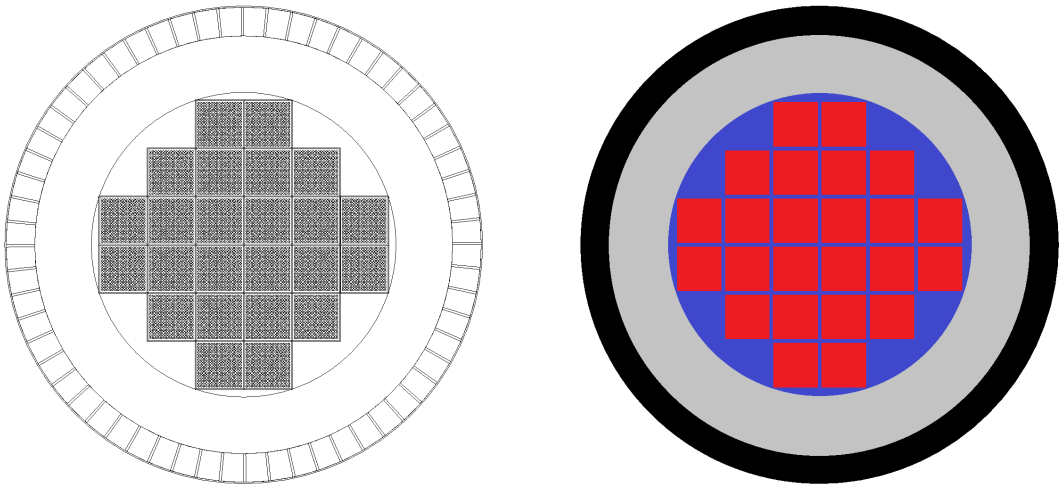

Figure 3.14: A cross-section of a simulated TN-24P cask (on left) shows intricate detail which is beyond the necessary requirements for detecting fuel diversion. A simplified model (on right) reduces the detail to fuel bundles (red), empty space within the cask (blue), steel gamma shielding (grey), and thermal neutron shielding (black).

elements, such that the sinogram data over-determines the element values.

Rather than trying to solve 3.36, a least squares χ^2 is defined:

$$\chi^2 = \sum_i \left(\sum_k \ell_{ki} f_k - s_i \right)^2 , \tag{3.38}$$

where ℓ_{ki} indicates the path-length of the sinogram ray i through model element k. By taking the derivative of χ^2 with respect to the model element values, a minimum of χ^2 is found:

$$\begin{aligned} \frac{d\chi^2}{df_j} &= 2 \sum_i \left(\sum_k \ell_{ki} f_k - s_i \right) \ell_{ji} = 0 \\ \Rightarrow \sum_i \ell_{ji} s_i &= \sum_i \sum_k \ell_{ki} \ell_{ji} f_k . \end{aligned} \tag{3.39}$$

Again, a matrix equation is now written as

$$\boldsymbol{y} = \boldsymbol{M} \boldsymbol{f} \tag{3.40}$$

where $\boldsymbol{y}_j = \sum_i \ell_{ki} s_i$, $\boldsymbol{M}_{jk} = \sum_i \ell_{ki}\ell_{ji}$, and $\boldsymbol{f}_j = f_j$. The solution for $\boldsymbol{f}$ in 3.40 is found by matrix inversion

$$\boldsymbol{f} = \boldsymbol{M}^{-1}\boldsymbol{y}.$$

Chapter 4

Muon Scattering Measurements at Idaho National Laboratory

Two experimental measurements of cosmic-ray muons scattering in a spent nuclear fuel storage cask were performed at Idaho National Laboratory (INL). The interrogated cask was a partially loaded Westinghouse MC-10 spent fuel dry-storage cask [99]. Taking data required the deployment of the Los Alamos National Laboratory's Mini Muon Tracker (MMT). The work presented here was published by the Los Alamos National Laboratory's Threat Reduction team in [100, 101].

4.1 MMT

The MMT is composed of two supermodule drift tube tracking detectors to measure incoming and outgoing muon tracks. The geometry of an MMT module is composed of 12 drift tube modules containing 24 drift tubes each. Each drift tube is a hollow aluminum cylinder with a length of 1.2 m, an outer diameter of 5.08 cm, and a wall thickness of 0.89 mm (Figure 4.1). A 30-μm diameter gold-plated tungsten wire is centered in and runs the length of each drift tube. Each tube is sealed with 1 bar of a gas mixture composed of 47.5% Ar, 42.5% CF_4, 7.5% C_2H_6, and 2.5% He. While in operation, the tungsten wire acts as an anode with a DC voltage of +2585 V relative to the aluminum wall of the tube. The DC voltage of +2585 sits in the regime where a drift tube's detection efficiency is above 90% (Figure 4.2).

The applied voltage is not so large as to create an electrical break down through the gas from the anode to the wall, but it does form a large electrostatic gradient

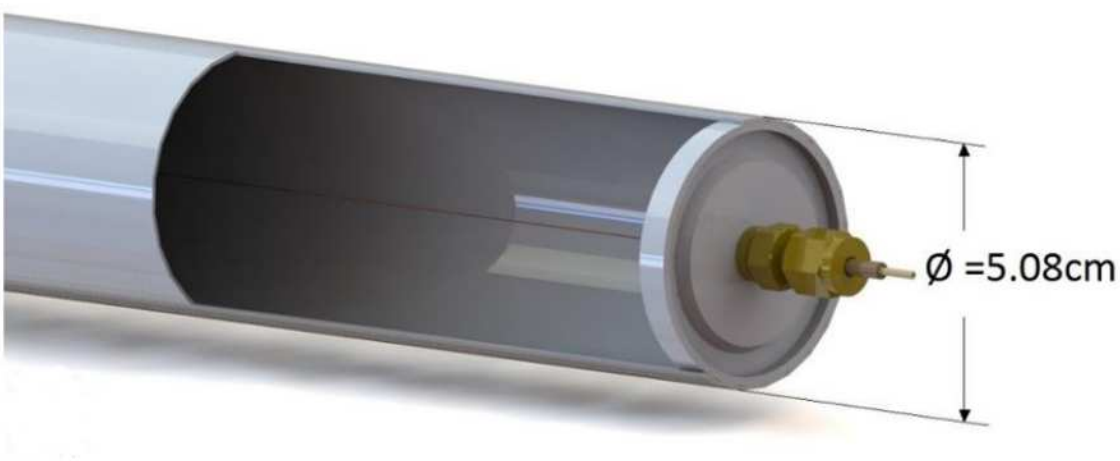

Figure 4.1: A model drawing of a single drift tube cutout to show interior and anode tungsten wire.

between the two. The resulting electric field within the tube has field lines that point radially from the anode wire to the aluminum tube wall; the magnitude of the electric field is proportional to $1/r$. As a cosmic-ray muon passes through the gas, it liberates electrons from the gas atoms which then drift along the electric field lines toward the anode wire. Once the electrons are within roughly 100 μm of the anode wire, the electric field is strong enough to accelerate the electrons to high enough energy that they collide with and liberate more electrons. The result is a cascade of electrons near the anode wire where the field is the strongest, causing a voltage pulse that can be read out from the end of the drift tube. The voltage pulse is fit to determine at what time in the data stream the electron cascade reached the anode wire. FPGA front-end electronics read from the tubes with a rate of 200 MHz. By knowing the drift time necessary for electrons to drift through the tube and create a pulse, the timing information of a tube is used to determine the radius of closest approach of the muon.

Each MMT module has 2 layers of 12 tubes that are offset by one tube radius. The offset is used to constrain the muon track to one side of the anode wire in the drift tube. Two modules placed side by side create a single detector plane with

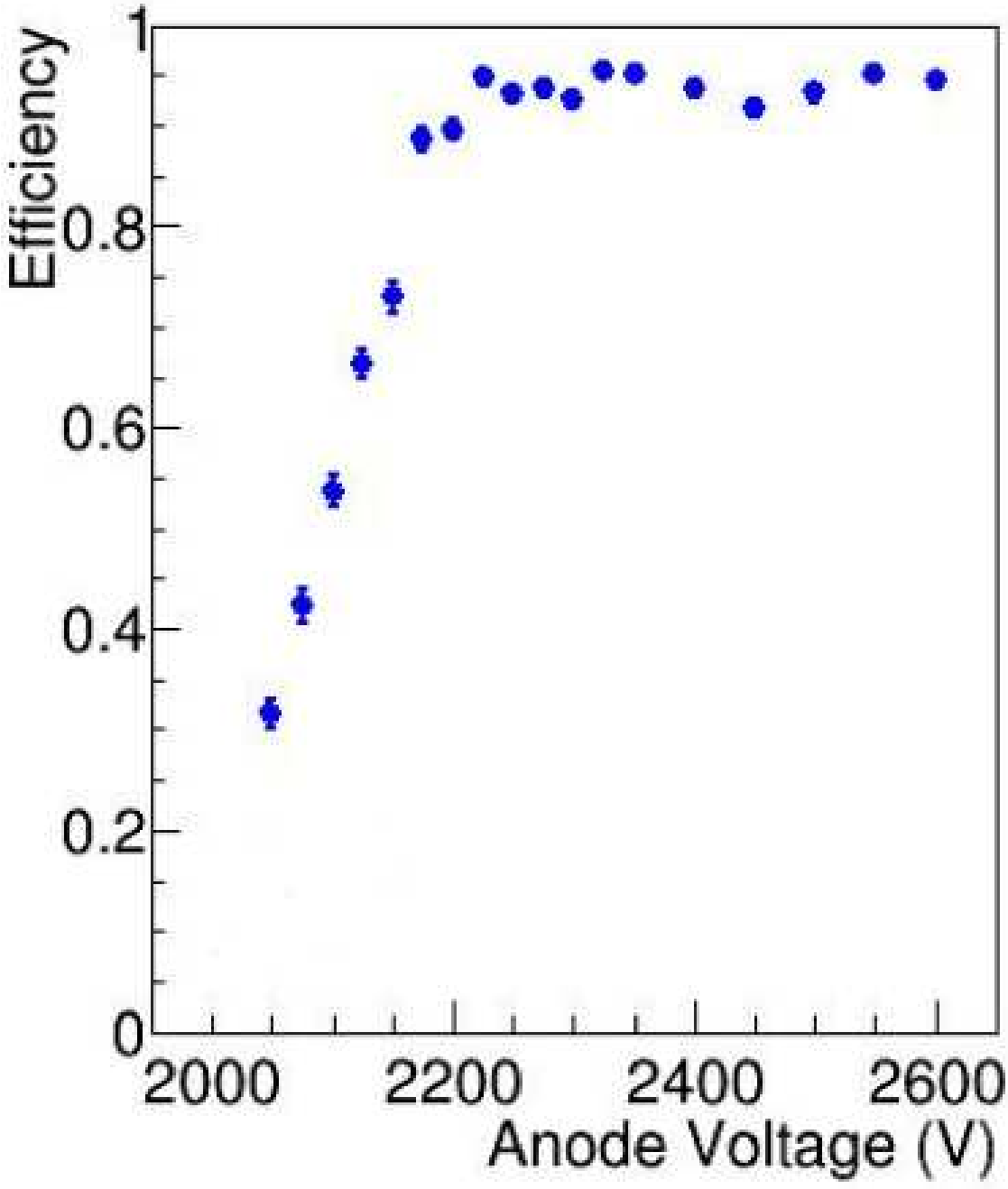

Figure 4.2: A plot of the MMT's drift tube efficiency as a function of the applied anode wire voltage.

spatial resolution in the direction perpendicular to the anode wire. By alternating the orientation of each plane by 90 degrees, a supermodule is able to measure the muon track in the x and y directions. By stacking 3 alternating x and y plane pairs, the supermodule has 6 planes (Figure 4.3) that measure the muon track's x and y position at 6 points in the z direction. When several tubes are pulsed within a 600 ns coincidence window, the timing information for all pulsed tubes is used with the drift time of the gas to constrain the path of the muon through those tubes (Figure 4.4) and create a muon track.

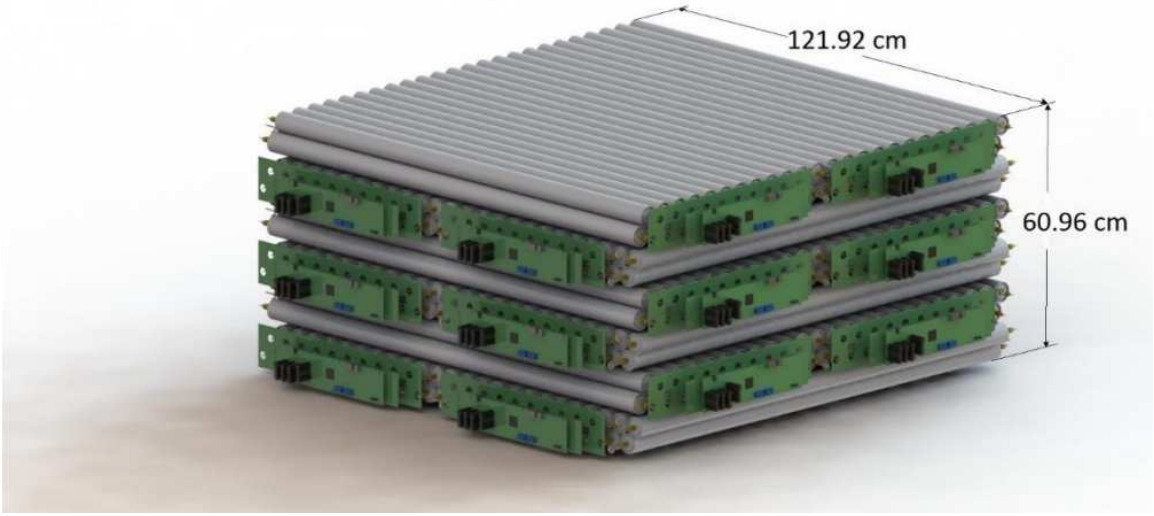

Figure 4.3: A model drawing of one MMT supermodule consisting of 6 planes with alternating drift tube directions.

Tracking the path of the moun in both the upper supermodule and the lower supermodule provides the data necessary to measure the muon's scatter between the detectors. If a muon is tracked in the upper supermodule but does not appear in the lower supermodule, it is assumed that the muon stopped via ionization loss between the two supermodules. Near the edge of a supermodule, it is possible for muons to scatter out of or scatter into a supermodule's active area without passing through the other supermodule. These events may be filtered out by requiring that the muon track in one supermodule is within the active area of the other supermodule when

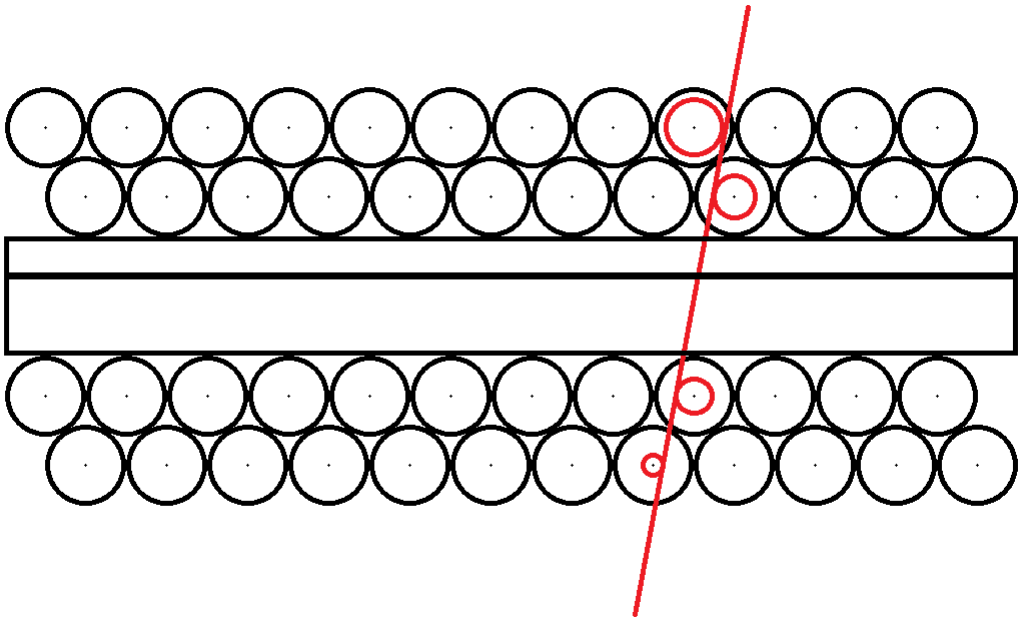

Figure 4.4: A conceptual side view of 3 MMT drift tube planes. The red circles represent the muon path's radius of closest approach in 4 of the tubes which are used to constrain the muon path.

projected to the other supermodule's position.

4.2 MC-10 Fuel Cask

A description of the geometry and materials composition of the Westinghouse MC-10 is found in [99]. The cask is a right cylinder with a height of 4.8 m and a diameter of 2.7 m. Inside, an aluminum basket made from 10.2 mm thick aluminum interlocking plates creates a grid of 24 cells. Each cell is large enough to house a single fuel bundle assembly. The basket is surrounded by an alloy steel cylinder for gamma shielding, with a 172.7 cm inner diameter and a wall thickness of 25.4 cm. Twenty four carbon steel fins are welded onto the outside of the steel shell and help to diffuse heat away from the cask body. Each fin runs vertically along the outside of the cask and has a thickness of 2.54 cm and a width of 23.2 cm. Additional shielding for neutrons fills part of the space between each cooling fin. BISCO NS-3 is used as the shielding; it extends an additional 6.35 cm beyond the steel shell and is covered by 6.4 mm steel

skin. A cutaway drawing of the cask from [99] is shown in Figure 4.5.

At INL, the MC-10 has been filled with Westinghouse 15×15 pressurized water reactor (PWR) fuel bundles. The fuel has a nominal burnup of 30,000 MWd and was removed from a US commercial power reactor in the early 1980s. The dimensions for each bundle is 21.4×21.4 cm^2 with a total height of 4.06 m, 3.66 m of which is fuel. The fuel rods are arranged in a 15×15 grid, with 204 grid cells containing fuel, 20 grid cells for reactor control rods, and 1 grid cell is reserved for in-core instrumentation. Each fuel rod has a diameter of 9.29 mm with a Zircaloy-4 cladding of 0.62 mm thickness.

Despite the gamma and neutron shielding of the MC-10, the radiation field at its surface from the fuel was measured to be 10 mrem/hr of neutrons and 10 mrem/hr of gammas. The radiation field created spurious hits in single drift tubes of the MMT, which swamped the data acquisition system with background data. To mitigate the noise from multiple drift tubes firing, an adjacent tube trigger was implemented in the MMT. The trigger required that only tubes that had a pulse in an adjacent tube within the 600 ns coincidence window be used for muon track reconstruction. In testing the MMT outside of the radiation field, the muon tracking rates decreased by $\sim 50\%$.

4.2.1 Simulation

In order to compare the results of the measurements of the MC-10 cask, simulations were performed using the simulation software package, Geant4[102]. The aluminum basket, gamma shielding, neutron shielding, cooling fins, steel skin, and fuel bundles were created for the simulation. Chemical composition for components was not included in [99]; however, the chemical composition used for each simulated component is given in Table 4.1. All dimensions for the simulated components were taken from [99], and a side by side comparison of cross-section drawings with cross-section

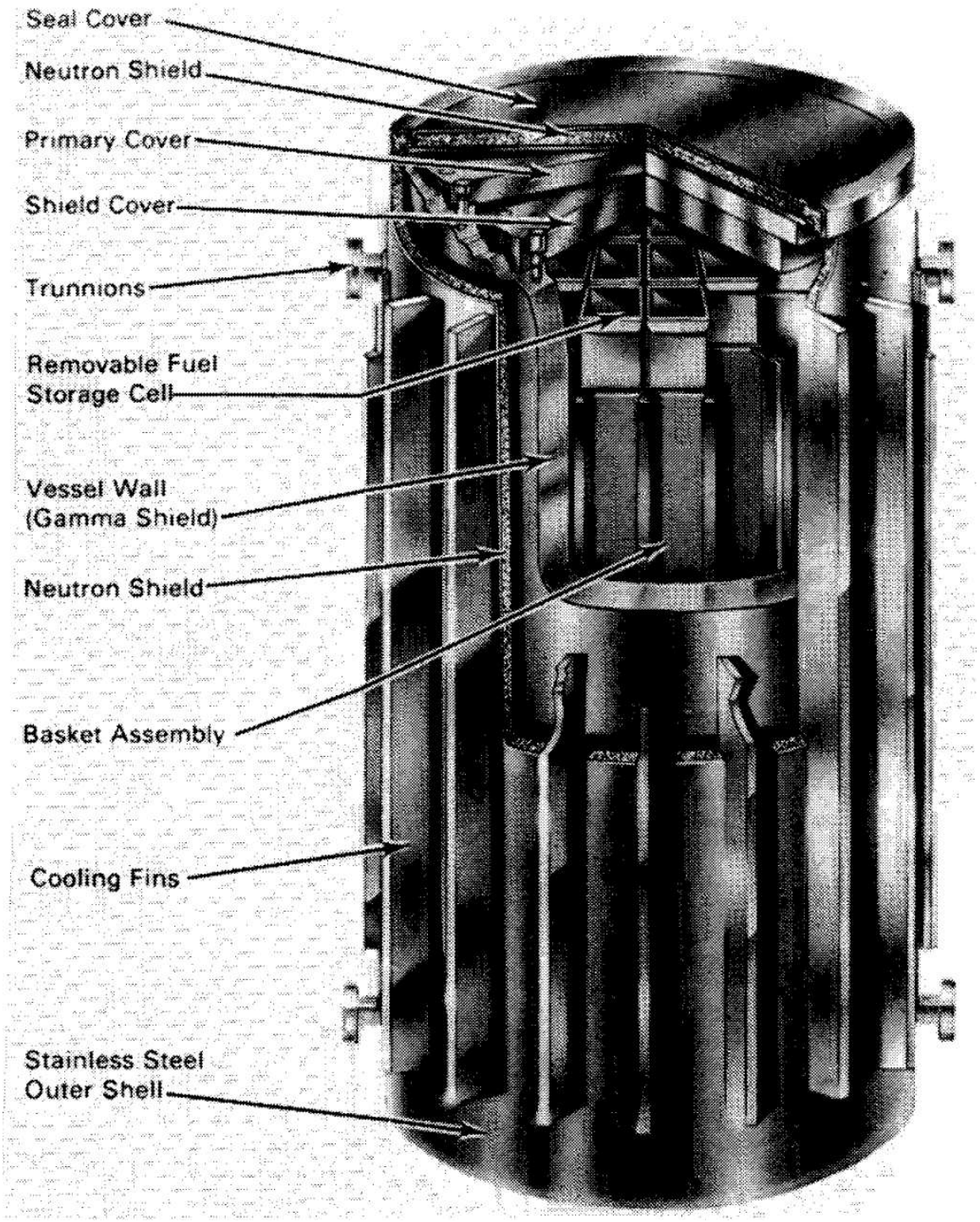

Figure 4.5: Cutaway drawing of the MC-10 fuel cask [99].

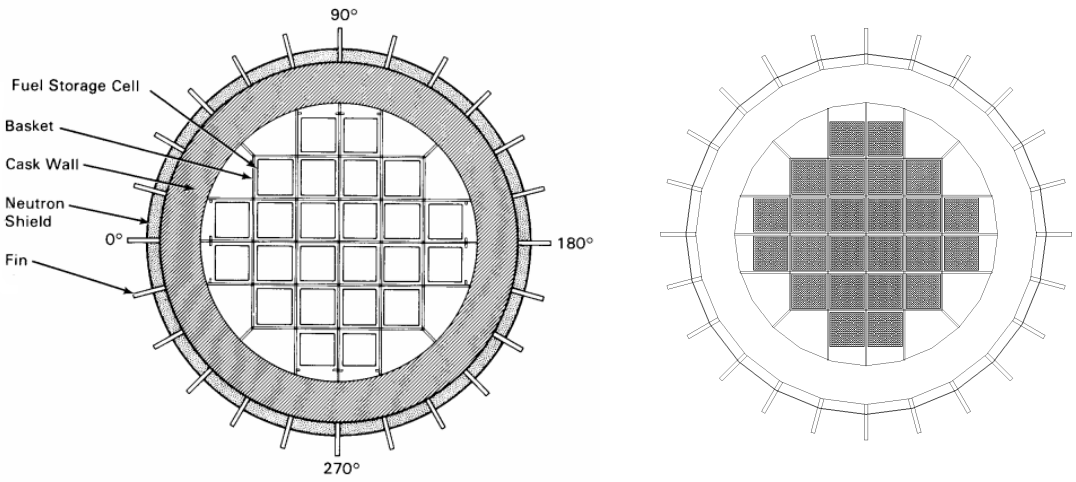

Figure 4.6: MC-10 cross-section from [99] (on left) and from simulation (right).

geometries from the simulation are given in Figures 4.6 and 4.7.

Component	Material	Composition [weight%]
Steel Shell Steel Skin Steel Fins	Steel Alloy	97.86-Fe, 1-Mg, 0.15-C, 0.9-S, 0.05-Si, 0.04-P
Neutron Shield	BISCO NS-3	58.38-O, 17.89-Al, 9.35-C, 5.61-Ca, 4.85-H, 3.36-Si, 0.56-Fe
Aluminum Basket	Aluminum	100-Al
Fuel Rod	Uranium Dioxide	88.14-U, 11.86-O
Cladding	Zircaloy-4	97.85-Zr,1.7-Sn, 0.19-Cr, 0.18-Fe, 0.08-Ni

Table 4.1: Chemical composition for each component of the simulated MC-10.

4.3 First Measurement

For the first measurement, a supermodule was placed on each side of and centered on the MC-10. Each supermodule was encased by a thin-walled and weatherproof enclosure to protect them from precipitation during the measurement. As shown in Figure 4.8, one supermodule was placed upon a 1.2 m tall aluminum support table.

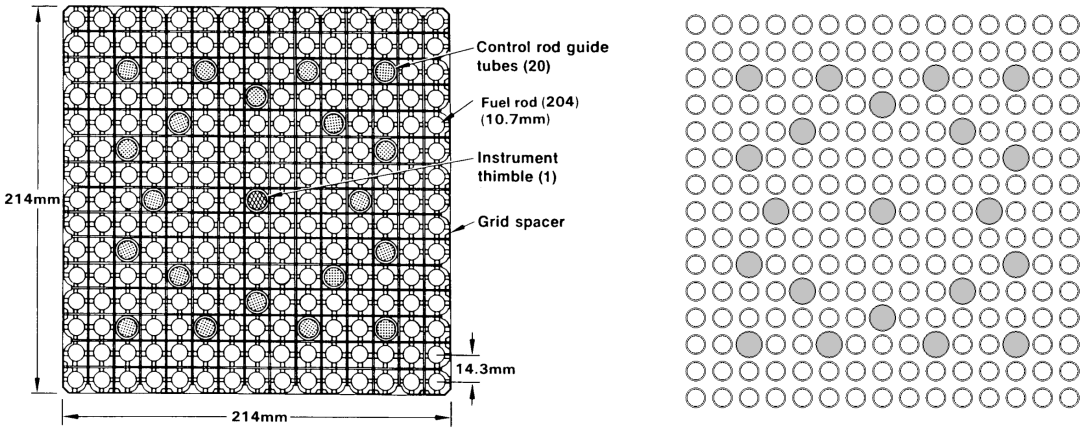

Figure 4.7: Westinghouse 15 × 15 PWR fuel bundle cross-section from [99] (on left) and from simulation (right).

This was done to sample from a smaller θ_z, thus increasing the muon flux according to the $\cos^2(\theta_z)$ distribution. Placement of the two supermodules also assured that the top or bottom of the loaded fuel did not enter into the field of view of the MMT. The size of a supermodule was not sufficient to give coverage of the entire MC-10 loading profile. Centering the supermodules on the cask allowed the detectors to cover the most interesting portion of the loading profile.

Figure 4.9 gives a top-down view of Idaho National Laboratory's MC-10's loading profile. The loading profile may be thought of in terms of the top-down view, with 6 columns and 6 rows of fuel bundles. Starting at the left and moving right, the loading profile for the MC-10 would be 0 out of 2 bundles in column 1, 1 out of 4 bundles in column 2, 6 out of 6 bundles in column 3, 5 out of 6 bundles in column 4, 4 out of 4 bundles in column 5, and 2 out of 2 bundles in column 6. Figure 4.10 shows the layout for each column of fuel bundles. Columns 2-5 with one, six, five, and four bundles respectively were within the MMT's field of view.

During the experiment, muons were measured passing through both supermodules at an average rate of ∼0.25 Hz. Data was collected for ∼200 hours, resulting in 1.62×10^5 recorded muons that passed through both supermodules.

Figure 4.8: Two weatherproof enclosures, each containing 1 supermodule. The near supermodule is elevated to increase the muon flux and decrease the counting time.

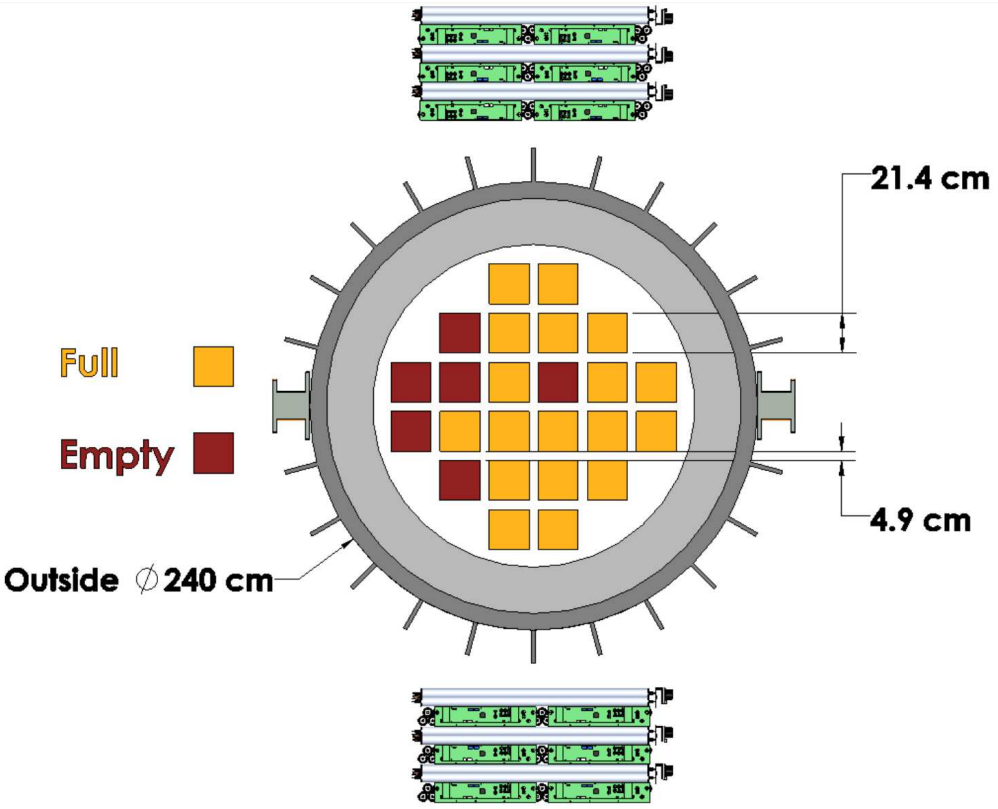

Figure 4.9: A top-down view of the measured MC-10's loading profile. Approximate locations and size of the two MMT supermodules are shown for comparison. The elevated supermodule is at the top of the image.

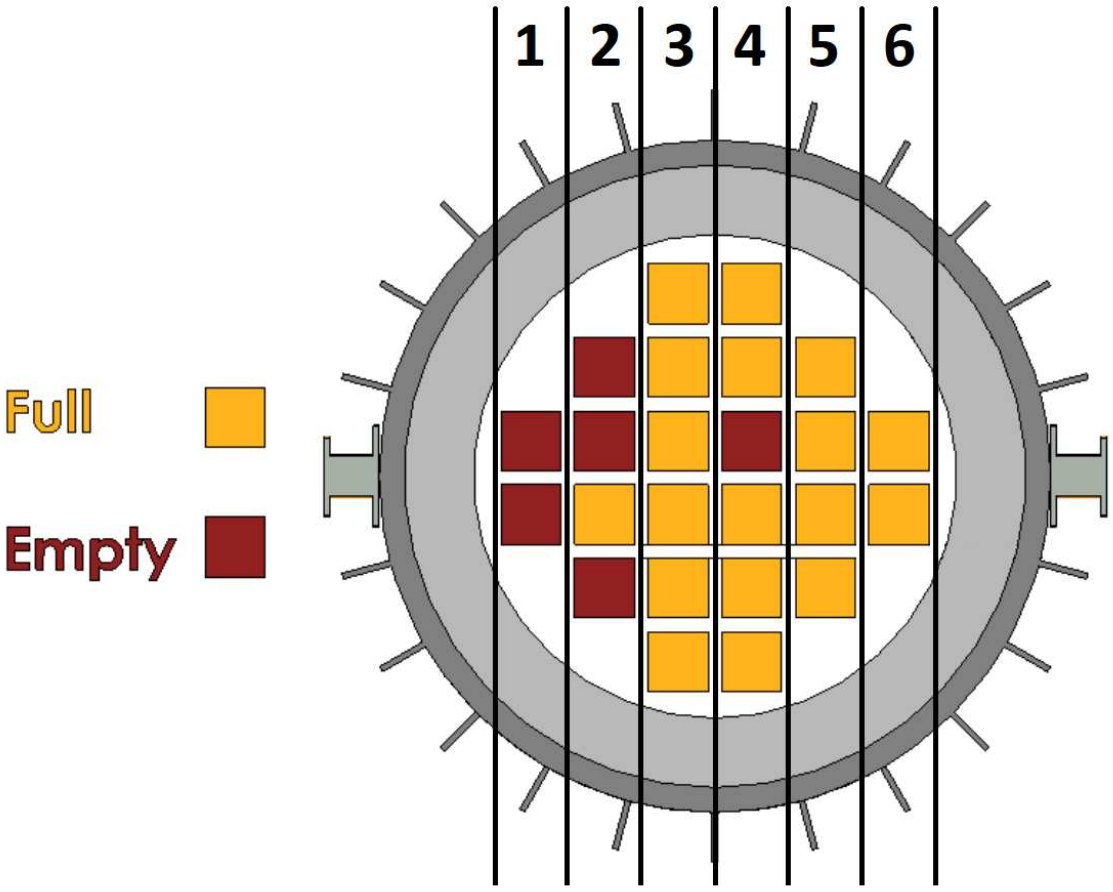

Figure 4.10: The loading profile of the MC-10 may be thought of as 6 columns with varying numbers of fuel slots and fuel bundles.

4.3.1 Analysis & Results

In order to compare the measured scattering data against different loading profiles, three Geant4 simulations were carried out. The loading profiles selected were: an identical partial defect profile, a fully loaded profile, and an empty loading profile. Each simulation was carried out with two muon detector planes, both had an active area of 1.2×1.2 m^2, placed to mirror the MMT supermodules' position relative to the MC-10. The detector planes recorded the simulated muon's position and direction, producing output comparable to the experimental data. Muon momentum and direction were determined by randomly sampling from the distribution described by the Reyna model. $10{\times}10^7$ muon trajectories were simulated for each loading configuration.

To analyze all of the scattering muon data, the muon tracks in the raised supermodule were projected forward to a virtual tally plane placed at the cask's center. The tally plane was divided into 2×2 cm^2 pixels. Each pixel had a corresponding scattering histogram which was filled with the scattering angles of the muons that intercepted that pixel. The resulting histogram of scattering angles was fit with the multi-group model to estimate the number of radiation lengths that the muons have passed through; referred to as areal density. An example of one of the scattering histograms and the resulting data is shown in Figure 4.11. Muon scatters that had angles greater than 200 milliradians were ignored for the fit since large angle scatters are more indicative of hard collision events of the muon with nuclei rather than multiple Coulomb scattering. An image with the same number of divisions as the tally plane was filled with the results of the multi-group fit. The analysis was applied to the experimental data and repeated for each of the three simulated fuel loading configurations. Figure 4.12 shows the obtained image for simulation and data.

An initial examination of Figure 4.12(a) quickly indicates that in column 2, where only one fuel bundle is present, the areal density is low relative to the other columns.

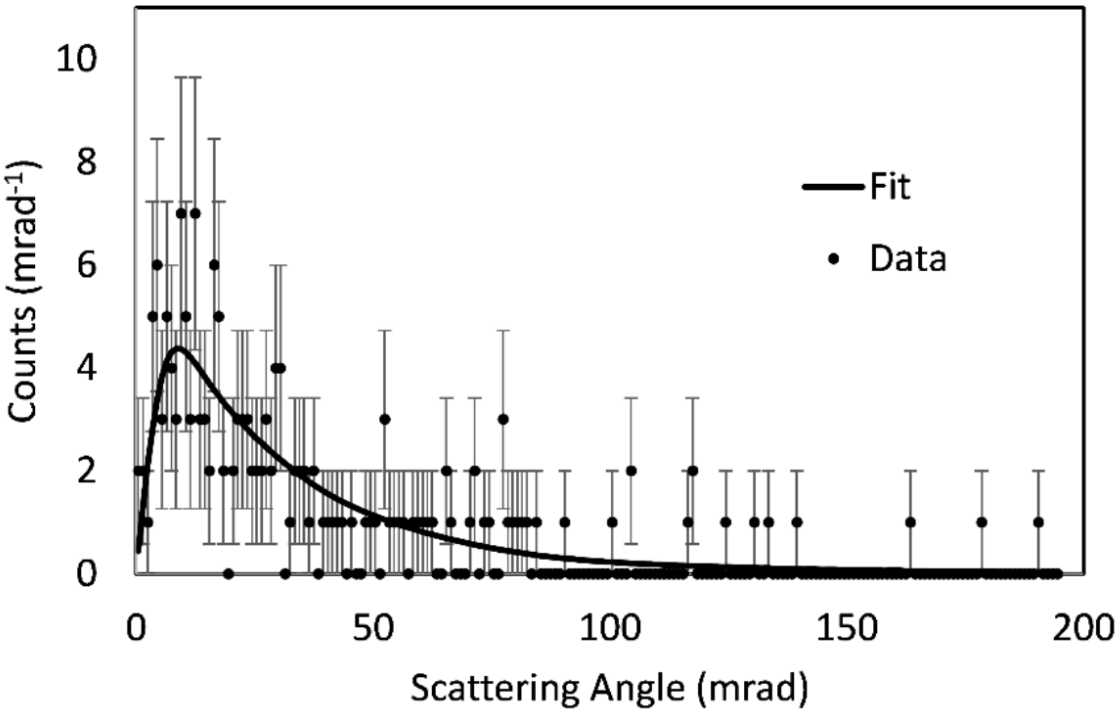

Figure 4.11: Histogram of muon scattering data as well as the multi-group fit. The fit provides an estimate of the areal density traversed by the muons that have passed through the cask.

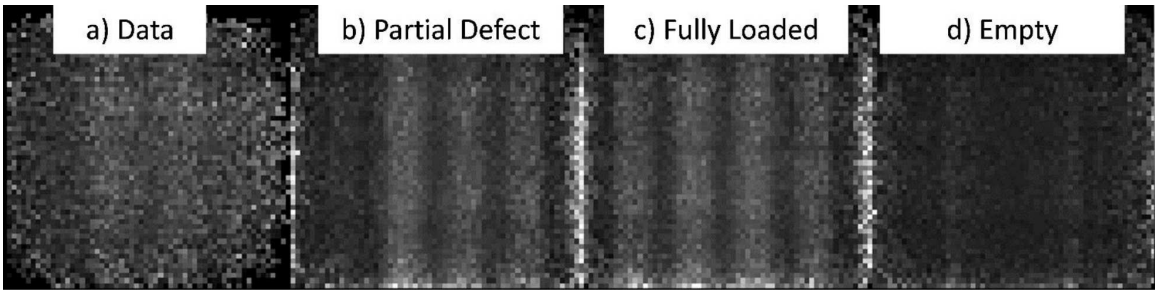

Figure 4.12: Image of the cask in terms of areal density for data taken on the MC-10 cask (a) and the three simulated loading configurations (b-d). Lighter grey scale values correspond to a larger areal density.

Visual comparisons of columns 3, 4, and 5 are less indicative of the number of fuel bundles in each column. Since the cask and fuel bundles are nearly uniform in the vertical direction, the scattering areal densities should not vary with height. Using this, the areal density in each image was summed vertically to create a one-dimensional profile of the cask. The integrated profile of data and simulation is shown in Figure 4.13.

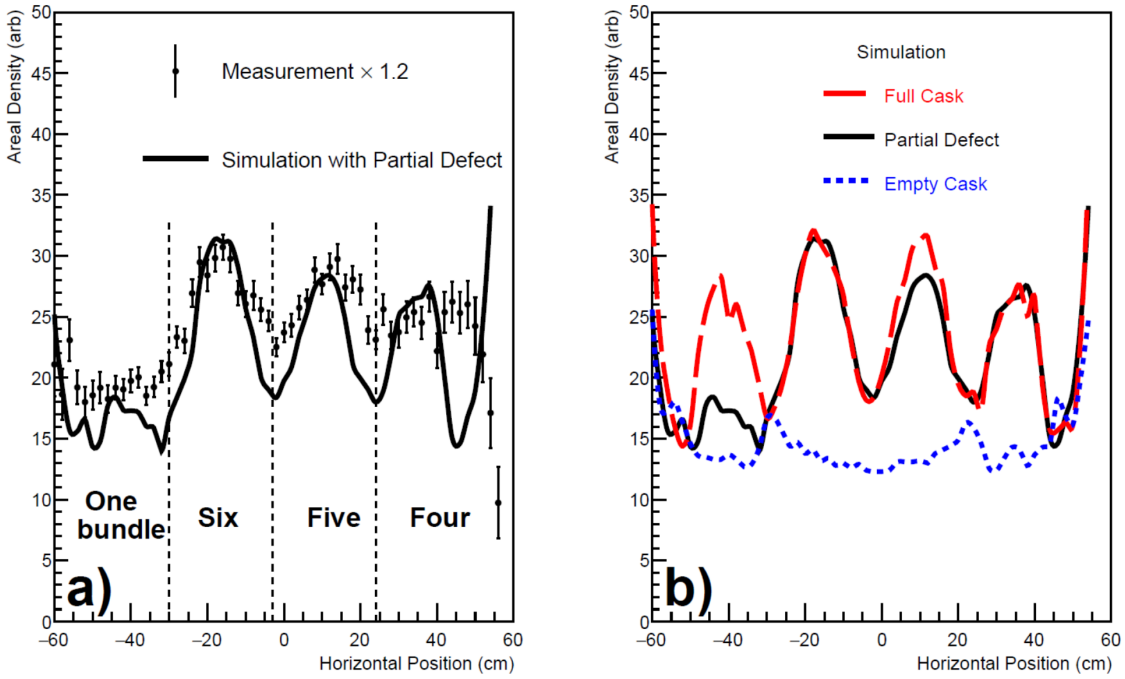

Figure 4.13: The estimated areal density through the MC-10 compared with a simulation of the identical loading profile (a). All simulation estimates are shown (b). Dashed lines show the approximate boundaries between fuel bundle columns.

Figure 4.13 gives a better indication of the relation between areal density and the number of fuel bundles within a column. The data were scaled by a factor of 1.2 in order to bring it in better agreement with the scale of the simulation. One potential explanation for the discrepancy is that the simulated muon momentum spectrum is different than that which passed through the MMT, resulting in differences of the Gaussian scattering width. Also, the simulation data contains artifacts near the edge of the tally plane. This is seen as higher grey scale values in Figure 4.12 and as upward

trends to unrealistic areal densities at the edges of Figure 4.13. These results most likely come from detector edge effects where in-scattering and out-scattering can over contribute to the tails of the Gaussian scattering distribution. However, simulation gives a good indication of what the predicted areal densities through the cask are.

The densities predicted by measurement appear to be a convolution of the densities predicted by the simulation. This could be the result of the MMT supermodules not being well aligned with the fuel bundle columns within the MC-10, creating an overlap between the fuel columns. It is also possible that the supermodules were offset from the center of the cask. Creating a tally plane that was offset in angle would also produce a similar result. Additionally, no account was given for detector efficiency which is not uniform across a supermodule but can change depending on the efficiency of each tube. The efficiency also falls off near the edges of a 48 tube module creating low-efficiency holes in a supermodule plane, where horizontal and vertical module edges overlap. Efficiency artifacts due to the adjacent tube trigger are also a concern. Still, this experiment was the first to actually measure muon scatter through a spent dry storage cask and it readily indicates that cosmic-ray muon tomography is able to identify multiple missing fuel bundles.

4.4 Second Measurement

A second measurement campaign was carried out at INL on the MC-10 to try and overcome the shortcomings of the first measurement and increase sensitivity to a single missing fuel bundle. For this measurement, care was given to verify that the supermodule planes of the MMT aligned well with the MC-10. The lifting trunnions at the base of the MC-10 were used as references points for the alignment; one can be seen at the bottom of the cask in Figure 4.14. Exposure time for the experiment was also increased. Rather than collecting data only on the center of the MC-10, additional positions to the side of the MC-10 were included and are illustrated in

Figure 4.15.

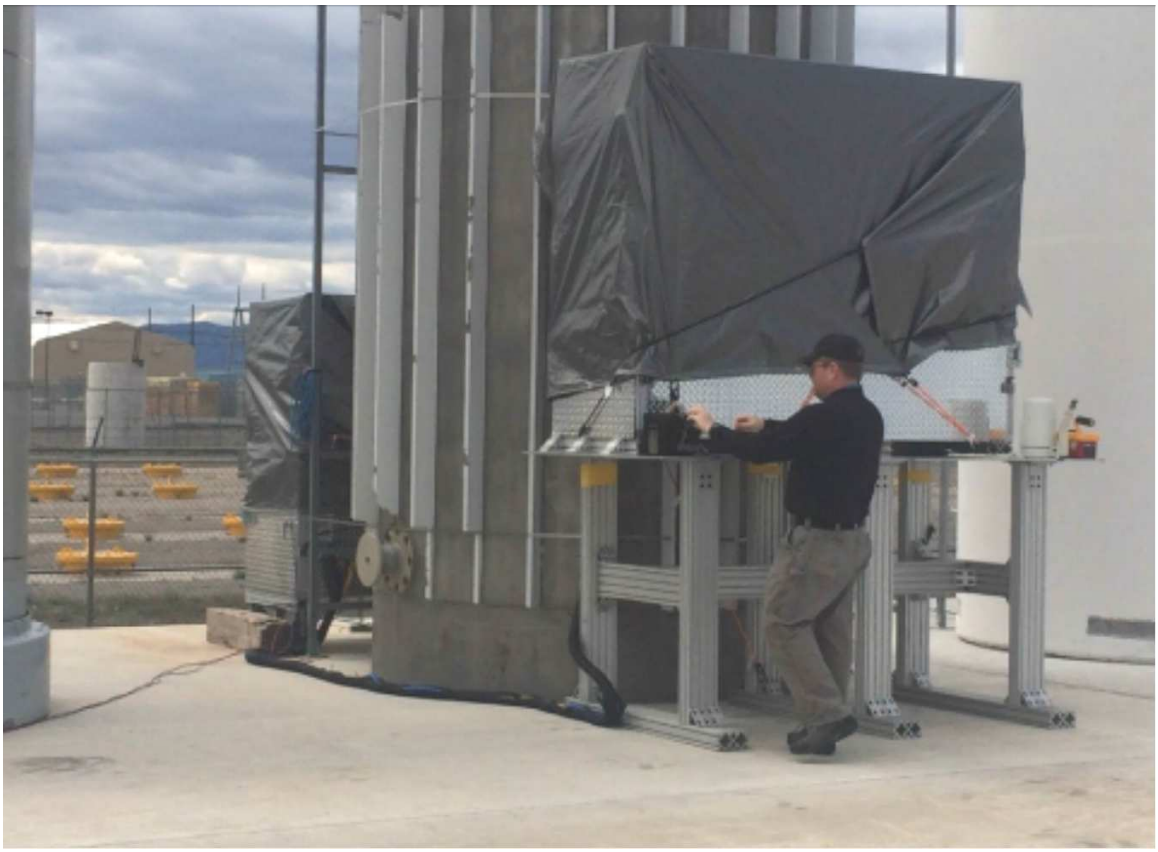

Figure 4.14: Both supermodules in new weatherproof containers around the MC-10.

4.4.1 Data Alignment

Taking measurements in multiple positions required that one supermodule not be moved between consecutive exposure times. As a result, the complete data set consisted of 9 subsets, one for each position pair. The complete data set was aligned by locking the position of the detector which had remained stationary between the two subsets and allowing the other detector to move in orientation and position. Aligning each subset sequentially brought all the data into alignment. Since each muon track contained a three-dimensional direction vector and a three-dimensional position vector for each supermodule, alignment of the data occurred in two steps: alignment of the directional vectors and alignment of position.

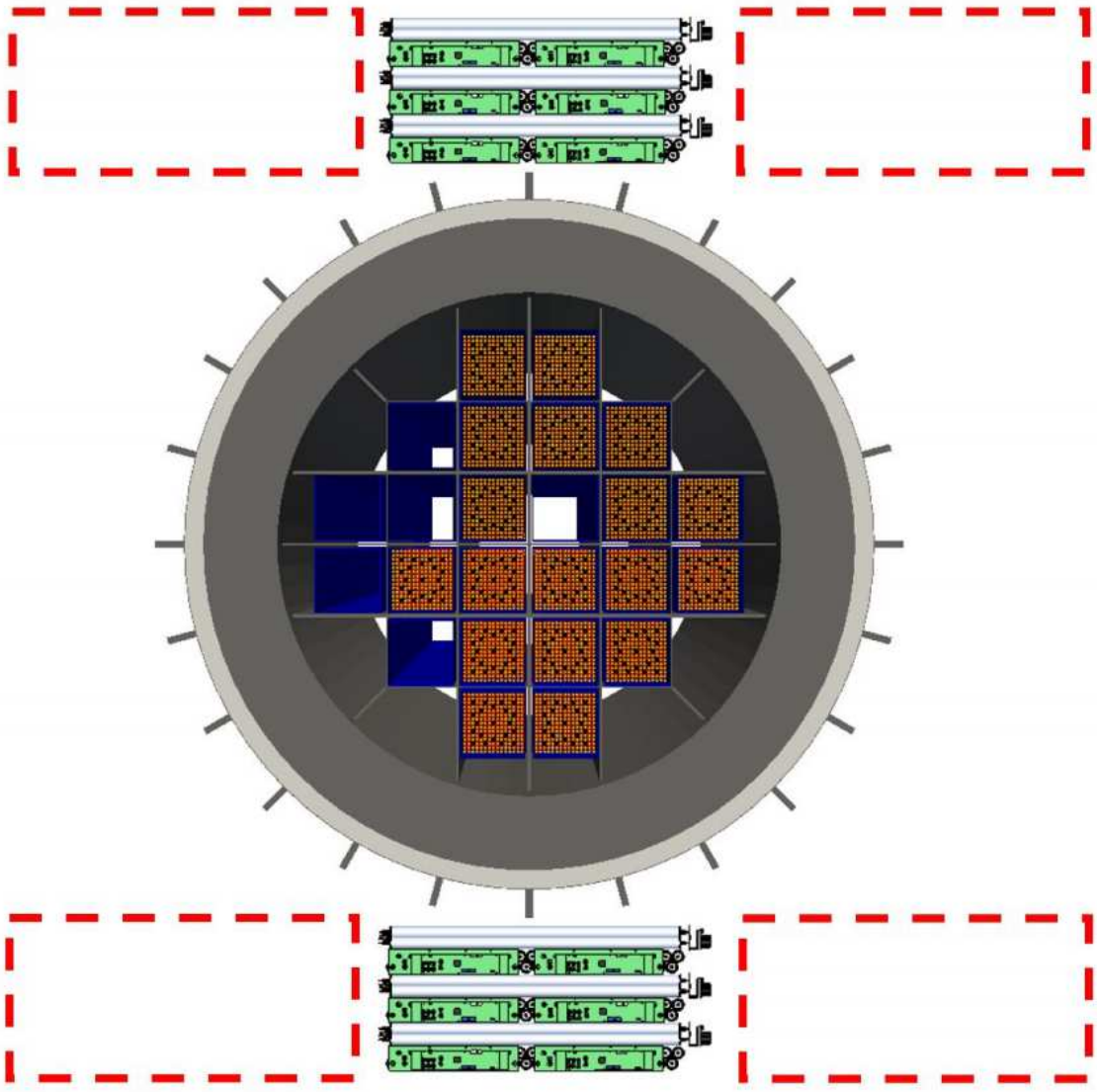

Figure 4.15: Planned positions for top and bottom supermodules relative to the MC-10.

As mentioned before, muon scattering has no directional preference. The result is a mean zero scatter, though the width of the scattering distribution changes. By aligning the directional vectors in the upper and lower supermodule, the optimal rotational alignment was found. A method of least squares alignment for two correlated vector sets is presented by Sorkine and Alexa in [103]. For the two groups of directional vectors the least squares residual is written as

$$\epsilon_R^2 = \sum_i (\boldsymbol{d}_{s,i} - \boldsymbol{R}\boldsymbol{d}_{f,i})^T (\boldsymbol{d}_{s,i} - \boldsymbol{R}\boldsymbol{d}_{f,i}), \tag{4.1}$$

where $\boldsymbol{d}_{s,i}$ is the directional vector of the ith muon track in the stationary supermodule, $\boldsymbol{d}_{f,i}$ is the direction vector of the ith muon track in the free supermodule, and $\boldsymbol{R}$ is the rotation matrix that describes the rotation to align the two vector sets. The rotation matrix $\boldsymbol{R}$ that minimizes ϵ_R^2 may be found by first calculating the covariance matrix of $\boldsymbol{C}$,

$$\boldsymbol{C} = \sum_i \boldsymbol{d}_{f,i} \boldsymbol{d}_{s,i}^T, \tag{4.2}$$

and finding its singular value decomposition:

$$\boldsymbol{C} = \boldsymbol{U}\boldsymbol{\Sigma}\boldsymbol{V}^T, \tag{4.3}$$

where $\boldsymbol{U}$ and $\boldsymbol{V}$ are unitary matrices and $\boldsymbol{\Sigma}$ is a diagonal matrix with diagonal entries corresponding to the singular values of $\boldsymbol{C}$. The rotation matrix R is given by:

$$\boldsymbol{R} = \boldsymbol{V}\boldsymbol{U}^T. \tag{4.4}$$

Once R is known, it is used to rotationally align the data for the free supermodule. After all data is rotationally aligned, translational alignment was calculated. The

translational alignment was determined by defining a residual

$$\epsilon_T^2 \equiv \sum_i \Big[\left(\boldsymbol{r}_{f,i} + \boldsymbol{O} - \boldsymbol{p}_{s:f,i}\right)^T \left(\boldsymbol{r}_{f,i} + \boldsymbol{O} - \boldsymbol{p}_{s:f,i}\right) + \left(\boldsymbol{r}_{s,i} - \boldsymbol{p}_{f:s,i} - \boldsymbol{O}\right)^T \left(\boldsymbol{r}_{s,i} - \boldsymbol{p}_{f:s,i} - \boldsymbol{O}\right) \Big], \tag{4.5}$$

where $\boldsymbol{r}_{k,i}$ is the position of muon track i in detector k, $\boldsymbol{p}_{k:j,i}$ is the projection of muon track i from detector k to detector j, and $\boldsymbol{O}$ is the offset correction for free detector. The value of $\boldsymbol{O}$ which minimized ϵ_T^2 was chosen as the nominal translational alignment for the supermodules.

Data collection lasted approximately ten days for each position with data sizes ranging from 4×10^4 to 9×10^4 muon tracks. During the run, winds were strong enough to move the lower supermodule which disrupted the ability to properly align the data from the final three positions with the rest of the data. As a result, data from the final three positions were not used in the analysis. The data used for analysis was collected from the positions shown in Figure 4.16.

4.4.2 Analysis & Results

As with the previous measurement, Geant4 simulations were used to compare the actual data against the expected results for different loading profiles. Fully loaded and empty loading profiles were simulated, using two muon detector planes which were centered on the cask. The muon detector planes were offset in height by 1.2 m; each had an area of 1.2×6 m^2. The large detector areas allowed the simulation to cover all positions used in the experiment. Both simulations generated 10^7 muons. The low momentum model was used to randomly generate each muon's angle and momentum. This was done to try to improve the factor of 1.2 that had been used to align simulation and data in the first experiment.

Data from the measurement at INL contained different quantities of muon tracks

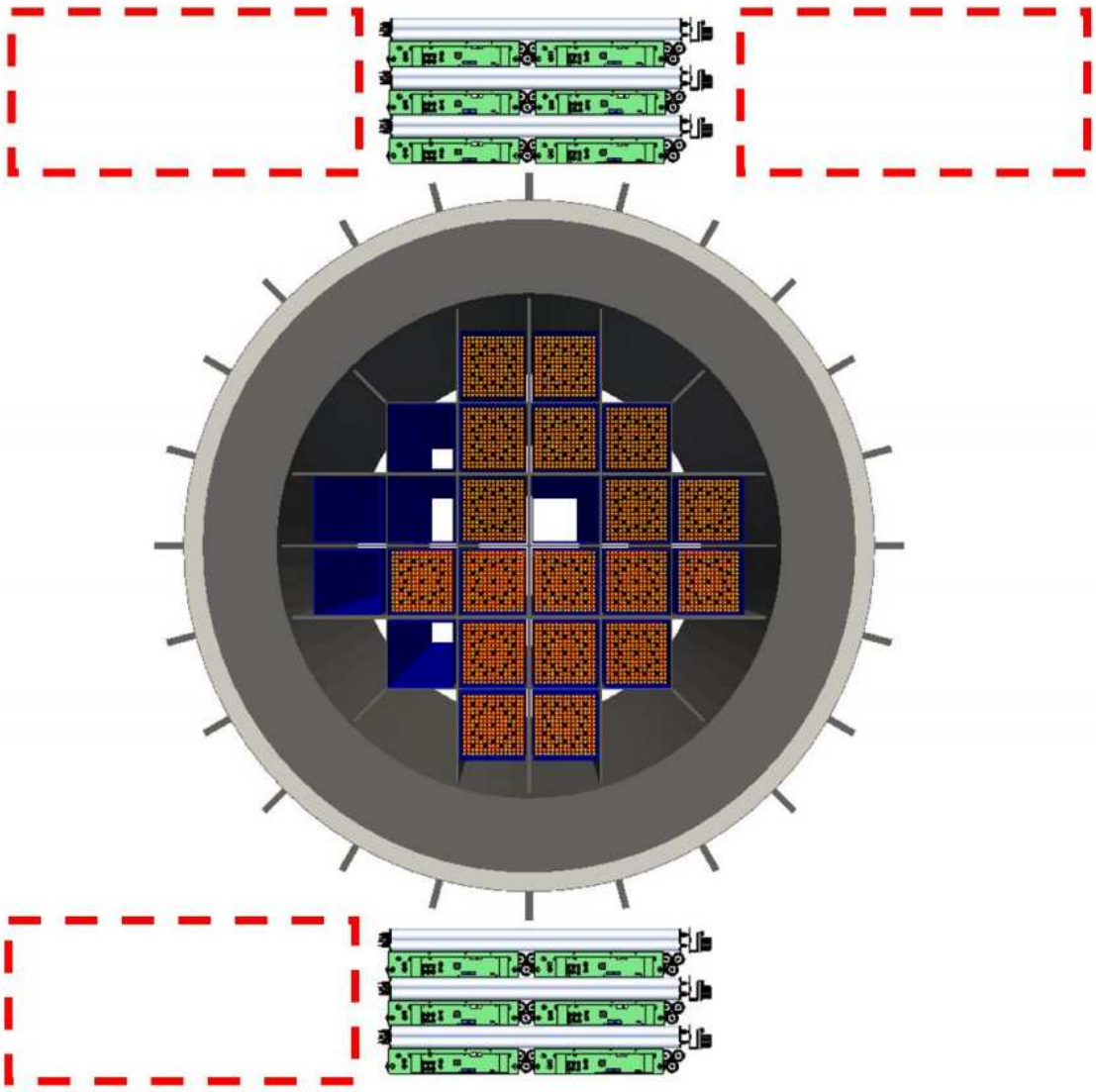

Figure 4.16: Used positions for top and bottom supermodules relative to the MC-10.

which were dependent on the solid angle between the detectors, the amount of time spent in each position, and detector efficiency. The adjacent tube trigger amplified the effects of dead tubes in the MMT supermodules and thus enhanced dead areas in each supermodule. These effects were accounted for in simulation by creating a mask from the INL data. The mask was applied to the simulation data to ensure that only data that overlapped with active areas in the MMT supermodules were used. This masking helped to ensure that the simulations reflected the asymmetries that arose from defects in detector acceptance.

Analysis of the data was similar to that of the first measurements, with a few notable exceptions. First, rather than a muon tally plane located at the center of the cask, a tally volume was used. The volume was divided into voxels with heights that surpassed the field of view of the MMT, widths of 2 cm in the horizontal direction, and 4 cm in the direction between the two detectors. Corresponding scattering histograms were assigned to each voxel. Muon tracks were projected from the upper supermodule to the tally volume. Each voxel that the muon traversed had its corresponding scattering histogram filled with the muon's scattering angle, weighted by the path length of the muon through that voxel. There was uncertainty about the absolution position of the muon due to multiple Coulomb scattering, and so adjacent voxels also had their histograms filled with the same weighted scattering value. For simulation, an additional step was taken to account for statistical bias introduced by different muon counts for each position. Simulation data had an additional weighting factor for each voxel corresponding to the number of counts in that voxel for each position in the actual data set. Average muon scattering values for each histogram were plotted as a function of horizontal position across the cask as shown in Figure 4.18. The curves from the simulations were normalized by a factor of 0.89 ± 0.01 to match the data over the range inside the cask steel shielding, where contributions from fuel are negligible.

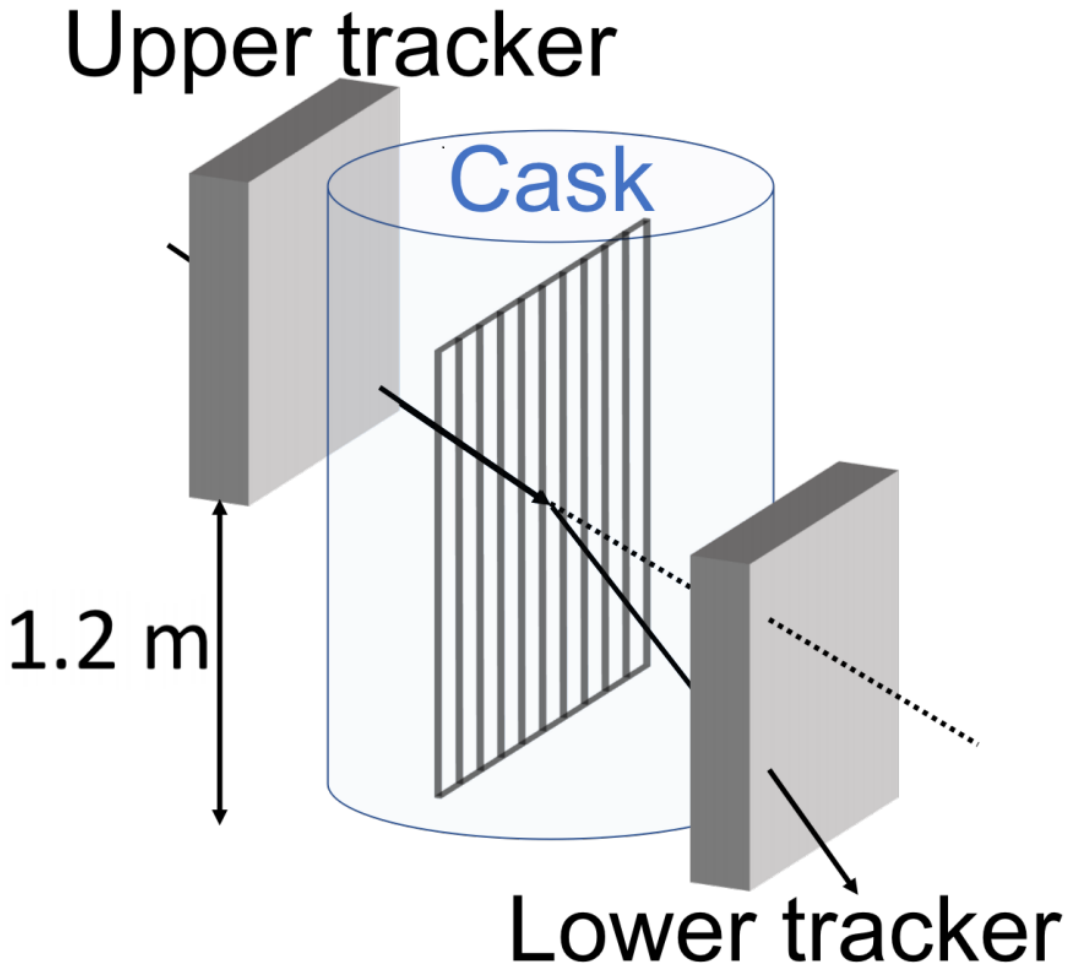

Figure 4.17: A muon track from the upper supermodule is projected to the tally volume. The histograms for the intercepted voxel and adjacent voxels are filled with the muon scattering angle.

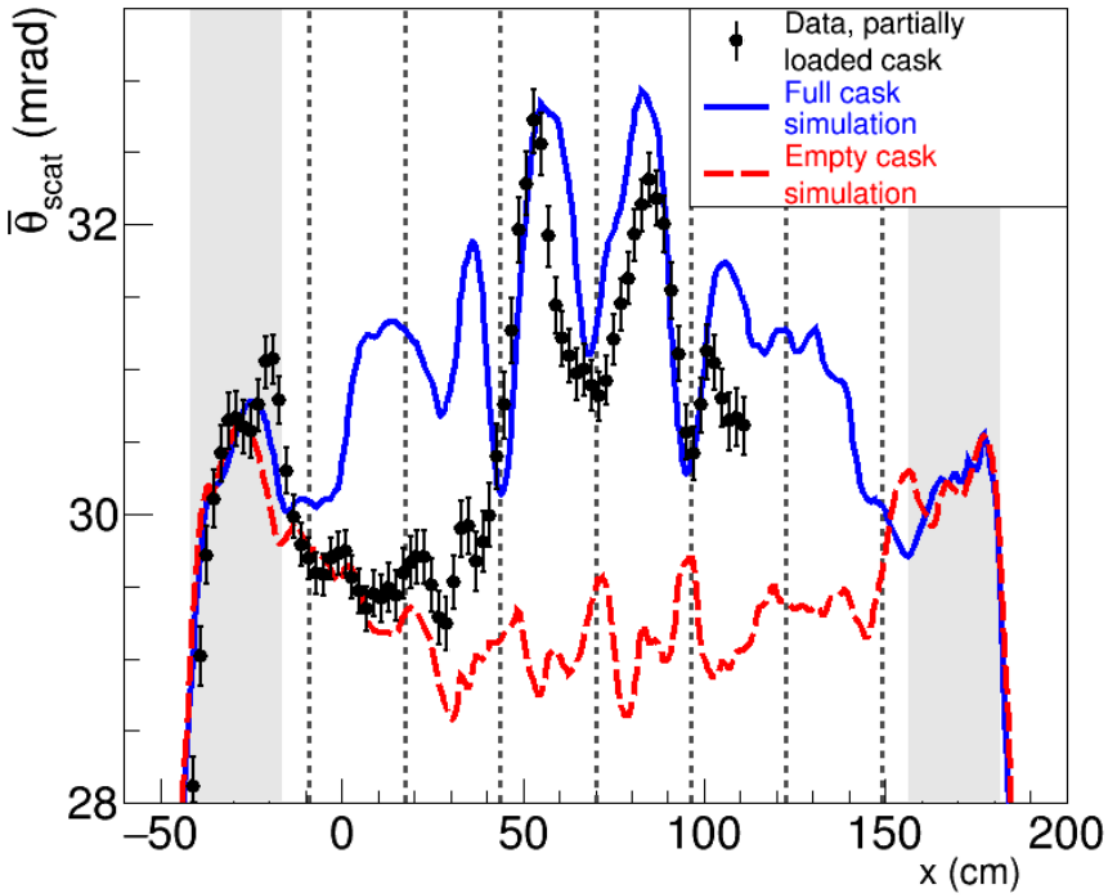

Figure 4.18: The average muon scattering angle as a function of horizontal position across the cask. The grey shaded areas indicate the inner and outer boundaries of the 25-cm steel shielding around the fuel, and the boundaries of the columns in the fuel basket are denoted by dashed lines. The Geant4 simulations of muon scattering in a full/empty cask is shown by the solid blue/dashed red line.

In the leftmost shaded area, a peak is seen due to scattering in the 25-cm steel shielding surrounding the basket. The precision on the features in the first two columns of fuel bundles is limited by statistical uncertainties, but there is evidence for a slight dip in the first column which contains no fuel, as opposed to the two assemblies that would be present in a full cask. The data here are consistent with the expectation for an empty cask from the simulation. In the region of the second column, a small peak corresponding to the single fuel assembly is seen which has an average scattering magnitude between the expectations for a full and empty cask. This indicates a column which is partially filled with fuel instead of containing four assemblies. The third column, which is fully loaded with six bundles, shows a clear peak with an amplitude that is consistent with the simulation of a full cask and is larger than the next two columns containing five and four bundles, respectively. The fourth column, which contains only five fuel assemblies rather than the full six, shows a peak with an amplitude smaller than the expectation for a fully populated row; this is indicative of a single missing fuel bundle. Column five is fully loaded with four bundles and displays some disagreement with both the full and empty simulation. However, this does not contain the full data set, due to data that was removed from the final three positions. This limitation on data precludes strong conclusions about fuel bundle content in the fifth column.

For a quantitative comparison, the scattering signal from Figure 4.18 was averaged across the boundaries of each column of fuel bundles. The complete measured data set and simulated data are shown in Figure 4.19. The vertical error bars indicate the statistical uncertainty, and the horizontal bars show the range over which the averaging was performed for each fuel bundle column. Simulation of the full cask shows a maximum scattering at the center of the cask where muons pass through the most fuel. Asymmetries between the sides of the cask with the same fuel content are due to the nonuniform angular acceptance of the detectors and the weights that are

applied to each simulated measurement position to accurately reflect the instrument's active area and measurement times.

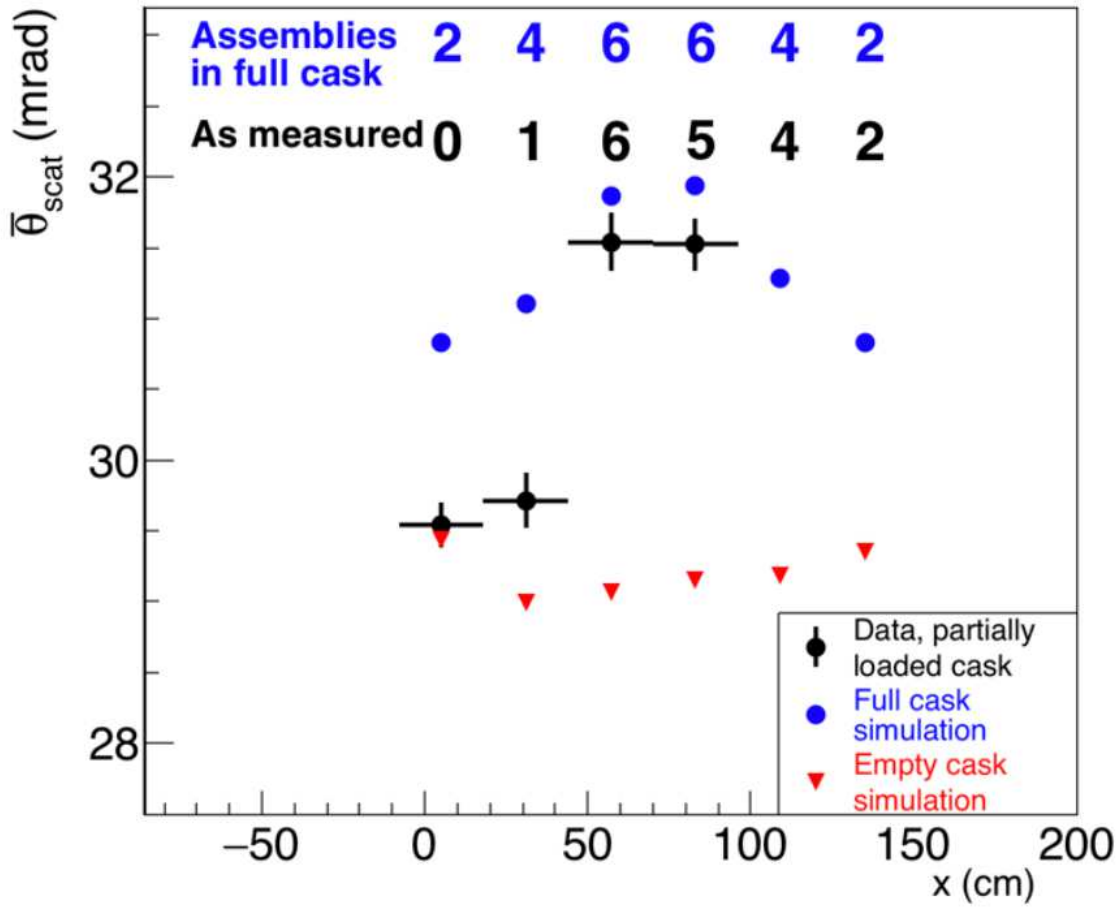

Figure 4.19: The muon scattering signal averaged across the positions of each column of fuel bundles, for measurement and simulation data. The number of assemblies in each column for the full cask and actual loading profile as measured are indicated in the text.

The empty cask simulation shows minimal scattering near the center of the cask, where the trajectories of muons moving from one supermodule to the other are nearly perpendicular to the steel gamma shielding and sample the least path length through this material. On the edges of the cask, where the path length through the curving wall of the 25 cm gamma shielding in the cask is a maximum, the empty cask simulation shows increased scattering.

Data from the first column of fuel bundles, containing no fuel, is consistent with

expectations for an empty cask. The second column shows a scattering signal that is above the expectation for an empty cask but is lower than the expected scattering in a full cask by 7 σ due to the three missing bundles in this column. Muon scattering in the third column, that is fully loaded with fuel is 1.6 σ lower than expectation from a full cask. While this level of disagreement has limited statistical significance, a slight deviation from the model of a full cask is expected. Some muon tracks projected to this column entered the cask and passed partially through the neighboring columns, which contain fewer fuel bundles than the full cask.

The fourth column, with a single fuel bundle missing, displays an average scattering that is lower than the full cask model by 2.3 σ. Most of the relevant data for this column was taken in the position with both detectors centered on the cask over a period of 10 days. If additional data were recorded, either by a more efficient detector or by increasing the exposure time, the uncertainty would decrease, providing much stronger constraints on the measured fuel content. In an actual verification scenario, this level of disagreement could be grounds for requesting additional measurements in this position, in order to draw stronger conclusions about the fuel content of this column.

The MMT is a general purpose instrument, that was not specifically designed for cask radiography. The active area of the supermodules was only able to cover less than half of the 2.7 m cask diameter in any single configuration. The size of the MMT supermodules limited the recorded flux of cosmic-ray muons, requiring 90 days of measurement time to acquire the data. Moving the MMT to different positions also compounded measurement difficulties due to limitations on cask access, as well as the additional forklift support required to move the elevated MMT supermodule and its table. High winds caused the lower MMT supermodule to shift during data taking, resulting in a loss of the continuity of the data coordinate system and the removal of the final three MMT positions from the data set. There were additional

issues due to some readout electronics falling out of the data stream, which required that they be replaced.

Though there were several obstacles during the measurement at INL, the results validate the utility of cosmic-ray muon tomography for verification of fuel content in a dry storage cask. Several of the obstacles, such as counting time, elevating one of the MMT supermodules, and requiring several MMT positions to image the entire cask could be overcome by using a larger muon detector. A sufficiently large muon detector would consist of two drift tube supermodules, similar to the MMT, but with a horizontal dimension extending beyond the width of the cask and a vertical dimension high that there would be relatively little gain in muon flux by elevating one supermodule. If a large detector were used, one position could cover the same positions recorded by the MMT and would require reduced counting time. It would also have the benefit of recording incident muon tracks from both sides of the cask simultaneously.

4.5 Conclusions

Two experiments measuring the multiple Coulomb scattering of cosmic-ray muons in an MC-10 dry cask were carried out at Idaho National Laboratory using the Los Alamos National Laboratory's Mini-Muon Tracker. The analyzed data indicated that measurements on spent fuel dry casks, using cosmic-ray muon scattering, can be used as a stand-alone method to independently determine if fuel assemblies are missing. In order to obtain statistically significant results and draw conclusions about the cask contents, count times of weeks to several months may be needed. However, spent fuel casks are designed to have a working lifetime of several decades, during which they typically sit undisturbed at storage facilities. Several months of measurement time is not expected to pose a significant impediment to operations at commercial fuel storage sites.

The data collected by the two INL measurements has been benchmarked against Geant4 simulation data. In both cases, a normalization factor was used to better align simulation with real data. It is likely that neither simulated muon spectrum accurately depicts the true momentum of incident muons. Accurate muon momentum measurements for momenta less than 10 GeV/c and at large zenith angle would likely be needed to better model the muon momentum distributions. However, the simulation data does correctly predict the shape of muon scattering profiles of the cask and should be sufficient to allow the Geant4 simulation to be used to investigate the muon scattering methods beyond what was possible with the MMT and MC-10 measurements.

Chapter 5

Computed Tomography Using Cosmic-Ray Muons

The measurements at Idaho National Laboratory (INL) produced data that approximated an integrated projection of cosmic-ray muon scattering in a spent fuel cask. By extension, it would be expected that several integrated projections at small angle intervals could produce a sinogram; from which, one can reconstruct an image via Filtered Back Projection, as mentioned in Chapter 3. A simulation study was carried out, using the same simulated MC-10 dry storage cask discussed in Chapter 4, in order to determine the feasibility of cosmic-ray muon computed tomography. The work presented here was published by the Los Alamos National Laboratory's Threat Reduction team in [104].

5.1 Simulation

The solid angle of the Los Alamos National Laboratory's Mini-Muon Tracker (MMT) allowed for a very limited view of the MC-10 dry storage cask. Rather than recreate two supermodule detector planes with similar solid angle coverage as the MMT, two cylindrical shell detectors were simulated and are shown in Figure 5.1. Each ring was 1.5 m high and had a radius of 1.68 m. The lower edge of the upper detector was situated 0.25 m above the center of the cask and 0.5 m above the top edge of the lower detector. Simulated muons were required to pass through the upper detector and be pointed at the lower detector (in order to be tallied in the data output). The detectors recorded the muon's position and direction with perfect spatial and angular

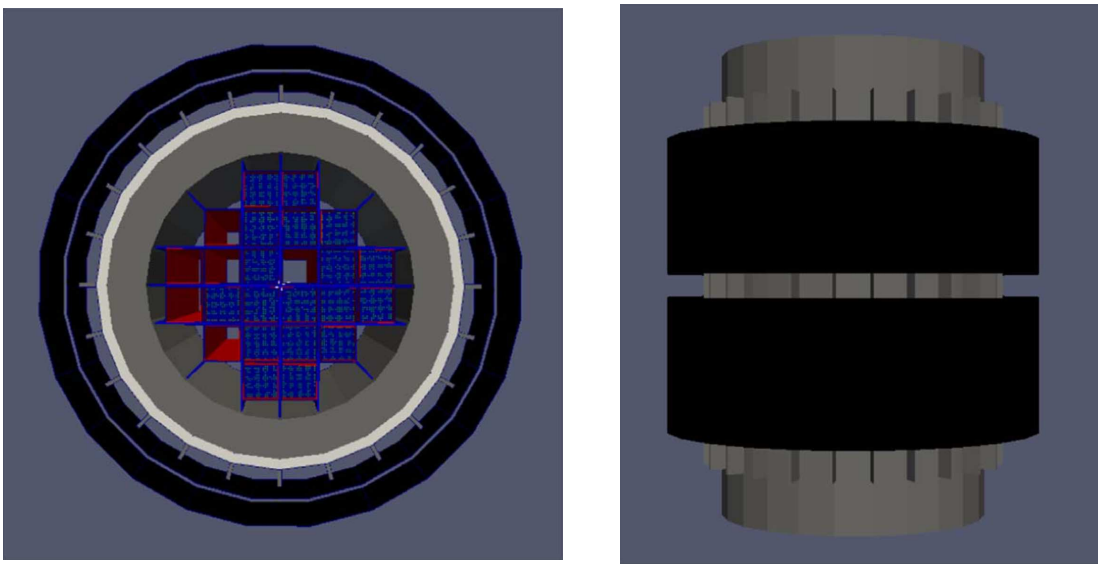

Figure 5.1: Top down view (left) and a side view (right) of the simulated MC-10 cask with two ring detectors. A loading profile identical to INL's MC-10 cask was used.

resolution. This was justified because muon scattering within the cask degraded the simulated data far more than the limiting resolution of a drift-tube or scintillation detector.

The low momentum muon spectrum model was employed for these simulations since it better simulates the low end of muon momentum. The low momentum muons are more likely to stop in the cask, which is critical for performing transmission measurements. In all, 1×10^8 muons were generated and aimed to pass through the cask. The counting time necessary to collect 1×10^8 muon tracks with the described detector geometry can be quickly estimated. Assuming that the muon flux distribution is given as

$$\frac{df}{d\cos(\theta)} = A\cos^2(\theta), \tag{5.1}$$

it is expected that

$$\int_0^1 \frac{df}{d\cos(\theta)} d\cos(\theta) = \int_0^1 A\cos^2(\theta) d\cos(\theta) = 1 \text{ muon cm}^{-2} \text{ min}^{-1}.$$

Integration produces an estimate of $A = 3$ cm^{-2} min^{-1} for the normalization factor. From the center of the cask, the observed azimuthal angle ranges from $\arctan(1.68/1.75) \simeq 44°$ to $\arctan(1.68/0.25) \simeq 82°$. Integration of the differential flux in 5.1 over the observed azimuthal angles predicts a rate of 0.372 cm^{-2} min^{-1} for incident muons in a 1 cm^2 area at the center of the cask. The simulation contained 1,018 muons projected to the 1 cm^2 area at the cask center, which is equivalent to 1.9 days of exposure. This prediction assumes a detector with perfect efficiency, though drift tube detectors should be 90% or more efficient. It is not unreasonable that an actual detector with similar solid angle coverage could produce a similar amount of data within a week of counting.

5.2 Analysis

The simulated scattering and stopped muon data were used to create two sinograms of the cask. This was done by projecting the incident muon track to a tally plane located at the center of the cask and was parallel to the cask's central axis. The tally plane was divided into 2 cm wide pixels, each of which had corresponding histograms and two integer counters. The scattering histogram recorded the scattering value for through-going muons that intersected the pixel. One of the counters recorded the number of all muons which intersected the pixel on the tally plane. The other counter only recorded the number of muons which intersected the pixel and also recorded the muon exiting the cask.

Rather than having a single tally plane for all of the data, 180 tally planes were created. The position of each tally plane was given as a function of φ, with φ being a counterclockwise rotation off of one of the horizontal axes–shown in Figure 5.2. The separation between adjacent tally planes was set to two degrees. Assigning the muon data to the correct tally plane required finding the angle φ at which the direction of the muon in the horizontal directions was perpendicular to a tally plane, within the

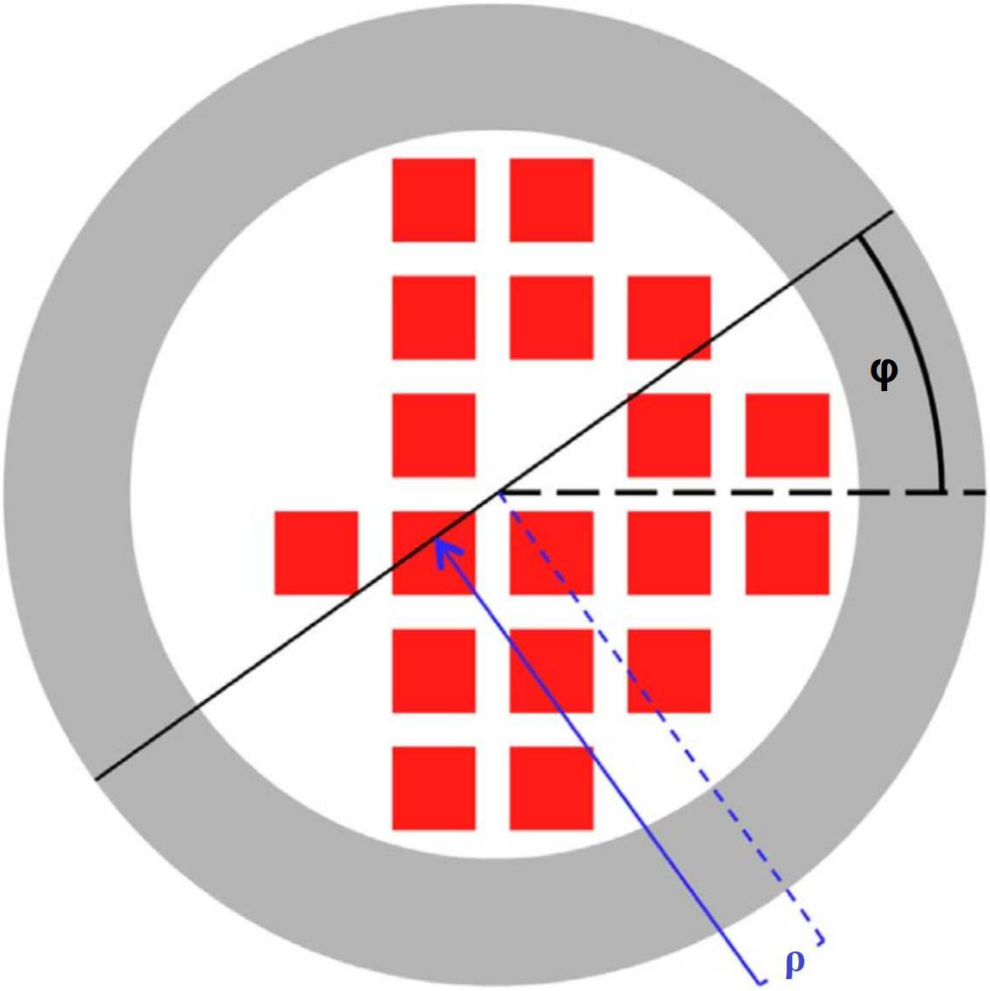

Figure 5.2: The projection of a muon path (blue arrow) to a central tally plane. Muon scattering histogram and counting values are filled according to the offset from the cask center (ρ) and rotation of the plane with respect to the cask (φ).

binning of 2 degrees.

Both scattering data and transmission data were analyzed. Each histogram of the scattering data was fit using the multi-group model, and the fit value for the areal density was used to fill a sinogram in ρ and φ. The two counter values for each pixel were used to calculate the transmission;

$$-\ln\left[\frac{N_{\text{out}}}{N_{\text{in}}}\right],$$

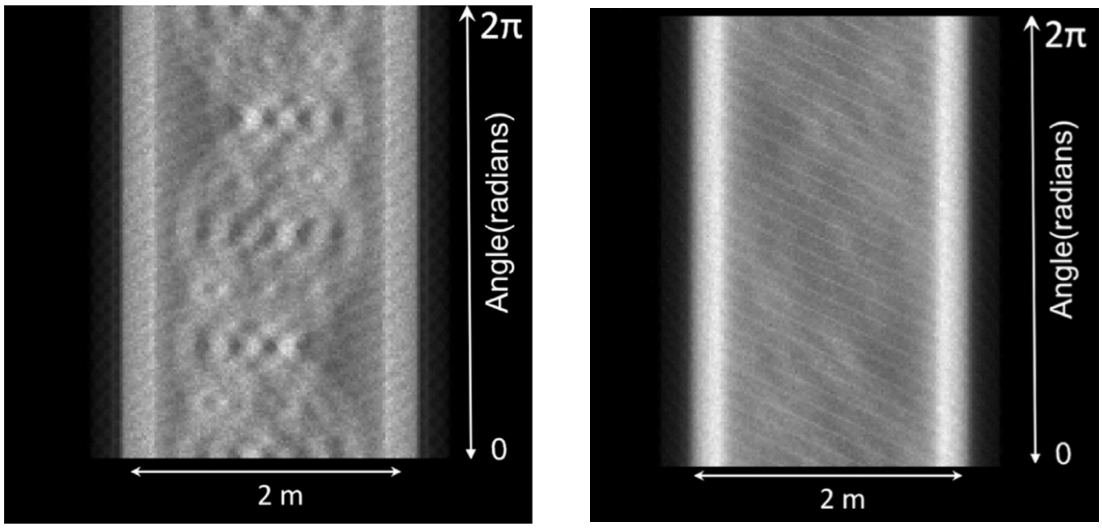

Figure 5.3: Two histograms created from the simulation data: areal density (left) and muon transmission (right).

where N_{out} was the number of muons that intersected the pixel and were detected exiting the cask and N_{in} was the total number of muons that intersected the pixel. The created areal density and transmission sinograms are shown in Figure 5.3. Sinograms typically have a φ range of $(0, \pi]$, due to ρ ranging $(-\infty, \infty)$, making the sinogram a mirrored duplicate as φ ranges from $(\pi, 2\pi]$. However, since the mean scattering angle θ_0 and rate of energy loss $dE/d\ell$ vary with the amount of matter that a muon has traversed, it is expected that any asymmetry in the cask geometry (likely due to fuel loading) would give rise to asymmetries in the scattering and transmission sinograms. In practice, the additional range would also increase the robustness of the method against detector flaws. For these reasons, the sinograms both cover φ over the range $(0, 2\pi]$.

The manner in which the sinograms were constructed assumed that the cask was uniform in the vertical direction, meaning that the sinogram and reconstruction will provide information only in the horizontal plane. Reconstructions from the sinograms are then thought of as a projection down the vertical axis of the cask and its contents. Reconstructions of both sinograms into two-dimensional images was performed via filtered back projection using the ramp filter and are shown in Figure 5.4. The

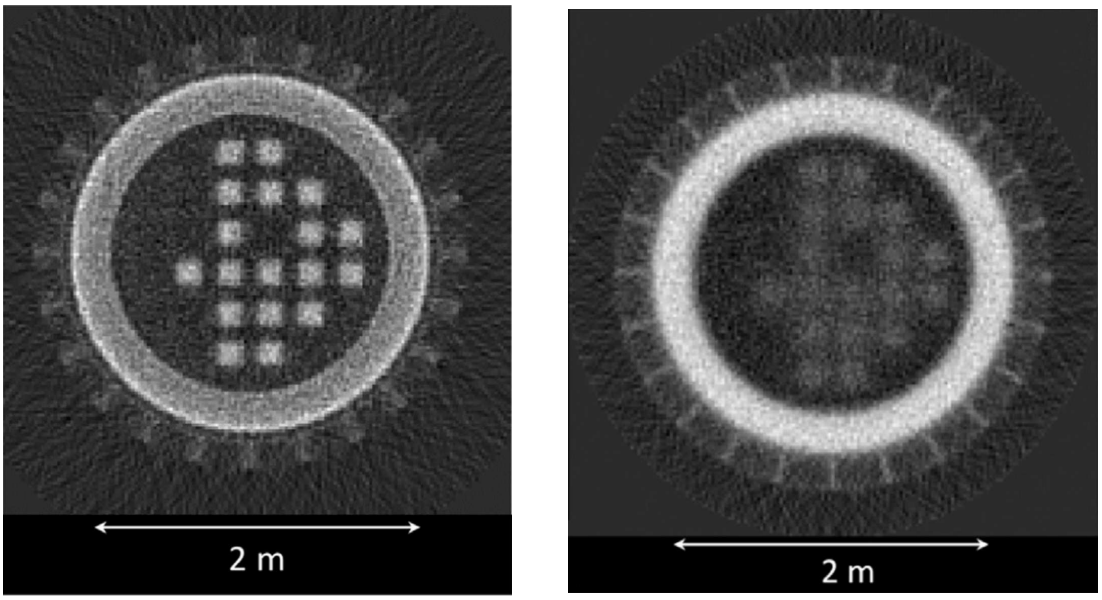

Figure 5.4: Two reconstructions created from the simulation data: areal density (left) and muon transmission (right).

RECLBL library [105] was used to perform the reconstructions.

5.3 Results & Discussion

Image reconstruction of the vertical projection of the simulated MC-10 cask immediately shows all of the features that should be expected, both for areal density and transmission. The loading profile of the MC-10 is immediately evident as well as the steel gamma shielding and the cooling fins. Figure 5.5 shows a numbered schematic of each slot in the fuel basket along with the summed signal at each location for the areal density reconstruction. The summed signal is defined as the sum of the scattering density values contained in a 20×20 cm^2 area centered at the nominal location of the fuel bundle. An immediate distinction is apparent between the summed signal of slots containing the fuel assemblies and those that have been left empty. The average summed value of slots that contained assemblies was calculated to be 25.8 ± 1.3 arb. units. Empty slots averaged a summed signal value of 2.5 ± 1.3 arb. units.

A quick check for the validity of the values of the reconstruction is provided by

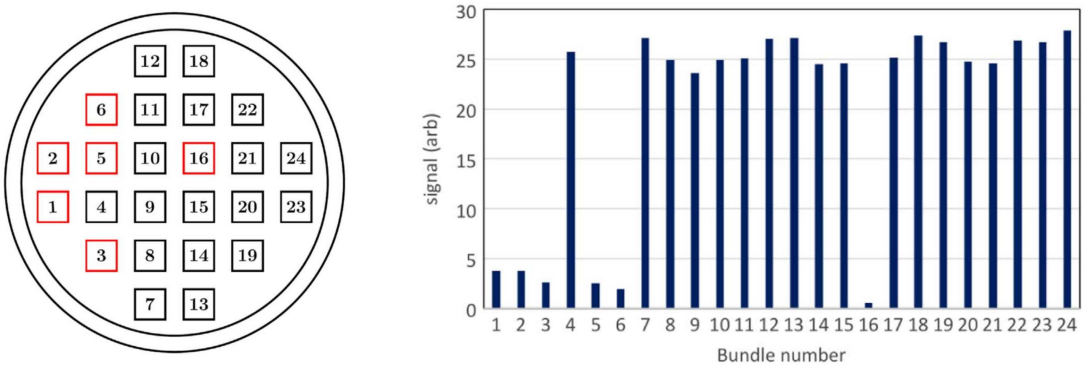

Figure 5.5: The numberbering scheme (left) of the fuel assemblies (red boxes indicate an empty slot) and the associated summed signal for each slot (right).

comparing the reconstructed relative scattering densities and the predicted relative scattering densities. The average summed signal for filled slots was 25.8, and the average signal for the gamma shield was 28.5. Taking the ratio of the fuel signal to the gamma signal produces a value of 0.905. The density of iron is 7.874 g cm^{-3} and the radiation length is 13.84 g cm^{-2}, giving a scattering density of 0.57 cm^{-1}. For uranium dioxide, the density is 10.97 g cm^{-3} and the radiation length is 6.65 g cm^{-2}, giving a scattering density of 1.65 cm^{-1}. However, in a fuel bundle, only 30% of the volume is accounted for by uranium dioxide; the residual volume is mostly air with some cladding and mechanical structure. The scattering density for a fuel bundle is then approximated as the scattering density of uranium dioxide multiplied by 0.3 to account for the contribution of the fuel to the fuel bundle, i.e. $1.65 * .3 = 0.495$. The ratio of the predicted scattering density of the fuel to that of the steel shell is then $0.495/0.57 = 0.87$. From this quick calculation, it is seen that the relative reconstruction values are close to those estimated from first principles giving confidence to the technique.

As described in Chapter 3, the stopping power of a material is proportional to the ratio Z/A of the material. The transmission reconstruction shows that the steel gamma shielding is more capable of stopping muons than the fuel bundles. This is expected since the ratio Z/A is roughly 0.466 for iron and is roughly 0.323 for uranium

dioxide. As indicated above, the ratio Z/A for a fuel bundle could be approximated as $0.323 * .3 = 0.097$ to account for the empty volume between fuel rods. As a result, it is expected that the steel shell would have a stopping power much greater than that of a fuel bundle. Here again, the reconstruction indicates results that are expected from first principles.

To first order, the scattering density signal is proportional to Z^2/A while the stopping power of the material is proportional to Z/A. Since the proton fraction generally decreases as Z increases, transmission radiography provides a weaker sensitivity to the UO_2 fuel. Scattering density, on the other hand, is more sensitive to the UO_2 fuel due to the extra dependence on Z. Muon scattering tomography thus provides a clearer image of the reconstructed fuel bundles than does muon transmission tomography.

5.4 MC-10 Model Method

A second simulation study was performed to examine how limited angle tomography could be accomplished with a smaller detector. The simulation was not modified except that the muon detectors were again reduced to two 1.2×1.2 m^2 planes. Several positions were selected for each plane in order to image different volumes of the cask. The positions were defined so that the upper detector plane ranged from $(0°, 180°]$ and the lower detector plane ranged from $(180°, 360°]$. The number of positions determined the distance between positions. Positions were defined by keeping the detector planes at a fixed radius from the center of the cask and rotating the plane such that each plane was always perpendicular to the edge of the cask. An integer n determined the number of positions, meaning that there were $n + 1$ divisions in the angular range of each detector and the detectors were placed with the center of the plane lying at the point of a division. The total number of positions increased as n^2, and data were simulated for n equal to 2, 3, and 4.

Scattering density histograms were produced by the same method described be-

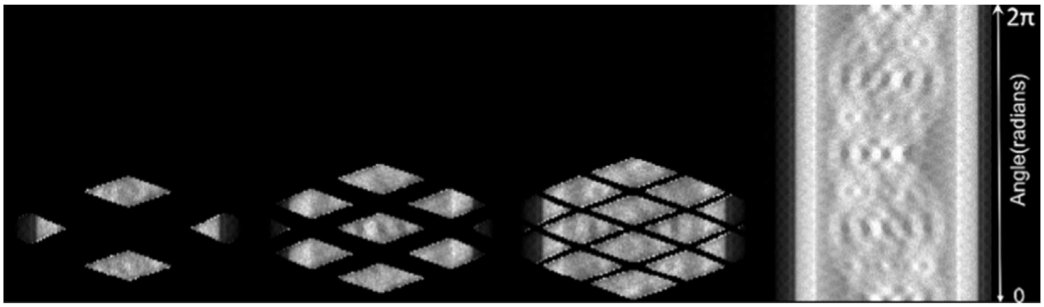

Figure 5.6: Sinograms for two, three, and four small detector positions, and for the cylindrical detector (left to right).

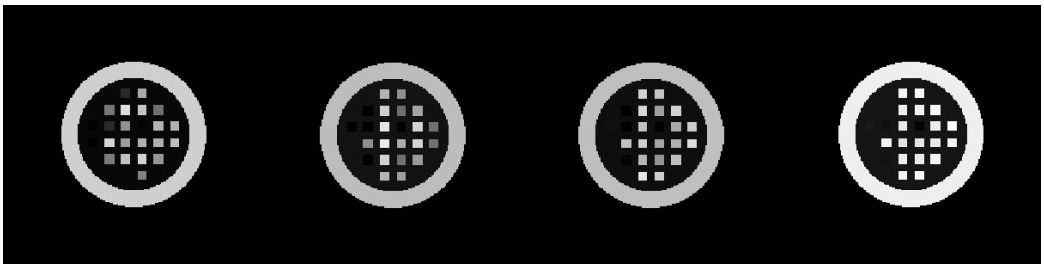

Figure 5.7: Scattering densities obtained from the partial sinograms ($n = 2, 3, 4$) and the full sinogram (left to right).

fore. The resulting sinograms for each n value as well as the full sinogram from the cylindrical detectors are shown in Figure 5.6. By increasing the number of detector positions, the sinogram can be filled in and even completed; though the counting time will also increase with the number of positions used. A simple model was constructed that contained 24 fuel elements with cross-sectional areas matching that of the fuel bundles and one shielding element with inner and outer diameters that matched those of the gamma shielding. A total of 25 elements were used in the model; 24 for the fuel bundle and 1 for the gamma shielding. It was assumed that the integrated scattering density signal (areal density) contained in the sinogram was the result of scattering densities of the model elements. Fits for the model for each sinogram were performed using the dry cask modeling method described in Chapter 3. Results for these fits are shown in Figure 5.7.

5.5 Conclusion

An areal density signal and the transmission signal can be obtained by measuring cosmic ray muons incident and exiting tracks. Correlating the muon tracks to angular increments and distance offsets from the center of the object being imaged allow for the creation of sinograms. With complete angular coverage, traditional reconstruction methods, such as filtered back projection, can be used to show a vertically projected image of the object. This was done in simulation on a partially loaded MC-10 cask using 10^8 muon tracks or 1.9 days counting time for a perfectly efficient detector. Reconstruction via filtered back projection estimated that the average summed value over the area of a fuel bundle was 25.8 ± 1.3 arb. units for present fuel bundles and 2.5 ± 1.3 arb. units for missing bundles. The statistical difference between a full fuel bundle and a missing fuel bundle is distinguished at 18 σ.

If ring detectors are not feasible, smaller detectors can be used to fill or partially fill the sinogram. However, this requires longer counting times in multiple positions. Should design information about the cask be known, the loading profile of the cask can be ascertained with a partial sinogram constructed from limited views.

Chapter 6

Fuel Cask Monitoring

The methods developed in Chapter 5 can be applied beyond the identification of missing fuel bundles. After the fuel has been spent in a nuclear reactor, the chemical composition of the fuel has changed and continues to change due to the fissioning of unstable nuclei. The fission process conserves the charge of the initial nucleus but divides it between the two fission product nuclei. Electron density (Z/A) of the material is constant (to first order) as the fuel fissions, while the average charge of nuclei (Z) decreases. Using fuel burnup descriptions described in [106], several simulations were run to study the muon signatures of fresh and spent fuel. Additional simulations were also performed to investigate the sensitivity of muon signals to different diversion scenarios. The work presented here was published by the Los Alamos National Laboratory's Threat Reduction Team in [107].

6.1 Spent Fuel Burnup

In commercial reactors, the amount of heavy metal that is lost to fission is characterized by the burnup fraction. Burnup is given either in units of the percent of burned up uranium or in the more easily measured gigawatt days per ton (GWd/T) of energy extracted from the fuel. Work presented in [106] provides a detailed inventory of the nuclear products of spent fuel as a function of burnup, generated using the code Monteburns–which links the Monte Carlo transport code MCNP to isotope generation and depletion tools such as CINDER or ORIGEN to provide both time- and

energy-dependent system parameters. A 1/8th core model representing a Pressurized Water Reactor through different irradiation cycles provided isotopic compositions on a per pin basis for the simulated fuel assemblies.

The isotopic compositions for a variety of burnups, enrichments, and cooling times were used to create Geant4 simulations with the fuel bundles held by a TN-24P spent fuel cask, in order to study: the signatures of fresh and spent fuel, the impact of β-decay on muon scattering of spent fuel, and the change in signature from some materials that could be used to replace diverted fuel bundles. The ^{239}Pu content for a spent fuel bundle was calculated for burnups of 15, 30, 45, and 60 GWd/T and is shown in Figure 6.1. In order to divert a significant quantity (SQ) of plutonium, as defined by the International Atomic Energy Agency (IAEA) [108], four bundles are required.

The isotope distributions for fresh fuel and fuel with a burnup of 60 GWd/T of heavy metal are shown in Figure 6.2. A double-humped distribution of the fission products is apparent with 14-day and 80-year cooled fuel isotope distributions having only small differences due to β-decay. The burnup fraction at this exposure is 5.5%, and is easily calculated from the isotopic composition of the simulated fuel bundle. In the simplest model, where the atomic number of the fission products is half of the starting nuclei, the value of $1/X_0$ for the fission products can be estimated using equation 3.15 as 10.29 g cm^{-2}. The radiation length of a compound ($X_0^{(C)}$) can be estimated from

$$\frac{w_t}{X_0^{(C)}} = \sum_j \frac{w_j}{X_0^{(j)}}, \tag{6.1}$$

with $w_t = \sum_j w_j$, w_j being the weight percentage contribution of element j to the compound, and $X_0^{(j)}$ being the radiation length of element j. For uranium dioxide, Equation 6.1 gives an estimate of 6.65 g cm^{-2} for the radiation length. If 5.5% of the

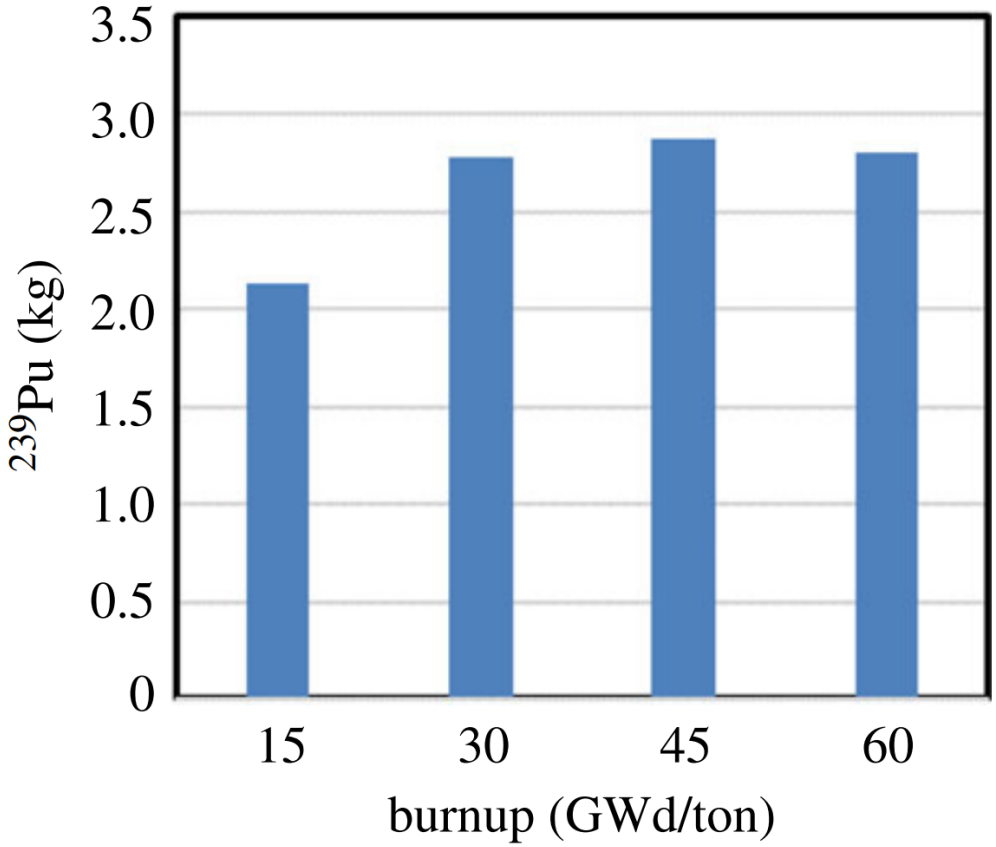

Figure 6.1: The ^{239}Pu content of a fuel bundle as a function of burnup.

uranium is converted to fission products of half nuclei, then the predicted radiation length is

$$X_0^{(\mathrm{UO_2+products})} = \left[\frac{1}{w_t}\left(\frac{w_\mathrm{U}}{X_0^{(\mathrm{U})}} * (0.945) + \frac{w_\mathrm{O}}{X_0^{(\mathrm{O})}} + \frac{w_\mathrm{U}}{X_0^{(\mathrm{products})}} * (0.055)\right)\right]^{-1}$$
$$= 6.80 \text{ g cm}^{-2},$$

where w_U and w_O is the weight fraction of uranium and oxygen in fresh fuel. The predicted change in radiation length is then roughly a 2.2% increase, which to first order should reduce the standard deviation of the muon scattering distribution by 2.2%. The transmission should remain the same when the burned fuel is compared to fresh fuel due to the constancy of Z/A in the fuel.

6.2 Simulation

6.2.1 TN-24P Spent Fuel Cask

For these simulations, a TN-24P fuel cask was modeled rather than the MC-10 because the TN-24 spent fuel cask is used commercially while the MC-10 was a prototype. Also, Idaho National Laboratory has a TN-24P spent fuel cask at its facilities allowing simulations to predict the muon signals expected if any muon measurements are carried out at INL in the future. The TN-24P geometric description can be found in [109]. Overall, the design is similar to that of the MC-10 with the main components being a steel gamma shield, outer neutron shielding, cooling fins, and an inner basket to hold fuel bundles.

The outer dimensions of the TN-24P are a height of 5.063 m and a diameter of 2.281 m. The outer surface of the cask is a stainless steel skin with a thickness of 10 mm. Inside the steel, skin sits the neutron shielding that is 133 mm thick. The neutron shielding is separated by 60 equi-spaced copper cooling fins. Each copper

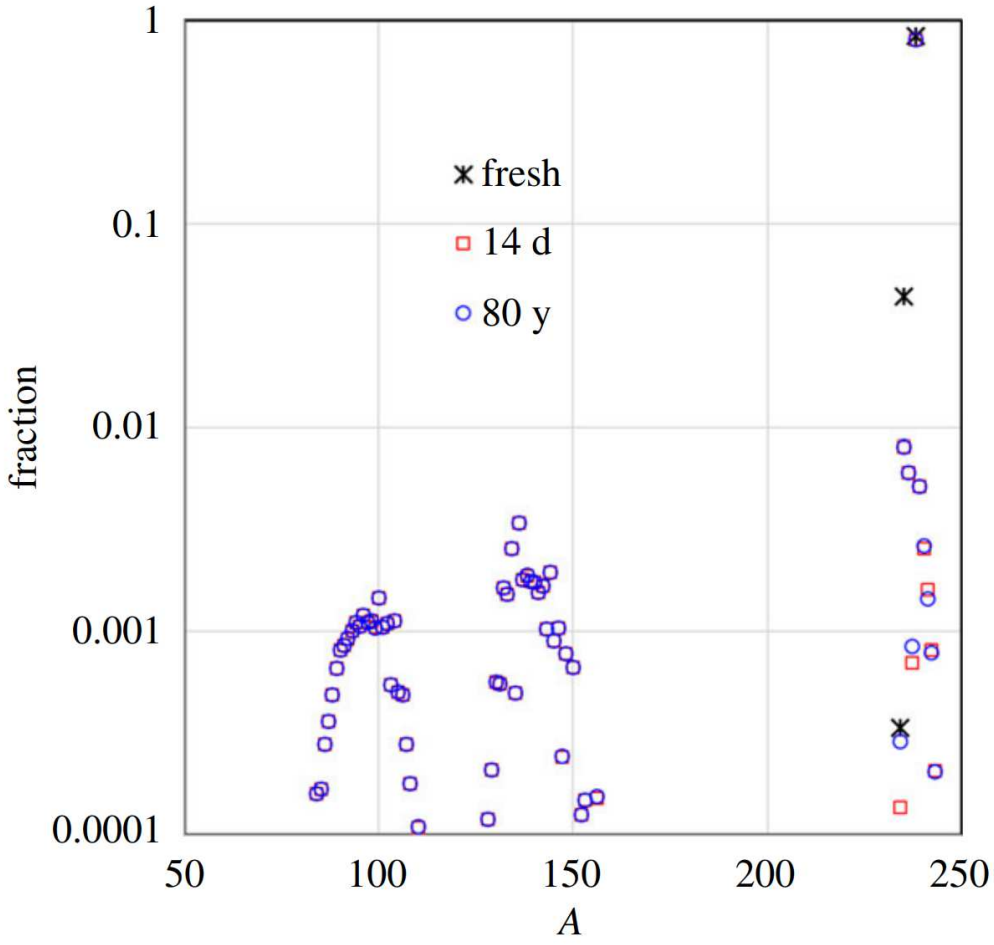

Figure 6.2: Effect of burnup on the isotopic composition of fuel. The small change in the isotopic distribution as a function of time of storage can be seen in the difference between the 14 day (red square) and 80 year (blue circle) curves.

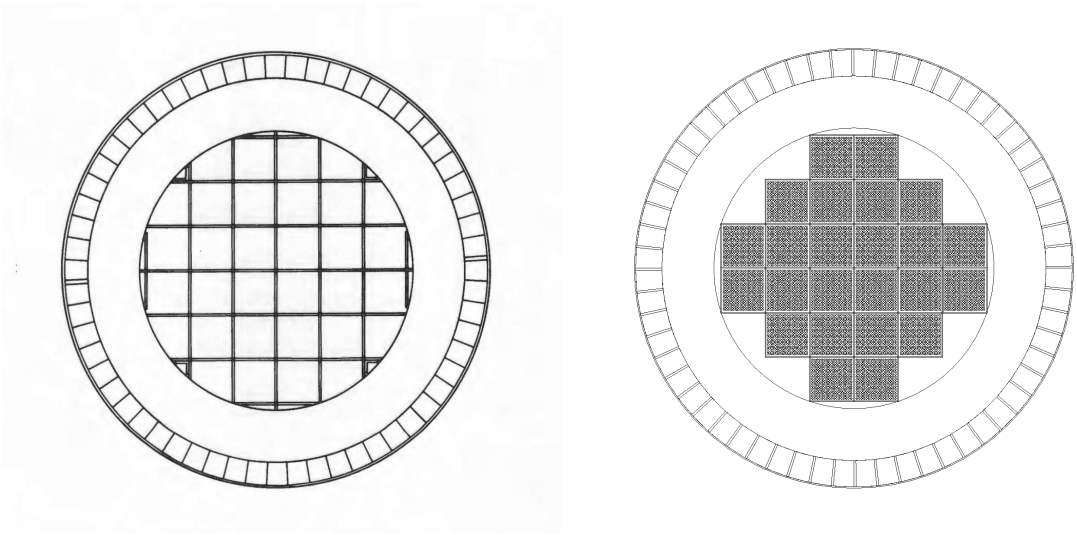

Figure 6.3: TN-24P cross-section from [109] (left) and from simulation (right).

fin has a width of 11.4 mm and is welded to the inner gamma shield and attached to the steel skin. A 270 mm thick steel shell acts as gamma shielding with an inner diameter of 1.455 m. The interior aluminum basket is made from interlocking 10 mm thick plates creating a grid that can hold up to 24 fuel bundles. Figure 6.3 shows comparative cross-sections for the TN-24P drawing and that of the simulated cask using Geant4. The simulated chemical composition of all components is given in Table 6.1.

Component	Material	Composition [weight%]
Steel Shell Steel Skin	Steel Alloy	97.86-Fe, 1-Mg, 0.15-C, 0.9-S, 0.05-Si, 0.04-P
Neutron Shield	Borated Polyethylene	77.74-C, 13.03-H, 5.00-B, 4.23-O
Aluminum Basket	Aluminum	100-Al
Cladding	Zircaloy-4	97.85-Zr,1.7-Sn, 0.19-Cr, 0.18-Fe, 0.08-Ni
Cooling Fins	Copper	100-Cu

Table 6.1: Chemical composition for each component of the simulated TN-24P.

The simulated muon detectors that surrounded the cask were identical in size and position to the two cylindrical detectors described in Chapter 5 and the method for

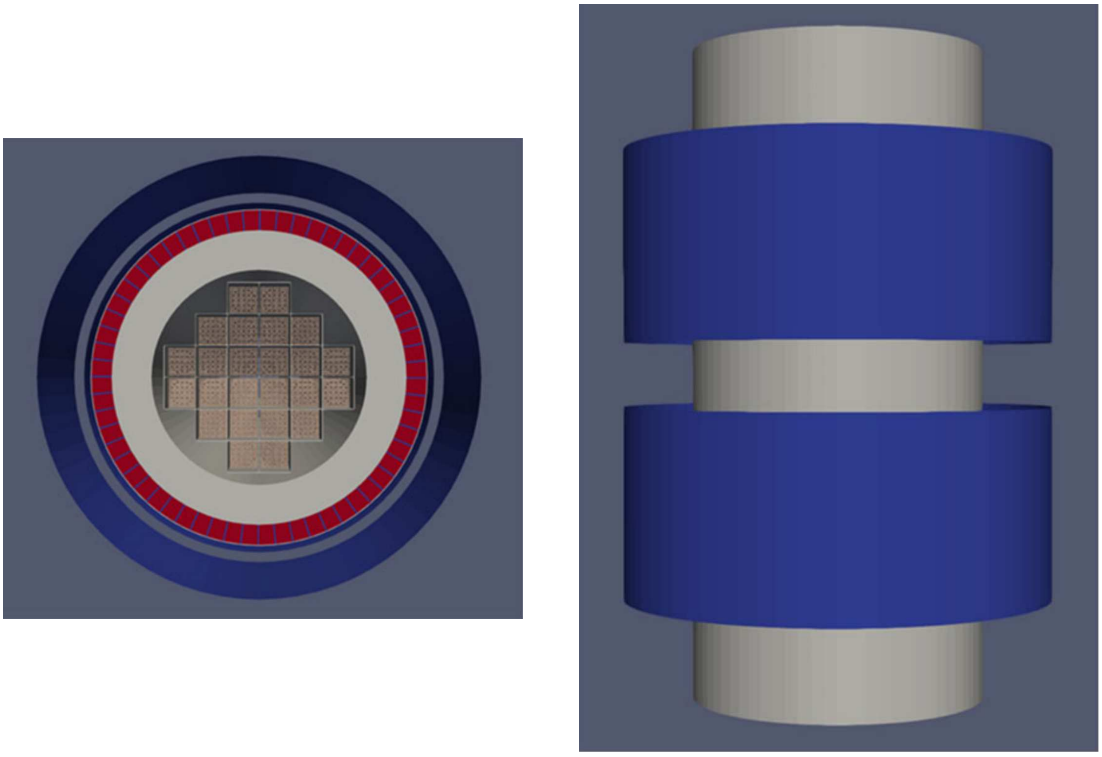

Figure 6.4: Top-down view (left) and side view (right) of the TN-24P simulated fuel cask and cylindrical muon detectors.

generating muons was the same. Figure 6.4 gives a schematic view of the simulated TN-24P cask as well as the cylindrical muon detectors. However, the number of generated muons was increased from 1×10^8 to 3.7×10^8 in order to simulate $\sim$7 days of count time with a perfectly efficient detector.

6.2.2 Spent Nuclear Reactor Fuel

Simulated fuel bundles had variable chemical and isotopic compositions, depending on the output from the Monteburn software. The geometric design was identical for the Monteburns and Geant4 simulations, as shown in Figure 6.5. The fuel bundles were 17×17 pressurized water reactor fuel bundles, with 289 rod-locations with a horizontal separation distance of 1.254 cm between the centers of adjacent rods. Of the 289 rod locations, 25 were control-rods and 264 were fuel rods. Each fuel rod was given a radius of 4.1 mm and was surrounded with a cladding layer that had an inner

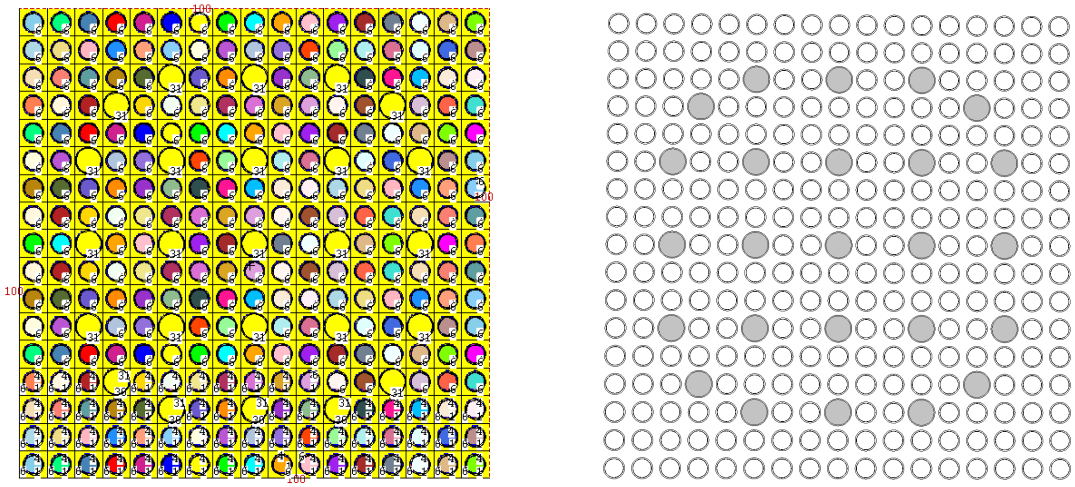

Figure 6.5: A 17×17 PWR cross-section from Monteburns simulation (on left) and from Geant4 simulation (right).

radius of 4.2 cm and a thickness of 0.55 mm. The guide rods had an inner radius 5.71 mm and a thickness of 0.42 mm. A unique identification number was given to each fuel rod in the Monteburns output which was used to identify the chemical and isotopic composition of the rod. The composition information was used as input for the Geant4 simulated fuel bundles, which were then duplicated in all fuel bundle slots in the TN-24P (with the exception of fuel diversion scenarios).

6.3 Analysis

6.3.1 Sinograms

Sinograms with 2° bins in ϕ and 2 cm bins in ρ were generated from the data from each simulation. Scattering and transmission histograms were created by the projection of the incident muon track onto a perpendicular tally plane that bisected the center of the cask. Examples of an areal density sinogram and the filtered back projection reconstruction are shown in Figure 6.6.

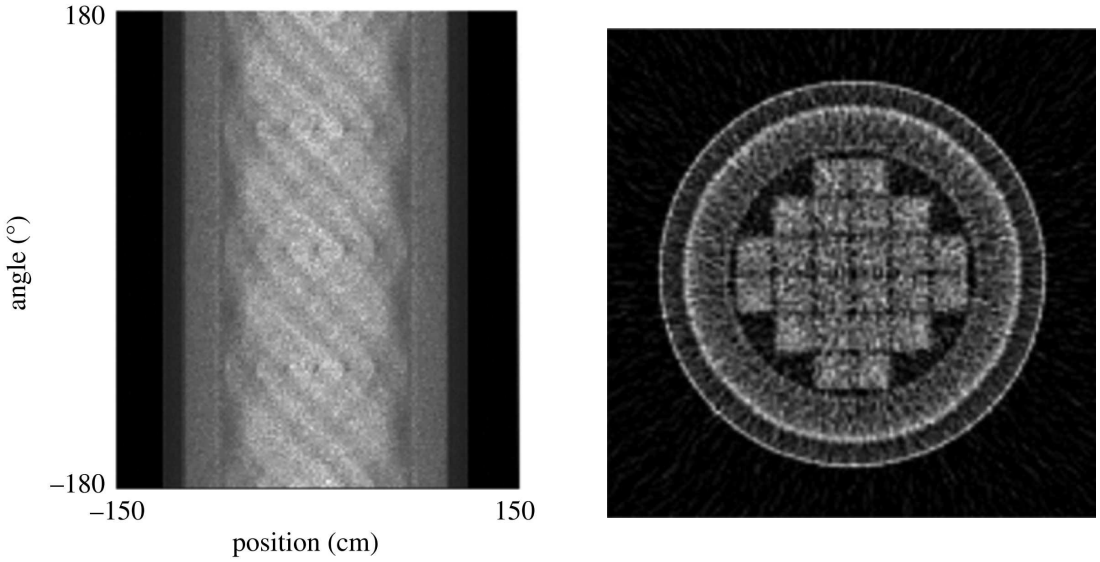

Figure 6.6: An areal density histogram from simulation .

6.3.2 Modification of the Multi-group Model

The multi-group model used in all previous analysis were based on the work done by the Los Alamos National Laboratory's Threat Reduction Team in [79]. In order to promote better fits to the scattering data, the multi-group model was modified to allow variability in the weights of each momentum group by taking into account momentum loss of the muon. The original multi-group model had a probability density function (given in equation 3.17) of

$$F(t,\theta) = \sum_i \frac{\alpha_i \theta}{\theta_i^2} \exp\left[-\frac{\theta^2}{2\theta_i^2}\right]$$

which can be rewritten as the differential scattering distribution

$$\frac{dN(t,\theta)}{d\theta} = N \sum_i \frac{\alpha_i \theta}{\theta_i^2} \exp\left[-\frac{\theta^2}{2\theta_i^2}\right], \tag{6.2}$$

where N is allowed to float to fit the binned data. To incorporate momentum loss of the muon, it is assumed that the muons will lose momentum linearly as a function of

radiation length, i.e.:

$$\Delta p = \frac{dp}{dt}t, \tag{6.3}$$

where $dp/dt < 0$ and is constant for all momenta. The modified multi-group model differential scattering distribution is then

$$\left.\begin{aligned}
\frac{dN(t,\theta)}{d\theta} &= N\sum_i \frac{\alpha_i(p_i,t)\theta}{\theta_i^2(p_i,t)}\exp\left[-\frac{\theta^2}{2\theta_i^2(p_i,t)}\right], & \\
\theta_i(p_i,t) &= \frac{13.6\text{ MeV/c}}{(p_i+\Delta p)\beta}\sqrt{t}, & \\
\alpha_i(p_i,t) &= 0, & \text{if } p_i+\Delta p<0,\\
&= \frac{p_i+\Delta p}{p_i}\alpha_i(p_i) & \text{if } p_{i-1}+\Delta p<0,\\
&= \alpha_i(p_i) & \text{otherwise,}
\end{aligned}\right\} \tag{6.4}$$

where $\alpha_i(p_i)$ is the weighting amplitude of momentum group p_i. The weighting amplitudes, $\alpha_i(p_i)$ were obtained by fitting high statistics data from a Geant4 simulation of just the empty steel gamma shielding using equation 3.17.

An example of the angular distributions for a one angle slice from a scattering sinogram is shown in Figure 6.7. On the left is the data from the simulation and on the right is the fit. A line plot taken at one position, shown by the red line, through the data and the fit is shown in Figure 6.8. The shape of the angular distribution is well fitted by the model.

6.4 Results & Discussion

6.4.1 Using only the Sinogram

Simulations were performed for an empty TN-24P and one loaded with the configurations described in Table 6.2, which were split into two categories: cooling fuel and

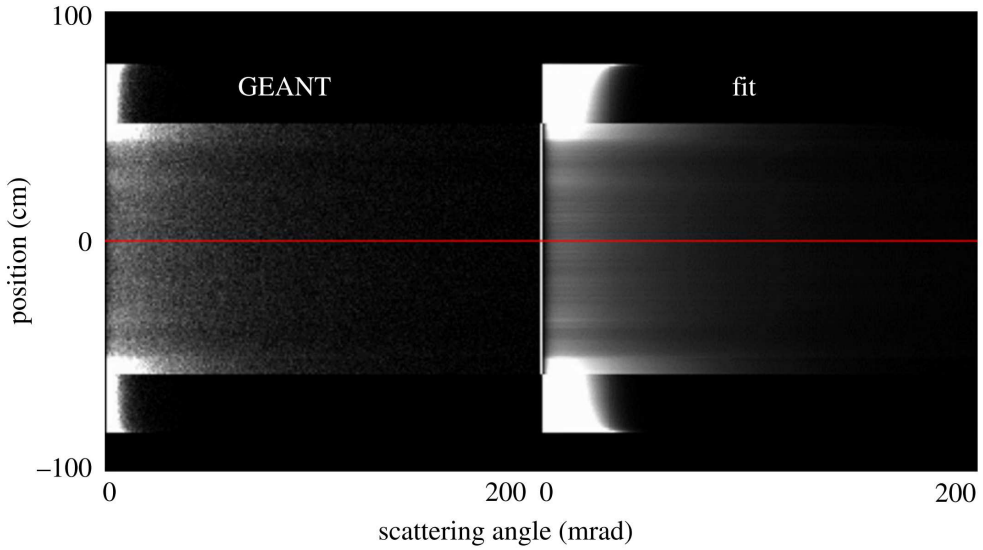

Figure 6.7: Scattering angle distribution (θ) for a single slice from scattering sinogram data (left) with the fit from the modified multi-group model (right).

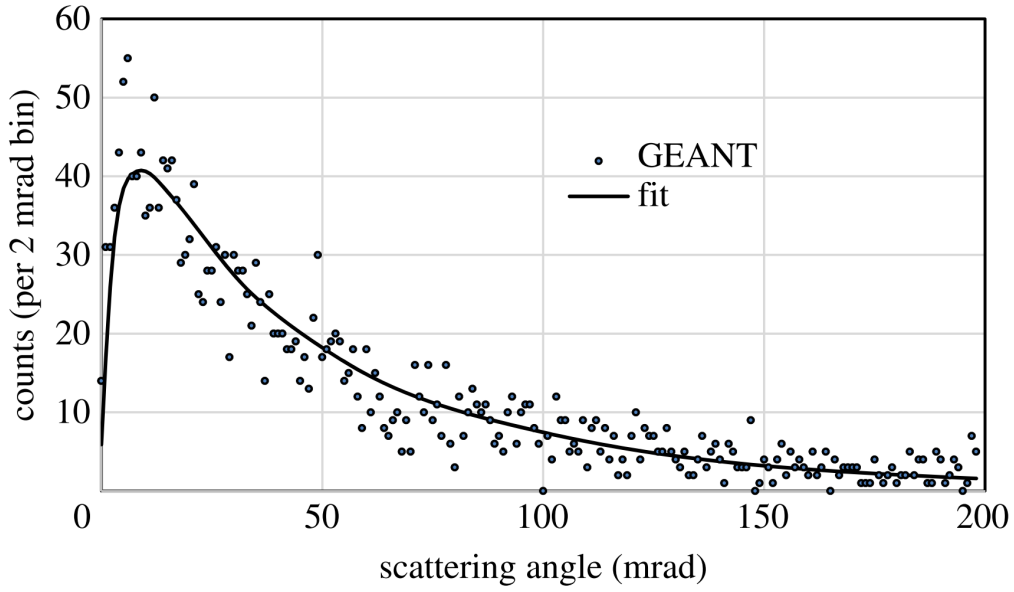

Figure 6.8: A plot from the red line in Figure 6.7 showing the simulated Geant4 scattering distribution and the corresponding fit from the modified multi-group fit.

diverted fuel. In the case of diverted fuel, the diverted fuel assembly had the same geometry as a spent fuel bundle; however, the uranium dioxide fuel was substituted for a different material. The fuel examined was about 5.5% burnup and was simulated as an equivalent to 60 GWd/T burnup. A first simple analysis used the sinograms for the loaded and empty cask, then subtract the empty cask sinogram from the loaded cask sinogram. An example of this method is shown in Figure 6.9 where one fuel bundle was replaced with steel. The effect from the steel bundle is clearly observed in Figure 6.10, where the values in the subtracted sinogram are averaged over ϕ for each ρ column.

Cooling Fuel Age	**Diverted Fuel Bundle Replacement**
Fresh (Prior to reactor loading)	Fresh Fuel Bundle
14 days (After Cask Loading)	Steel Bundle
40 years	Lead (Pb) Bundle
80 years	Depleted Uranium (DU) Bundle
-	no replacement

Table 6.2: Two loading configuration categories. Cooling fuel is fresh fuel, and 60 GWd/T burnup fuel that has been cooling in the TN-24P for lengths of time. Diverted fuel is a single fuel bundle from the center of the cask being replaced with a decoy fuel bundle assembly.

The difference profile for a cask loading configuration can further be averaged along ρ where the profile is non-zero to get an average muon signal for the cask. Figure 6.11 plots the ratio of the averaged sinogram signal for a given loading profile to that of a cask fully loaded with 14-day cooled fuel. The error bars only reflect the statistical error.

The difference between the scattering signal for fresh and spent fuel is 2.5% with statistical uncertainties being close to 0.1%. As expected, there is no detectable difference in the stopping signal which has an uncertainty of approximately 0.4%. This suggests that in principle it is possible to fingerprint fuel casks by measuring the

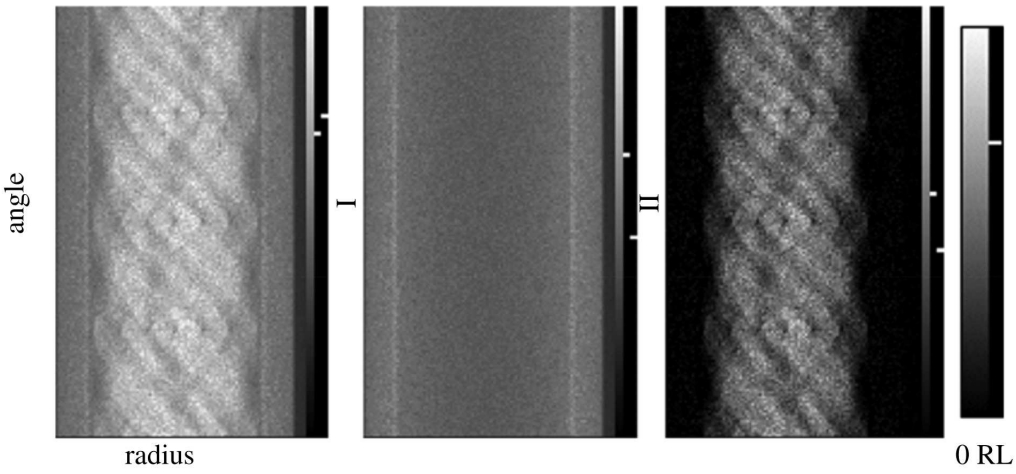

Figure 6.9: Sinograms for a loaded, empty, and the difference for the cask where one bundle has been replaced by steel.

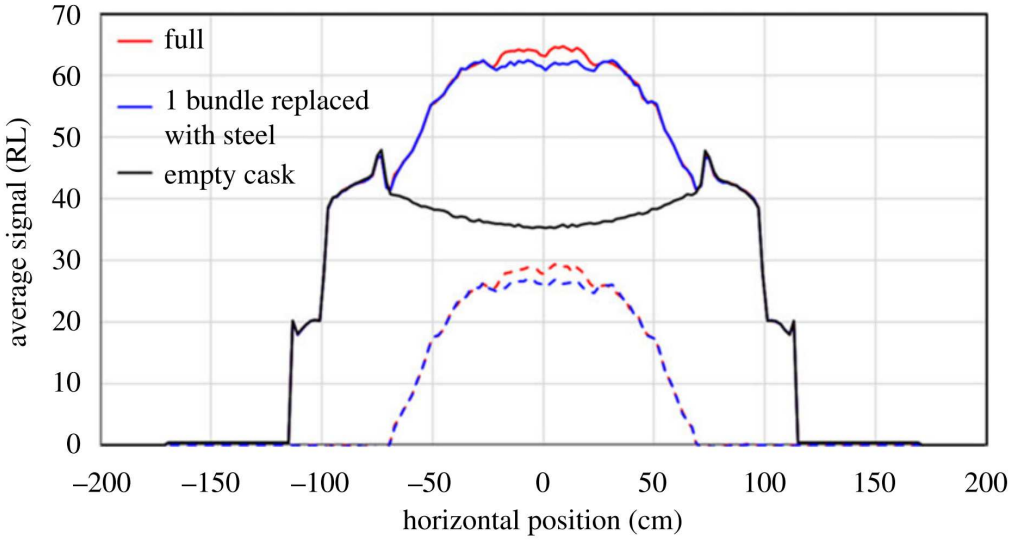

Figure 6.10: A profile along ρ for the averaged areal density sinogram.

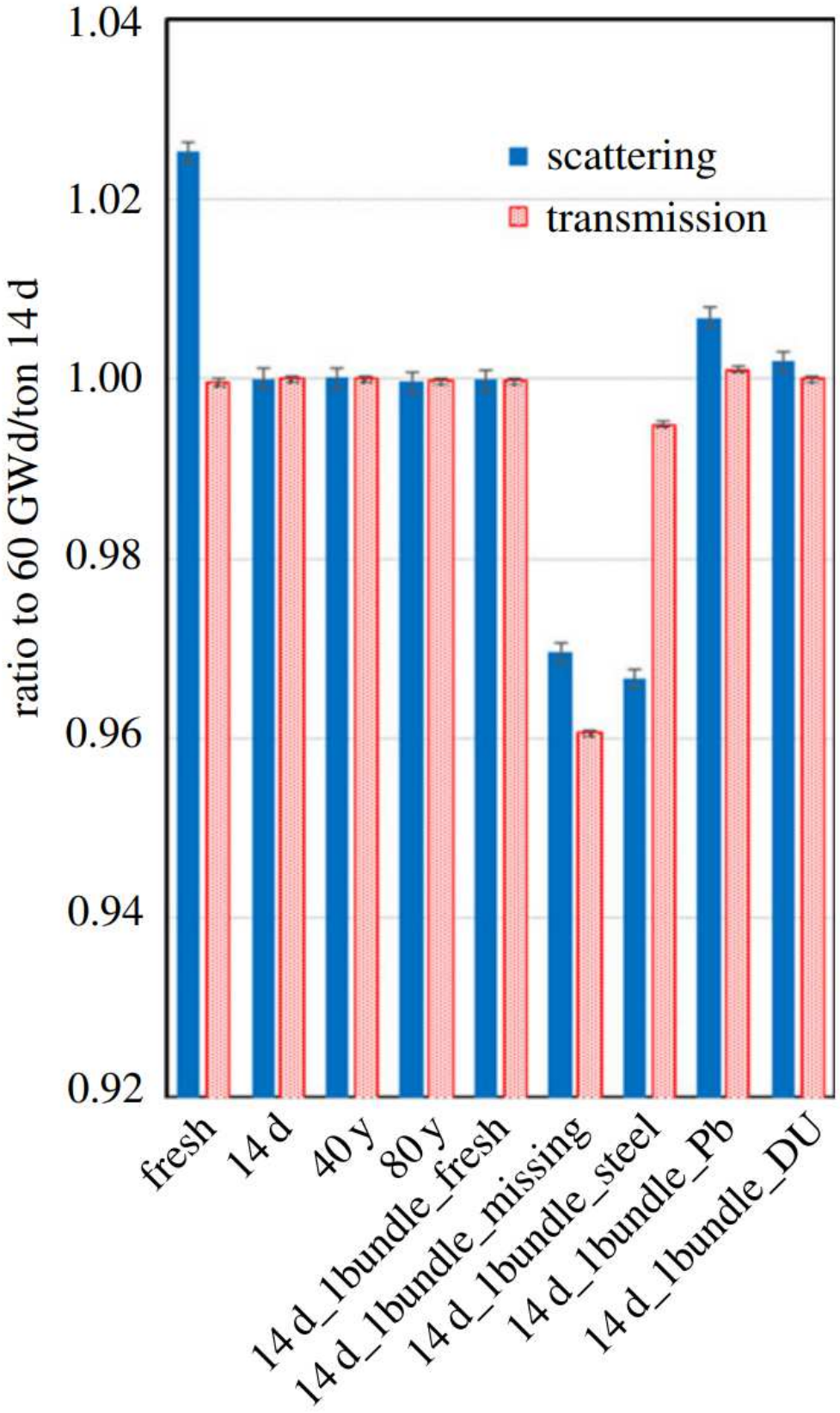

Figure 6.11: The ratio of the averaged sinogram signals between the loading profile (horizontal axis) and the a fully loaded cask (14 day fuel) for scattering (blue/solid) and transmission (red/shaded) signals.

burnup of the fuel in situ. Such measurements would most precisely be accomplished differentially in time, i.e. by comparing measurements across events when continuity of knowledge of the cask contents has been lost. Achieving 0.1% precision would require careful control for atmospheric pressure, detector efficiency and geometry, and all other experimental variables. Thus, experimental research is needed to establish the level of precision that can be obtained. Missing and replaced fuel bundles are readily apparent in the ratio of averaged signals, save for the cases of DU and fresh fuel. At 0.1% precision, the replacement of 4 fuel bundles (1 SQ) with DU or fresh fuel should be detectable at 4 σ.

6.5 TN-24P Cask Model

Increased sensitivity to diverted fuel bundles can be obtained by applying model fitting tomography, as discussed in Chapter 3. A simple model was constructed that has 26 density elements, one for each of the fuel bundle locations, one for the neutron shielding, and one for the gamma shielding. It is assumed that the model elements are sufficient to describe the areal density values recorded in the sinogram. The resulting scattering densities from the fits to the sinograms are shown in Figure 6.12. Deficiencies in the model are apparent in the consistent variation of the fuel bundle densities as a function of position. Nevertheless, the fuel bundle that is missing, replaced with lead, or replaced with steel is easily identified in the images.

The absolute value for the fractional changes of the densities for the missing fuel bundles obtained from the model analysis is plotted in Figure 6.13. Although a single fresh fuel bundle is difficult to detect, the missing, lead, and steel replacement fuel bundles are observed with a high likelihood in both the scattering and transmission imaging. It is clear that muon scattering gives a more significant signal for the lead and steel fuel bundles, whereas the muon transmission signal is more significant for the missing fuel bundle. Although either scattering or transmission could be spoofed

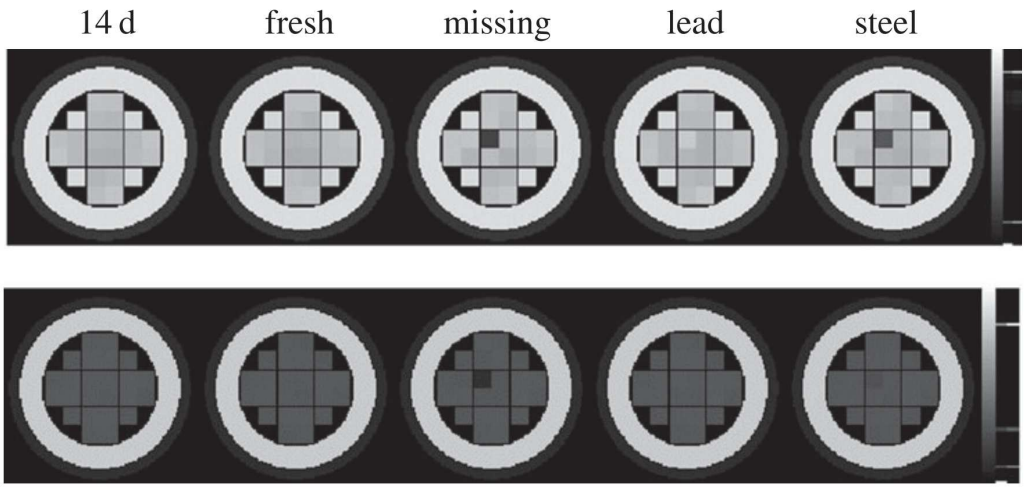

Figure 6.12: Tomographic volume densities obtained for scattering (top) and transmission (bottom) tomography for a fully loaded TN-24P spent fuel cask (left) and four cases where the bundle has been removed and either left empty or replaced.

by making dimensional changes to match the scattering or transmission of the fuel, it is difficult to match both simultaneously because of the unique mix of uranium and fission products specific to the loaded fuel. Numerical results for each diversion scenario are given in Table 6.3.

Loading Profile	Scatter Signal			Transmission Signal		
	signal	Δ signal	σ	signal	Δ signal	σ
fresh	0.03	0.01	1.67	0.03	0.03	1.06
missing	0.90	0.01	60.24	1.01	0.03	39.23
Pb	0.16	0.01	10.95	0.06	0.03	2.48
steel	0.73	0.01	48.49	0.14	0.03	5.41

Table 6.3: The signals and significance in standard deviations (σ) of the data plotted in Figure 6.13.

6.6 Conclusion

A numerical study of scattering and transmission cosmic-ray radiography/tomography with the goal of fingerprinting spent fuel casks was performed. There is a 2.5% difference between the scattering signals from fresh and spent fuel with 5.5% burnup

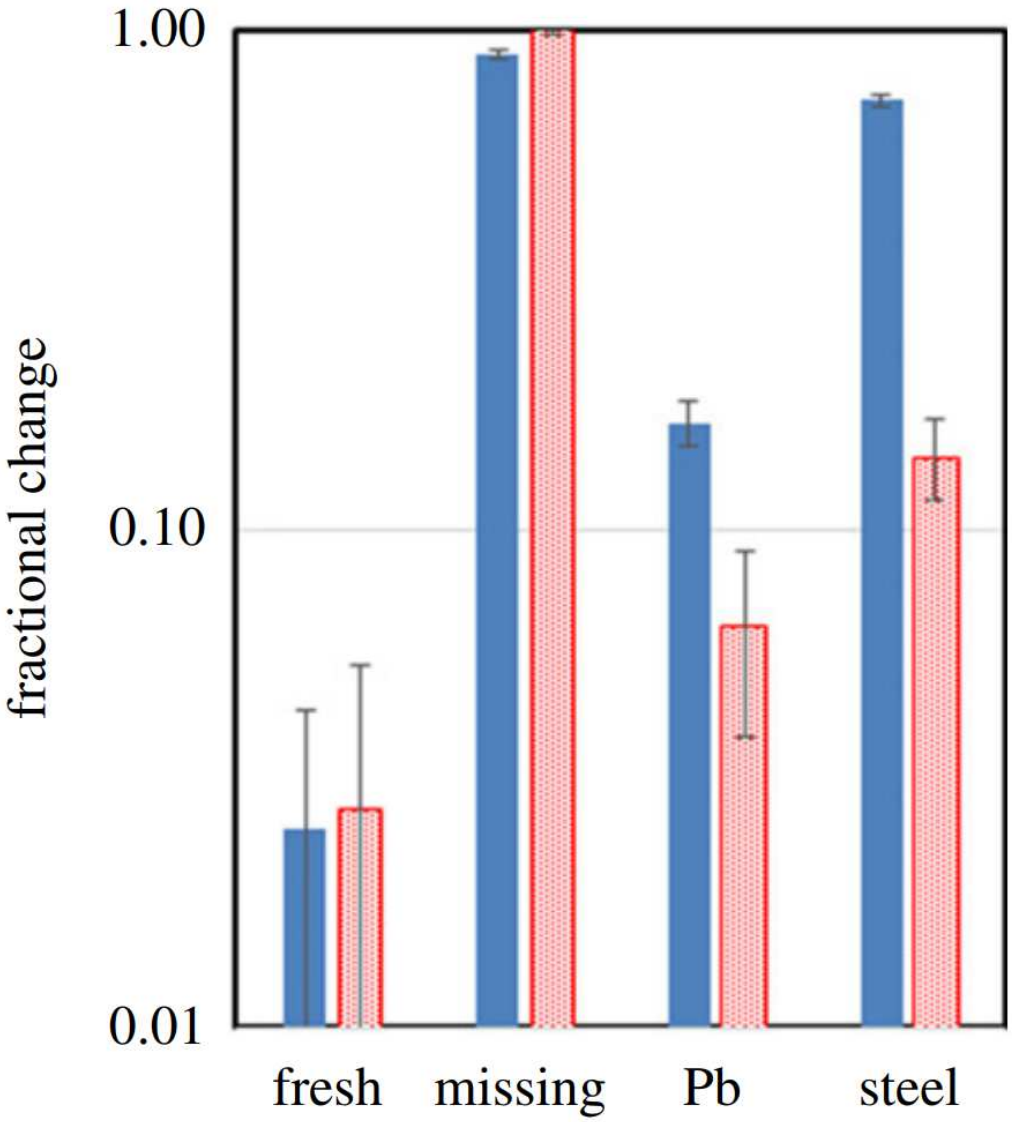

Figure 6.13: Absolute value of factional change of the density signal in the missing bundle slot between four diversion scenarios shown in Figure 6.12 and the fully loaded cask for scattering (blue/solid) and transmission (red/shaded) radiography.

(60 GWd/T). One week of muon exposure with two 1.5 m high detectors that surround the cask is sufficient to measure the scattering signal to 0.1% precision. This precision is sufficient to detect the diversion of a single bundle of fuel that has either been removed or replaced with a common material such as lead or iron. Although the signal from a single bundle replaced with fresh fuel or DU is too small to be reliably detected at this precision, the replacement of four bundles (enough to obtain 1 SQ of plutonium) would give a 4 σ signal.

Chapter 7

Final Fuel Verification for Geological Repositories

Finland and Sweden are currently preparing the first permanent geological repositories for high-level radioactive waste and are expected to begin accepting spent reactor fuel in the 2020's (Finland) and 2030's (Sweden) [110–112]. The operation of geological repositories will be the first time that spent nuclear fuel will be permanently disposed of, removing it from IAEA accountability and safeguards. Prior to the final burial of the spent nuclear fuel, the contents of the fuel casks will need to be verified to ensure that no material leaving safeguards is being diverted. Simulations of the casks designed for use at these geological repositories was carried out and the data analyzed to demonstrate the practicality of using cosmic-ray muons to perform a final verification of spent nuclear fuel.

7.1 Simulation

A description of the geometry of both pressurized water reactor (PWR) and boiling water reactor (BWR) fuel casks is given in [113]. Both cask designs consisted of an interior cast iron insert with square cross-section voids, to accommodate the fuel bundles, surrounded by a copper shell that would act as a corrosive barrier after burial. The cast iron insert had a diameter of 94.9 cm and was surrounded by 5 cm of copper, which made the outer dimensions of the cask 1.05 m in diameter and 4.835 m in height. The insert for PWR assemblies had four 26×26 cm^2 cross-section voids spaced in a 2×2 array with 37 cm separation from center to center. Inserts for BWR

assemblies had twelve 18×18 cm^2 cross-section voids spaced in an array with 21 cm separation from center to center. For these simulations, only the BWR cask was used due to the reduced fuel size and increased number of fuel bundles. It is reasonable to assume that the analysis applied to a BWR cask will also work on PWR casks, where the number of fuel bundle assemblies is reduced and their size is increased.

The simulated fuel assemblies were 10×10 BWR fuel bundles with a 16×16 cm^2 cross-section area. Each fuel bundle contained 92 UO_2 fuel rods and two water rods. The fuel rods had a radius of 4.775 mm and were surrounded by an outer cladding layer of 0.71 mm thick zirconium alloy. The water rods were composed of a single 0.71 mm thick zirconium alloy tube with an outer radius of 12.725 mm. The 10×10 array of fuel rods was encased in a square 10 mm thick aluminum shell. The fuel bundles did not vary along their 3.85 m length. All fuel bundles were placed inside of the fuel cask with identical orientation, since a 90° rotation of a fuel bundle would have virtually no effect on the muon scattering signal.

The BWR fuel cask simulations were broken in to five scenarios: a full cask, an empty cask, one fuel bundle removed, one half fuel bundle removed (half of the fuel rods removed from one side), and one fuel bundle replaced with lead (UO_2 replaced with Pb rods). Cross-sections of each simulated loading profile are shown in Figure 7.1. For each scenario, two horizontal detector planes were used to simulate muon detectors. The planes were aligned vertically with a separation of 1.5 m. The cask's central axis was placed horizontally and centered vertically and horizontally between the two detector planes. The plane's dimensions were: 4 meters along the length of the cask and 2 meters along the width of the cask. Each plane recorded the simulated muon's position and direction vectors. The muons' momentum and direction were selected randomly from the parameterized distribution described in [81]. Only muons aimed to pass through the cask or within 5 cm of its edge were simulated, in order to reduce the quantity of simulated data. Each data set consisted of 2.33×10^7 generated

muons. The data sets had an average number of 922 muons with zenith angles ranging between 0 and 45° that were also aimed to hit a 1 cm^2 area centered between the detectors. The calculated equivalent muon count time corresponded to 12 hours of data collection for a perfectly efficient detector.

7.2 Analysis and Discussion

7.2.1 Radiography Method

The angular resolution of the muon detectors was degraded to more realistically imitate a finite resolution detector. A muon's direction vector was described as a function of polar angles ϕ and θ (Figure 7.2) with the x, y, and z components being defined by:

$$\begin{bmatrix} x \\ y \\ z \end{bmatrix} = \begin{bmatrix} \sin(\theta)\cos(\varphi) \\ \sin(\theta)\sin(\varphi) \\ \cos(\theta) \end{bmatrix}. \tag{7.1}$$

Random Gaussian blurs, with a mean of 0 and a width of 0.009, were added to each polar angle of the incident and exiting muon tracks. The Gaussian blurs were selected so that the difference between the non-blurred muon scattering angle and the blurred muon scattering angle resulted in a Gaussian distribution with a width of 10 milliradians. The resulting blurred data was analogous to recording data at a limiting resolution of 10 milliradians.

The fuel casks had a uniform geometry along their central axes, within the range of the fuel bundles. The uniformity of the cask geometry was utilized by creating a horizontal tally plane at the center of the cask with a width of 1.2 m and a length of 3 m. The tally plane was divided into 2 cm pixels along its width with the pixels running the length of the plane. Each pixel had a corresponding scattering histogram,

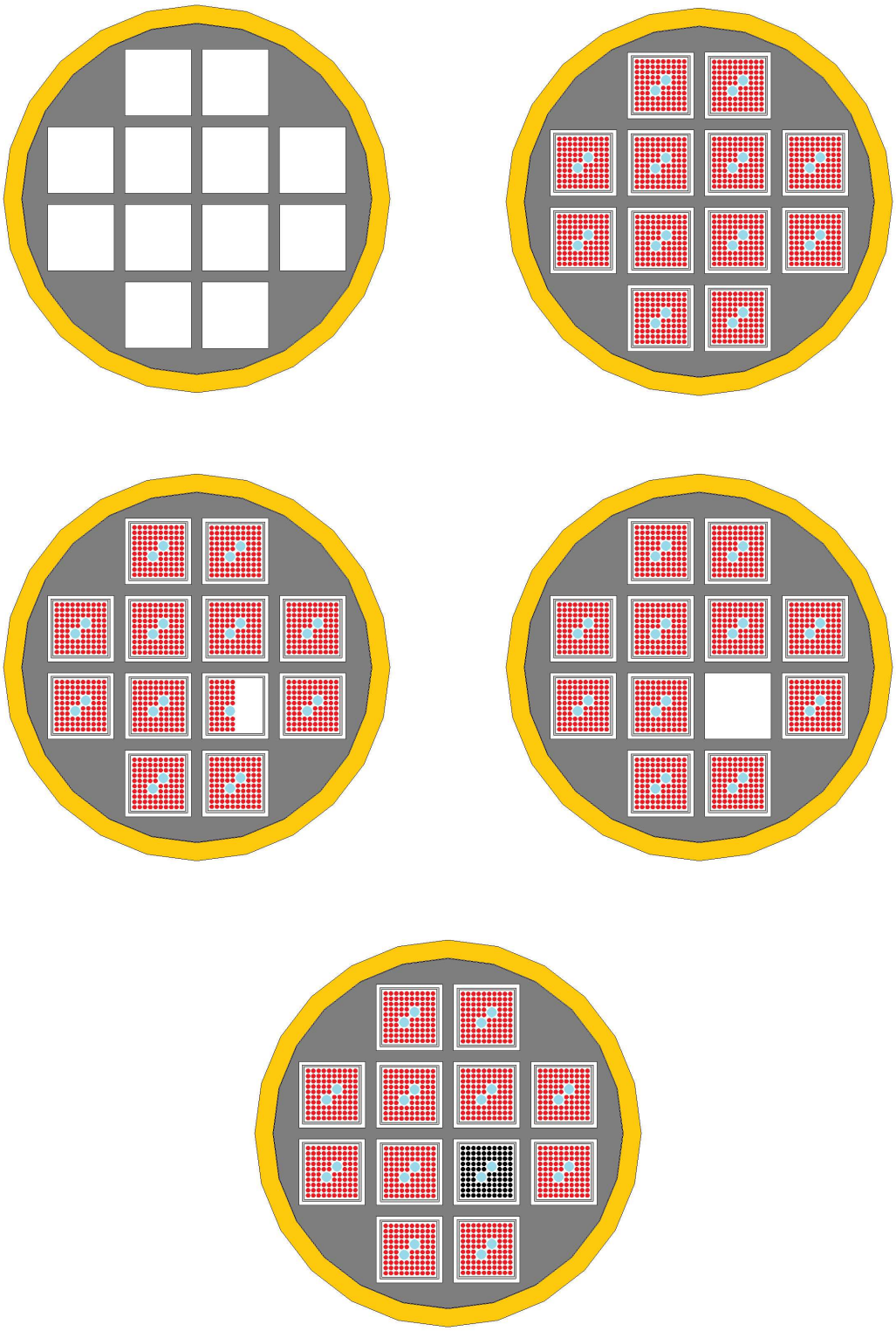

Figure 7.1: Five cross-sections of the BWR cask filled with 10×10 BWR fuel bundles. The simulated scenarios are: empty, full, one half bundle removed, one bundle removed, and one bundle's fuel content replaced with Pb rods. Red circles represent fuel rods, blue circles represent water rods, and black circles represent Pb rods.

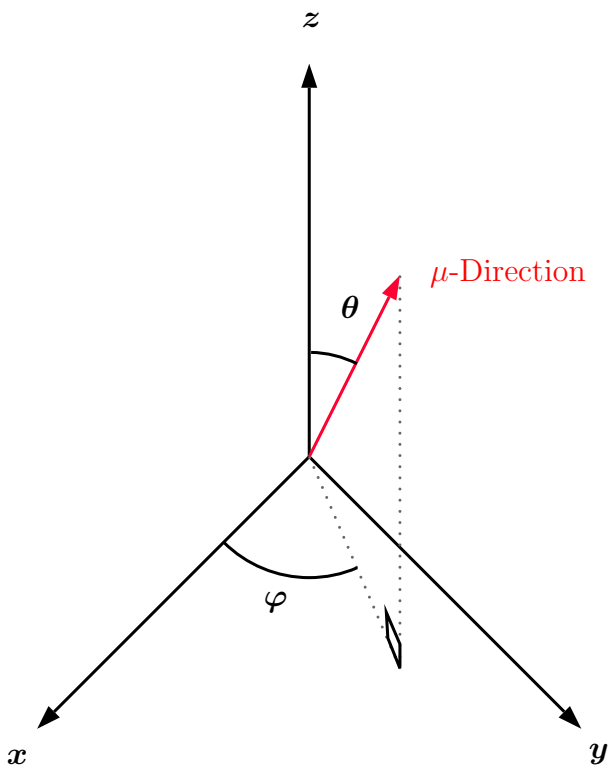

Figure 7.2: The polar angles used to describe the muon track direction vectors. Both polar angles had a random Gaussian blur added to them.

which was filled with the blurred scattering angles of the muons. The array of BWR fuel bundles was divided into four columns across the width of the cask, with the two outer columns having two fuel bundles and the two inner bundles having four fuel bundles. If the blurred incident muon track intersected the tally plane without crossing between fuel bundle columns, the corresponding scattering angle histogram of the intersected pixel was filled with the blurred muon scattering angle.

The average value of the muon scattering histogram ($\bar{\theta}_{\text{scat}}$) was calculated for each pixel, for each simulated scenario. The ratio of $\bar{\theta}_{\text{scat}}$ of each diversion scenario to that of a full fuel cask is plotted along the width of the cask in Figure 7.3 (for 12 hours counting time) and Figure 7.4 (for 24 hours counting time using 2, 12 hr data sets). The horizontal lines indicate the 2 cm width of each pixel and the vertical lines show the statistical error of the calculated ratio. The black line is plotted at the expected ratio value of 1. Below the ratio plot, the number of standard deviations difference from the expected value of 1 is plotted for each pixel.

The muon scattering ratio for an empty cask with a half-day of exposure quickly diverges from the expected value of 1, reaching up to 35.3 σ separation. For the diversion scenarios, the muon scattering ratio is nearly statistically identical to 1 in the first column and most of the second and fourth columns, where there is no diversion. Within a few cm on either side of the the third column, divergence from 1 starts. In the third column, where fuel has been diverted, the muon scattering ratio for the removal of a single fuel bundle reaches 7.7 σ away from that expected for a full cask, while the ratio for the removal of a half bundle reaches 5.2 σ. However, the muon scattering ratio for replacement of a fuel bundle stays close to the expected ratio for a full cask.

Applying the same analysis to data with a simulated exposure time of 24 hours increased the maximum divergence to nearly 50 σ for an empty cask. The divergence in the third column also increased to 11.2 σ for the removal of one fuel bundle and to

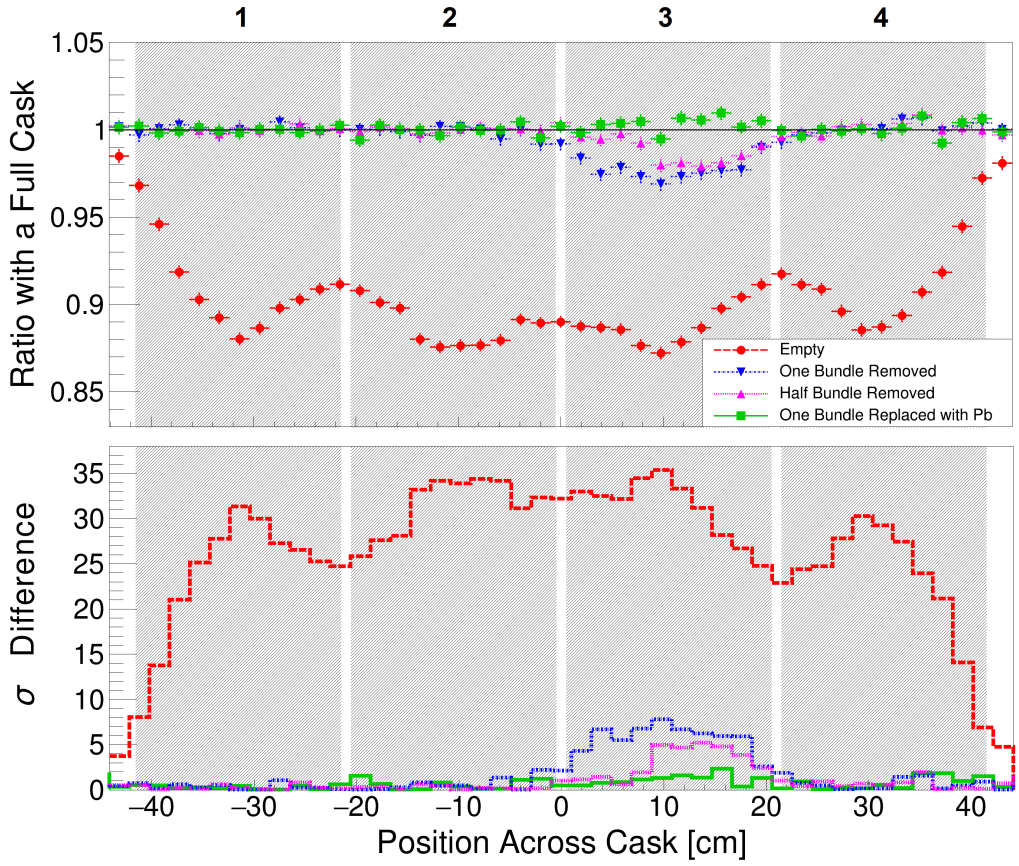

Figure 7.3: The ratio of $\bar{\theta}_{\text{scat}}$ for each diversion scenario to that of a full cask (above), for a 12 hr data set. The black line is the expected ratio. The difference in number of standard deviations (using statistical error only) that the calculated ratio is from the expected ratio of 1 (below). Shaded regions indicate the locations of fuel bundle columns (labeled 1-4, left to right).

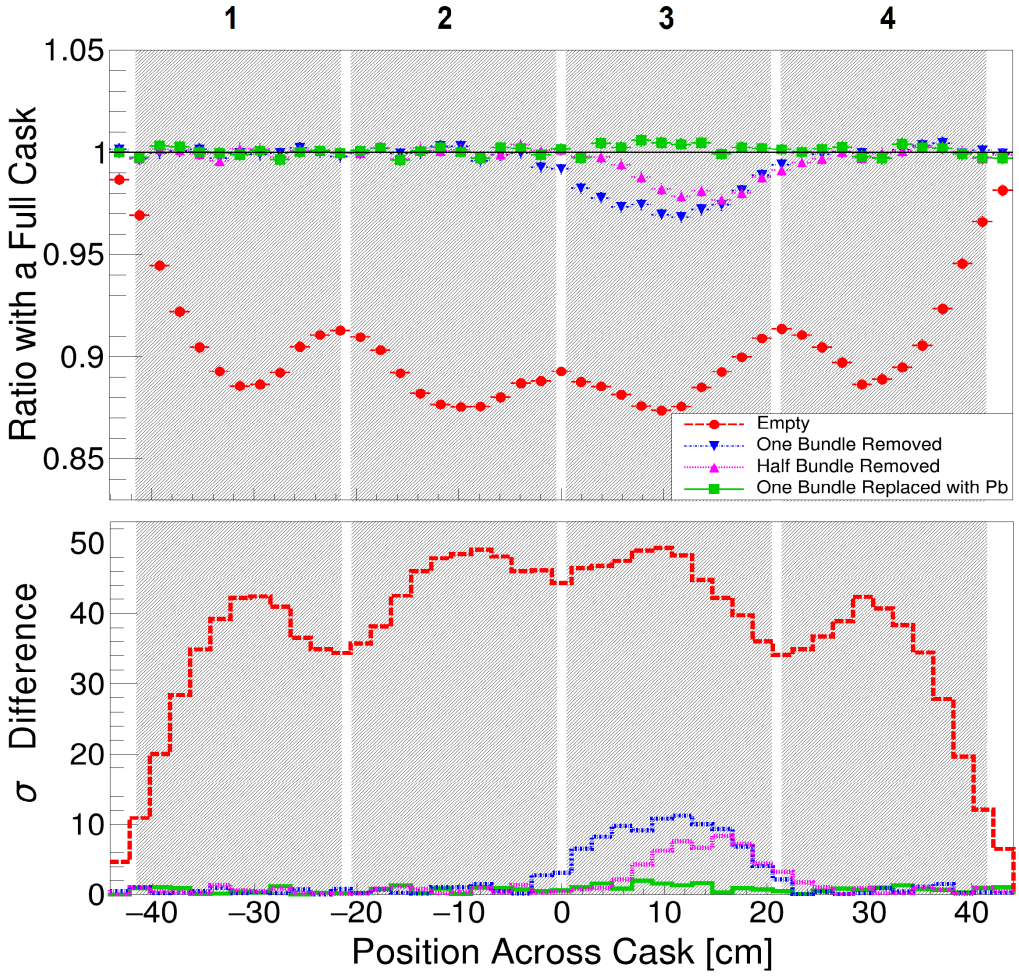

Figure 7.4: An identical plot to that of Figure 7.3, but with 24 hours of simulated data.

8.3 σ for the removal of one half bundle. However, the sensitivity to lead continued to remain below 2 σ.

In order to better quantify the ratio signal for each column, the average ratio within the boundaries of the fuel bundle columns was calculated and is plotted in Figure 7.5 for 12 hours and Figure 7.6 for 24 hours. Horizontal error bars were plotted to show the range of the fuel bundle columns. The statistical error bars are eclipsed by the markers; however, the lower plots show the discrepancy between the averaged scattering ratio and the predicted value of 1, in number of standard deviations. The averaged scattering ratio signal demonstrated that 12 hours of data is sufficient to identify: one half bundle removed at 10.0 σ, one bundle removed at 16.7 σ, and one fuel bundle replaced with Pb rods at 2.6 σ. The sensitivities increased with an additional 12 hours of data to: one half bundle removed at 16.5 σ, one bundle removed at 25.1 σ, and one fuel bundle replaced with Pb rods at 3.0 σ. Simple muon radiography techniques were sufficient to identify the simulated scenarios with significant statistical certainty.

7.2.2 Model Fitting Method

A simple model of the cask was created with 12 fuel bundle elements, an insert element, and a copper shell element; the simple model geometry is shown in Figure 7.7. Additional data consisting of 2.33×10^7 simulated muons was simulated, and blurred, for each scenario after rotating the cask 90° about its central axis. This data was combined with a simulated 12 hr data set in the non-rotated configuration to create a 24 hr data set. Muon scattering sinograms were created with the multi-group model fitter using the 24 hr non-rotated data sets and the 24 hr rotated data sets. The sinograms had a range of $[-60, 60]$ in ρ with 2 cm binning and a range of $[-180, 180)$ in φ with 1° binning. Figure 7.8 shows the resulting sinogram for a full, rotated cask. The data centered at $\varphi = -90°$ is from the non-rotated configuration

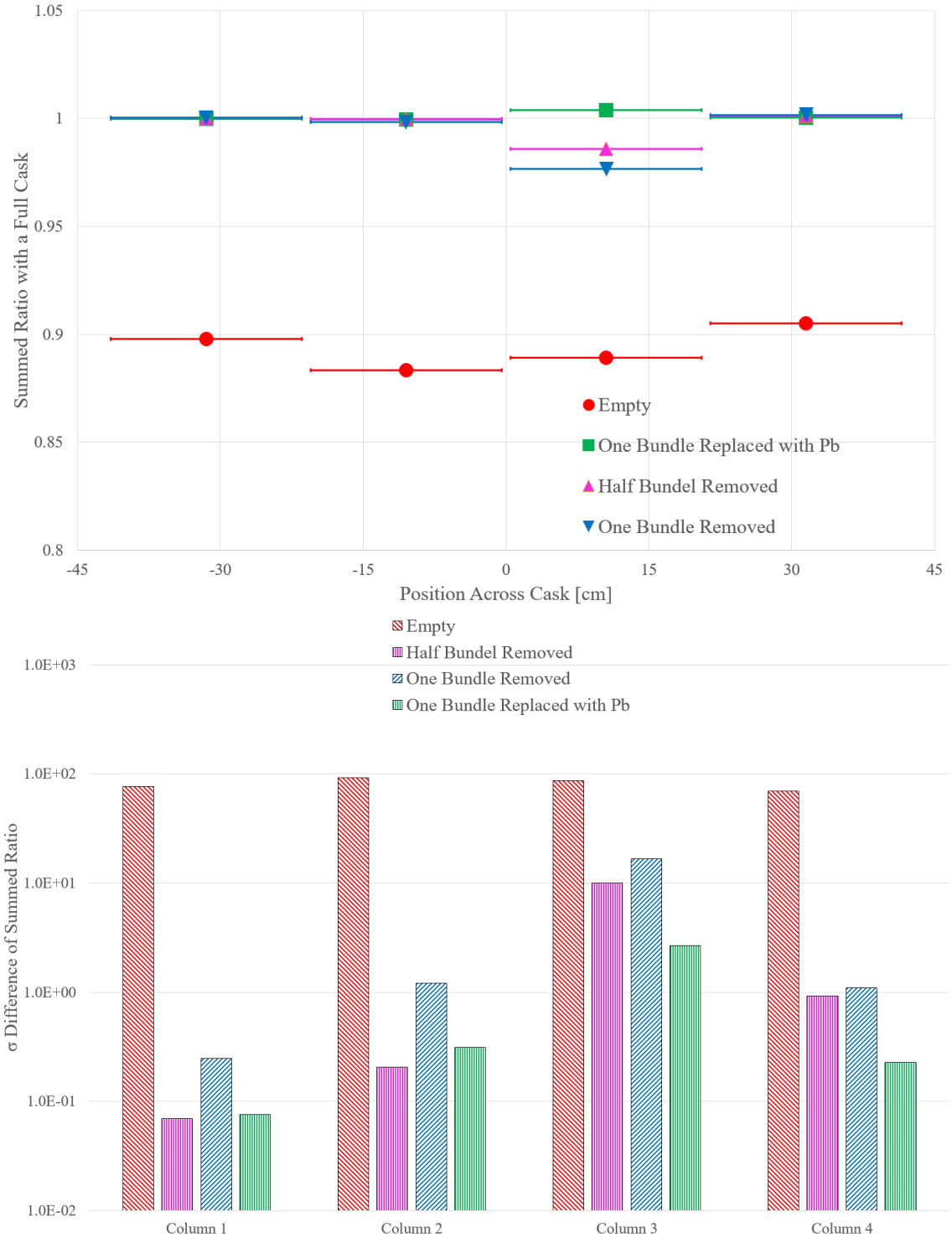

Figure 7.5: The scattering ratio, averaged across the range of each fuel bundle column (above), for a 12 hr data set. The difference in number of standard deviations of the averaged scattering ratio from 1 (lower).

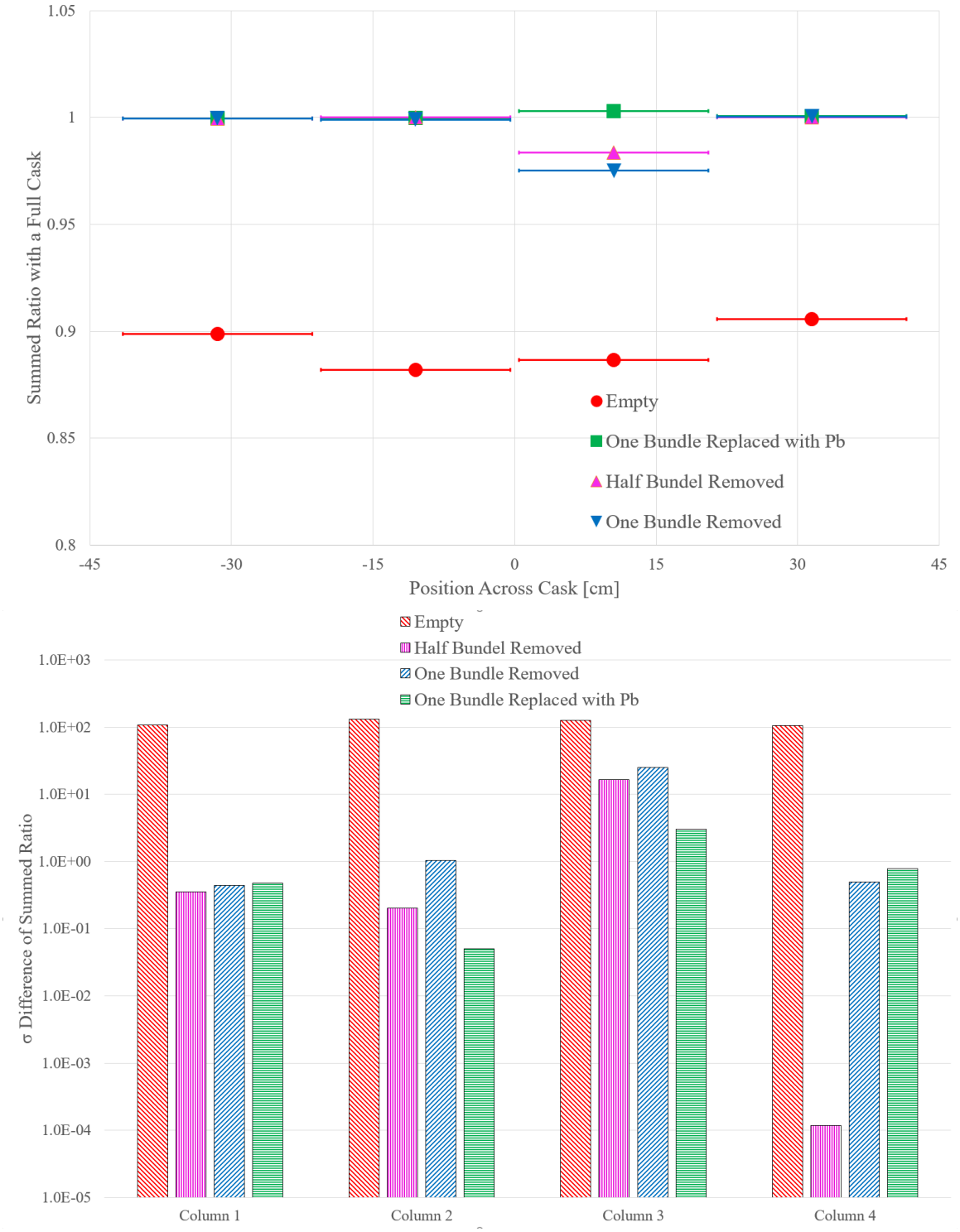

Figure 7.6: An identical plot to that of Figure 7.5, but with 24 hours of simulated data.

and the data centered at $\varphi = 0°$ is from the rotated configuration. There is some slight overlap between the two data sets, creating a region of higher statistic histograms.

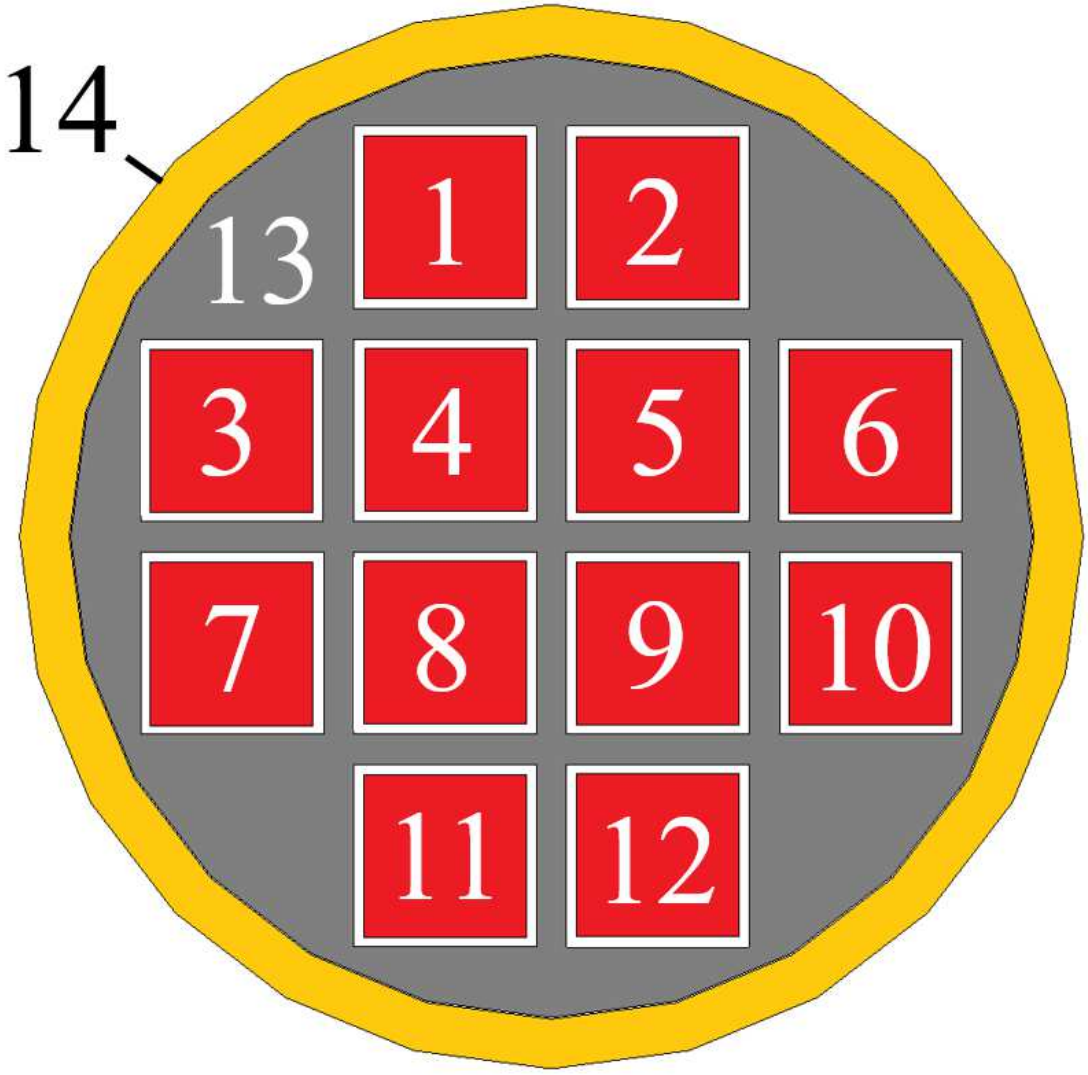

Figure 7.7: The constructed model geometry.

The bin sizes for the sinogram were determined by creating multiple sinograms with bin sizes ranging from 1-3 cm in ρ (increasing in 1 cm steps) and 0.5°-3° in φ (increasing in 0.5° steps), using the full cask data. For each sinogram, the total

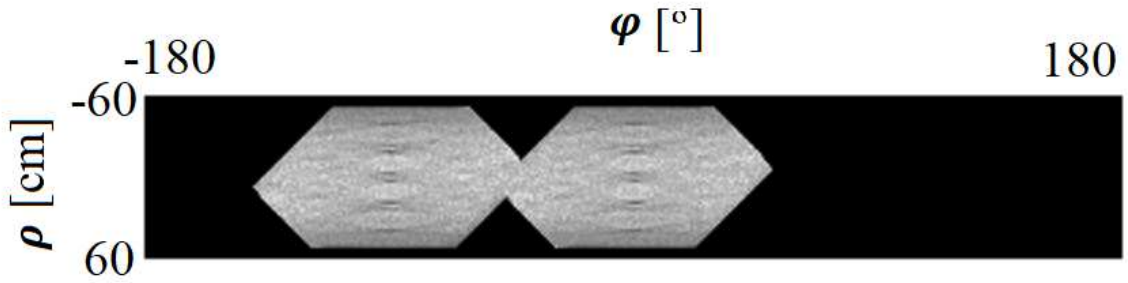

Figure 7.8: A partial sinogram of a full fuel cask created from two 12 hour counting time data sets, separated by a 90° rotation. The sinograms had 60, 2 cm bins along the cask width (ρ) and 360, 1° bins in rotation about the central axis of the cask (φ). Black indicates regions where no scattering data was collected.

variation (TV) of the sinogram was calculated as

$$TV = \frac{1}{K} \sum_i \sum_j \sqrt{(s_{i+1,j} - s_{i,j})^2 + (s_{i,j+1} - s_{i,j})^2}, \tag{7.2}$$

where $s_{i,j}$ was the value of the sinogram at the ith ρ bin and the jth φ bin, and K was the total number of summed elements. Sinogram pixels only contributed to equation 7.2 if all the sinogram pixels used contained a multi-group fit value. The TV value had a minimal value when ρ had 2 cm bins and φ had 1° bins. Minimizing the TV for multiple sinogram bin sizes allowed the data to be binned and fit in a way that minimized the difference between adjacent sinogram pixels. This provided the multigroup fitter with sufficient data in each bin to fit similar values in adjacent bins, where there were like areal density values. TV minimization of the sinogram in this manner was akin to smoothing the sinogram. Smoothing the sinogram on scales much smaller than the size of a fuel bundle helped to ensure that the sinogram consistently constrained the scattering densities of the model elements, resulting in more precise results.

The scattering densities for each cask model element were calculated using the partial sinogram data for each simulation scenario. The ratio of the calculated scat-

tering densities to those calculated for a full cask were taken for each model element. Graphs of the ratio values of each model element for the non-rotated and rotated data sets with one fuel bundle removed are shown in Figure 7.9. The error bars only indicate statistical error. It is evident by inspection that the deviation of the calculated ratio values from the predicted value of 1 is smaller in the case of the rotated data than for the non-rotated data. Table 7.1 shows the mean ratio value of the fuel bundle elements as well as the standard deviation from the mean. The calculations omitted cask element 9, which was the element used for diversion scenarios. Overall, the mean ratio value is closer to 1 and the standard deviation is smaller when a 90° rotation was included in the data set.

	Half Bundle Removed—non-rotated
Mean Ratio Value	1.003
σ	0.051
	Half Bundle Removed—rotated
Mean Ratio Value	1.002
σ	0.011
	One Bundle Removed—non-rotated
Mean Ratio Value	1.009
σ	0.033
	One Bundle Removed—rotated
Mean Ratio Value	1.004
σ	0.011
	One Bundle Replaced with Pb—non-rotated
Mean Ratio Value	1.002
σ	0.005
	One Bundle Replaced with Pb—rotated
Mean Ratio Value	1.001
σ	0.004

Table 7.1: The estimated mean ratio and the standard deviation from the mean for each diversion scenario. Each calculation omitted cask element 9, which either was missing fuel or had fuel replaced by Pb.

Using the cask model fitter method, the sensitivity to each diversion scenario was greater than the sensitivity from using the radiography style method (projecting the

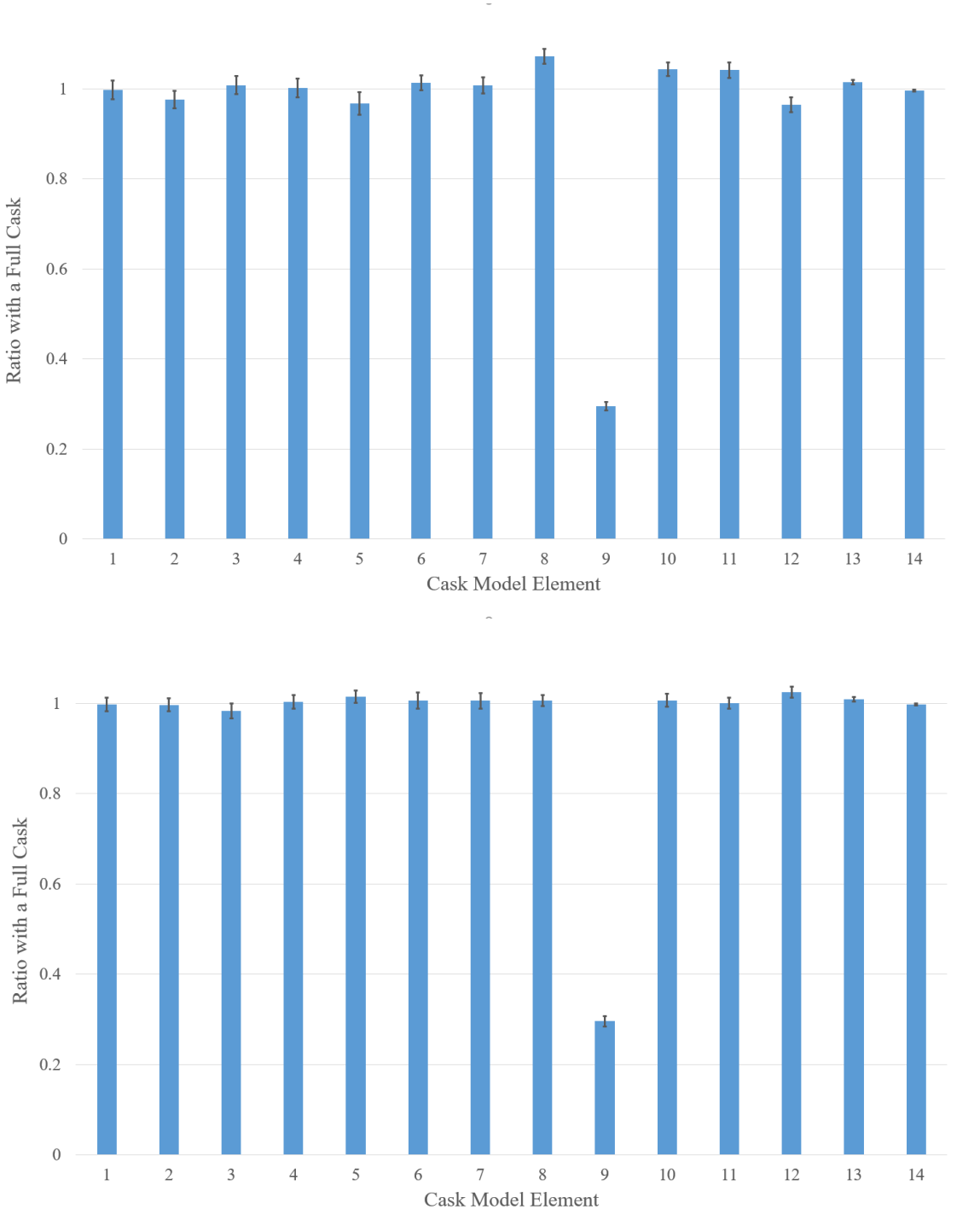

Figure 7.9: The ratios of each model element for a cask with one missing fuel bundle for the non-rotated data set (above) and the rotated data set (below).

tracks to a single plane). For the non-rotated data, the differences in the calculated ratio from the expected value of 1 were: 17.0 σ for a half bundle removed, 77.3 σ for one bundle removed, and 4.3 σ for one bundle replaced with Pb. The sensitivities increased in the case of rotating the cask by 90° after 12 hours, where differences in the calculated ratio from the expected value of 1 increased to: 27.9 σ for the removal of a half bundle, 102.2 σ for the removal of one bundle, and 5.2 σ for when one bundle was replaced with Pb. Figure 7.10 shows the calculated ratios of the diverted fuel bundle element for non-rotated and rotated data with the statistical error bars.

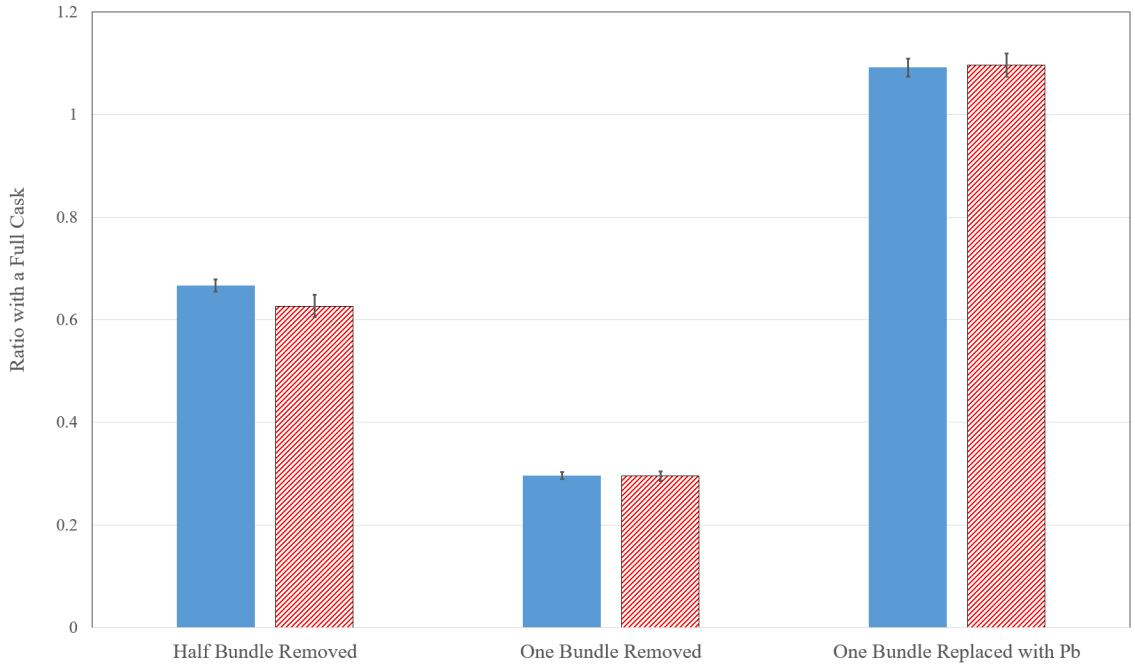

Figure 7.10: The calculated ratio of scattering densities of the diverted fuel bundle element for each diversion scenario, for both non-rotated (textured red) and rotated (solid blue) data.

7.2.3 Sensitivity to Rotation

One final analysis was performed to investigate the sensitivity of the cask model fitting method to an incorrect rotational alignment between the cask model and the data. The areal density sinograms had been binned according to the incident muon angle,

relative to the cask's central axis. Shifting the sinogram by a 1° bin was analogous to taking data on a cask that was 1° misaligned with the assumed geometry. The cask model fitting analysis was performed for 5°, 4°, and 3° misalignments. These rotations corresponded to 2.75 cm, 3.67 cm, and 4.58 cm differences between the rotated and correct orientations, along the circumference of the cask. While it is expected that engineering controls could guarantee correct alignment, even manual alignment of the cask should be able to achieve better precision than even a 3° misalignment.

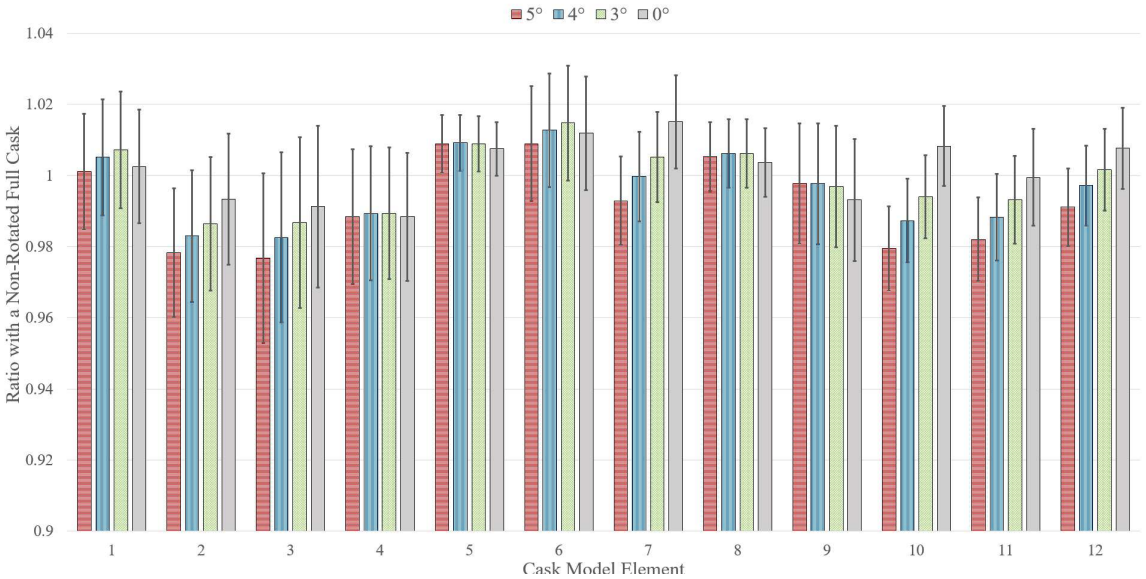

Figure 7.11: The calculated ratio of scattering densities of the diverted fuel bundle element for a full cask with rotational misalignment.

The ratio of the calculated scattering density of each model element for the rotationally misaligned data was taken to that of the correctly aligned data. Figure 7.11 shows the ratio values for 0°, 3°, 4°, and 5° misalignments. The fuel bundle elements 4, 5, 8, and 9 were located closest to the center of the cask, so the rotation misalignment affected these bundles the least. This was evident from the consistency of the ratio values as a function of rotational misalignment. All other fuel bundle elements had values that typically decreased away from the expected ratio as a function of rotational misalignment. These elements experienced a greater displacement in po-

sition, due to the increased distance from the cask's axis of rotation. However, even up to a 5° rotational misalignment, the calculated ratio values never reached above a 2 σ discrepancy from the predicted ratio of 1. Table 7.2 lists the discrepancy, in number of standard deviations, of the calculated scattering density ratio as a function of rotational misalignment.

Cask Model Element	Rotational Misalignment			
	0°	3°	4°	5°
1	0.157	0.439	0.315	0.069
2	0.359	0.726	0.920	1.195
3	0.383	0.553	0.728	0.970
4	0.646	0.572	0.563	0.608
5	0.987	1.142	1.171	1.098
6	0.742	0.917	0.795	0.556
7	1.151	0.409	0.0228	0.572
8	0.383	0.647	0.644	0.545
9	0.399	0.185	0.136	0.133
10	0.735	0.512	1.079	1.731
11	0.037	0.554	0.967	1.524
12	0.671	0.144	0.249	0.820

Table 7.2: The deviation of the calculated ratio of scattering densities for each cask model fuel bundle element in number of standard deviations as a function of rotational misalignment.

7.3 Validity of Simulations

It is worth noting that the data analyzed was produced to imitate data take from practical muon detectors. While the muon position vectors were perfectly precise, at the simulated detector planes, the muon direction vectors were blurred so that the muon scattering resolution was limited to 10 milliradians. Actual drift tube detectors are known to have spatial resolutions of a few hundred μm and angular resolutions of a few milliradians to sub-milliradian [114, 115]. In this analysis, since muon tracks are projected along their direction vector, discrepancies in angular resolution affect

the resulting analysis much more than spatial resolution (assuming spatial resolution would be sub-mm).

The tracking efficiency of the simulated detector planes was 100% which may be considered unrealistic. However, gaseous anode wire detectors and scintillator detectors are known to typically have efficiencies above 95%, which should not have drastically adverse effects on the presented results. Systematic errors in an actual muon detector cask imaging system (such as variations in barometric pressure, detector geometry, detector efficiency, and other experimental variables) would still need to be addressed, though the ratios taken in the analysis should help to minimize overall systematic errors in the results. Statistical error could also be reduced by taking an initial data set on a known full cask for a time longer than 24 hours, which effectively reduces statistical error of the scattering signal for a full cask to zero.

The muon momentum spectrum was generated from a parameterization that was fit to actual muon momentum data [81], and muon momenta recorded in the data set. Many efforts have been made to create analysis algorithms that incorporate muon momentum, in order to better estimate muon paths [54, 116] by which they intend to increase the resolution of the reconstructed image. Efforts have been made to measure the muon momentum, such as [54] which estimates muon energies after they have traversed the muon detectors and [117] which estimates muon energies from multiple coulomb scatting within the drift tube planes. The analysis presented here makes no use of individual muon momentum information, requiring only muon track position and direction information.

The performed analysis provided high sensitivity to the removal of spent nuclear fuel from the fuel bundle assemblies. It also showed sensitivity to the replacement of the fuel with Pb. All the data simulated could easily be produced with current detector technologies, and requires only 1 day to collect. The additional requirements of placing a cask suspended between two detectors with correct alignment and the

ability to rotate it are additional engineering challenges; though no obvious technical challenges should prevent this from being accomplished.

7.4 Conclusion

Simulations of BWR spent fuel casks were performed, with each data set being the equivalent of 12 hours counting time. Radiography style analysis of the simulated cask with 24 hours equivalent of data resulted in sensitivity to a half removed bundle at 8.3 σ and the removal of a whole bundle at 11.2 σ. Additional simulations with 12 hours of data after rotating the cask 90° were combined with 12 hours of data prior to rotation. The cask modeling method was used to make estimates of the scattering density within the cask. This method increased sensitivity to 27.9 σ for removing a half bundle and 102.2 σ for removing an entire bundle. Sensitivity to the replacement of a fuel bundle with Pb rods was 5.2 σ. The cask modeling method was also robust against falsely identifying a fully loaded cask as a diversion scenario with rotational misalignment up to 5°.

Chapter 8

Conclusion

The IAEA is tasked with the mission of verifying that special fissionable material is used only for peaceful purposes in non-weapon member states of the NPT. There are currently no deployed technologies that allow IAEA inspectors to verify the contents of spent nuclear fuel storage casks *in situ* once continuity of knowledge of the cask contents has been lost. Several simulation studies have been carried out that indicate that cosmic-ray muons would be a useful radiographic probe to verify spent fuel cask contents due to their highly penetrating nature, their scattering sensitivity to materials with high Z numbers, and their consistency as a source of background radiation. The LANL Threat Reduction Team has carried out the first cosmic-ray muon measurements on a spent fuel cask; measurements were made on an MC-10 cask stored at INL.

The LANL measurements were made with a generic drift tube detector, with reduced efficiency due to radiation backgrounds near the cask surface. However, simple analysis techniques were sufficient to show a sensitivity to a removed fuel bundle at 2.3 σ. The measurement data was also used to benchmark Geant4 simulations of an MC-10 fuel cask using the Reyna muon momentum model and a separate muon momentum model developed at LANL. In both cases, a normalization factor was used to bring simulation into agreement with experimental data; this indicated a potentially insufficient description of muon momenta below 1 GeV. However, simulation accurately captured the gross features seen with experimental data, giving confidence

to other simulated results.

Simulations were performed of the MC-10 spent fuel cask using idealized cylindrical detectors. The simulation data was used to create a sinogram of the fuel cask, which was reconstructed using filtered back-projection. This analysis showed the first application of computed tomography to muon scattering data. Using this method, the sensitivity of a missing fuel bundle was shown to be 17.9 σ. The reconstruction was also shown to accurately reconstruct the scattering density fuel cask components, as well as the stopping power of the components. A technique was developed which allowed the fuel cask to be described by a small number of model elements, rather than a large pixelated image; this assumed that the corresponding elements spatial positions were known. The cask model used sinogram data to reconstruct the model element's scattering densities and was able to do so with limited sinogram data.

Additional simulations were performed of a TN-24P spent fuel cask, which was loaded with different fuel burnups and fuel diversion scenarios. Two methods were presented to show the sensitivity of cosmic-ray muon scattering to changes in burnup of the fuel, as well as the diversion of fuel bundles. The methods utilized were cask element model scattering density reconstruction and an average sinogram value compared against the signals for a full cask. The muon scattering signal changed by 2.5% between fresh and spent fuel with a burnup of 5.5%. Spent fuel diversion scenarios were detected with sensitivities of: 1.67 σ for replacement with a fresh bundle, 60.24 σ for the removal of a bundle, 10.95 σ for replacement with a bundle containing lead rods, and 48.49 σ for replacement with a bundle containing steel rods.

A final round of simulations was performed to demonstrate the feasibility of using cosmic-ray muons to perform a final verification of spent fuel prior to its deposition in a geological repository and removal from safeguards. BWR spent fuel casks were simulated and a realistic muon detector was simulated. The detector was given an intrinsic limiting resolution on muon scattering of 10 milliradians; 12 data equivalent

hours of muons were simulated for each data set. Simple analysis methods like those used on the INL muon measurement data were applied to 24 hrs of data which showed sensitivities of: 16.5 σ in for the removal of a half fuel bundle, 25.1 σ for the removal of a single bundle, and 3.0 σ for replacement with a bundle containing lead rods. A geometric model of the cask was created and partially filled sinograms were created from 24 hrs of data with a 90-degree rotation applied to the cask after 12 hrs. The sensitivity to fuel diversion dramatically increased to: 27.9 σ in for the removal of a half fuel bundle, 102.2 σ for the removal of a single bundle, and 5.2 σ for replacement with a bundle containing lead rods. Rotational misalignment up to 5° did not cause false positives in the case of a full cask.

The results from experiment and simulation offer compelling evidence of the utility of cosmic-ray muons to be used as radiographic probes of spent nuclear fuel casks.

Chapter 9

Future Work

9.1 A Larger Muon Tracker

The measurement campaign at INL had a number of difficulties, namely:

1. The width of the fuel basket was larger than the width of the 1.2×1.2 m^2 detector supermodules.

2. A large aluminum table was used to elevate the upper supermodule, this complicated positioning, and maintenance of the detector.

3. Strong winds buffeted the supermodules' enclosures which cause the lower supermodule to shift position, thus losing the continuity of the coordinate system.

4. An adjacent tube trigger needed to be implemented in order to identify muon tracks through the radiation background. The trigger cut tracking efficiency by approximately 50%.

While a system for deployment use by the IAEA would require a commercial effort to optimize, the LANL threat reduction team has recently acquired a larger drift tube detector that would help to overcome some of the measurement difficulties. The MMT that is currently used at LANL has a planar area of 1.2×1.2 m^2 and is shown in Figure 9.1. The new, larger, drift tube detector is shown in Figure 9.2. The new detector has two supermodule pairs with planar areas of 1.8×1.8 m^2 and 1.8×2.4 m^2, both of which have operating characteristics similar to the MMT.

Figure 9.1: The currently used MMT detector at Los Alamos National Laboratory.

Figure 9.2: The new drift tube detector at Los Alamos National Laboratory.

With proper engineering and foresight, the detectors could both be placed on the ground on the 1.8 m side, allowing the detectors to rise 2.4 m vertically. Placing the detectors in this configuration would provide multiple benefits. First, coverage of approximately 1.8 m along the width of the cask would allow the fuel basket to be captured within a single position. Second, vertical coverage of the supermodules precludes the necessity of elevating one above the other, increasing the ease of installation and movement of the supermodules. Third, high vertical coverage by both supermodules would also allow the cask to be imaged by muons entering the cask from both sides of the cask; knowing that incident muon tracks are higher than exiting muon tracks would be sufficient to distinguish coincident tracks in the supermodules.

A major issue that could remain unsolved by using the larger detector would be the use of the adjacent tube trigger. One possible solution may be increasing the standoff distance of the detector supermodules. Knowing the muon tracking rate as a function of the distance between the two detectors may provide an optimal standoff distance. The optimal distance would not require the use of the adjacent tube trigger, but the muon tracking rate would be higher than the configuration of supermodules close to the cask with the trigger implemented. Accurately determining the optimal configuration would need to be performed *in situ* and would need to be calculated into the setup time.

9.2 Modification of the Multi-Group Model

Some modification of the multi-group was performed in Chapter 6 in order to account for the muon's energy loss as it traversed the cask. Here, two modifications to the muon model are presented. First, the multi-group model assumes that the cosmic-ray muon spectrum can be described by seven momentum groups: 0.25 GeV, 0.5 GeV, 1 GeV, 2 GeV, 4 GeV, 8 GeV, and 16 GeV. Work has been done to reduce an overparameterized mixing model to an optimum number of groups by creating the regularized

estimation-maximization (REM) algorithm [118]. The REM algorithm iteratively computes the maximum likelihood estimates of the parameters, while applying a regularization term in the form of Shannon's entropy. The algorithm attempts to strike a balance between increasing the log-likelihood by over-fitting data with too many mixture groups and minimizing Shannon's entropy which grown as the number of parameters is increased. Application of the REM algorithm to the multi-group model is given in Appendix A.

In addition to estimating the values and number of momentum groups, the multi-group model can be modified to estimate the momentum loss of the muons. As mentioned in Chapter 3, Eyges derived a pdf for muon scattering that accounted for momentum loss [76]. The change in the muon momentum spectrum can be applied to the multi-group model if it assumed that the muon momentum loss is constant for the materials and independent of muon energy. These assumptions are crude, but not unrealistic as long as the object does not stop most of the incident muons. The necessary modifications to the multi-group model to provide momentum loss estimation is given in Appendix B.

9.3 Enhancing Sinogram Data with Cubic Spline Paths

Recent work has been performed that attempts to reconcile the scattering path of the muon with the straight path of sinogram rays [119]. Several methods for filling a sinogram were proposed, including a method similar to the method here described, meaning incident muon tracks were used as the basis for sinogram filling. No direct comparison should be attempted between the two methods since those in [119] use a pixelated volume and fill the sinogram according to sums of distribution widths and the method here described uses the multi-group model. However, the work indicated that accounting for deviation from the incident muon direction, using POCA, improved cask image reconstruction and sensitivity to diverted fuel.

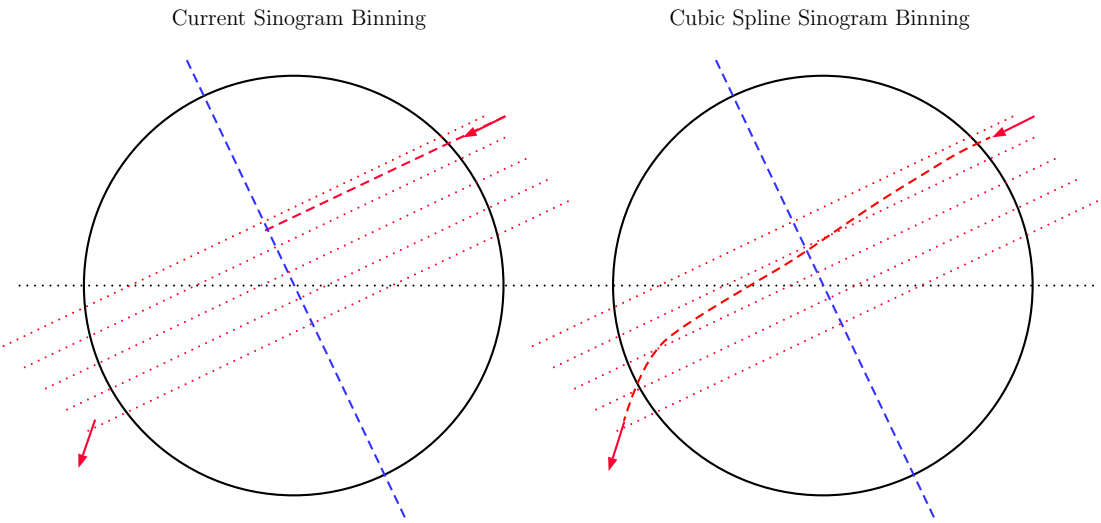

Figure 9.3: The current method for filling a sinogram bin (left), where the muon's scattering angle is used to fill a single bin that is parallel to the incident muon track. A cubic spline method (right), where the muon's scattering angle is used to fill all bins that the cubic spline track passes through (and are parallel to the incident muon track).

Similar methods could be applied to sinograms that are constructed using the multi-group model. Rather than applying the POCA method, the cubic spline method could be used to fill the muon scattering angle in multiple sinogram bins, as shown in Figure 9.3. The cubic spline path (CSP) method is a charged particle path predictor that has been developed in the field of medical physics for use in proton computed tomography [120]. Use of the cubic spline method is comparable to using the most likely muon path (MLP) to fill the sinogram; both methods are explained in Appendix C.

Use of both the MLP and CSP require knowledge of the outer geometric boundaries of the object being imaged. The incident and exiting tracks are projected to the boundary of the object and then the position and directional information are used to estimate the muon's path through the object. A comparison of the MLP and CSP paths to the actual simulated muon path through one of the copper-lined casks described in Chapter 7 is shown in Figure 9.4. The MLP was calculated using

scattering density information from the simulation which would not be available using real muon detectors. The CSP was calculated using only the position and direction information recorded by muon detectors. An additional comparison with the POCA paths was performed, where the closest distance between the actual muon path and the POCA was recorded as well as the largest distance between the actual muon path and the CSP. The distributions of both the closest approach to POCA and the largest deviation from CSP for values under 40 cm are shown in Figure 9.5. The data indicate that use of the CSP has a narrower distribution and lower mean than POCA in terms of deviation from the muon path. Additional work should investigate if using the CSP to construct the sinogram offers any enhancements in image reconstruction.

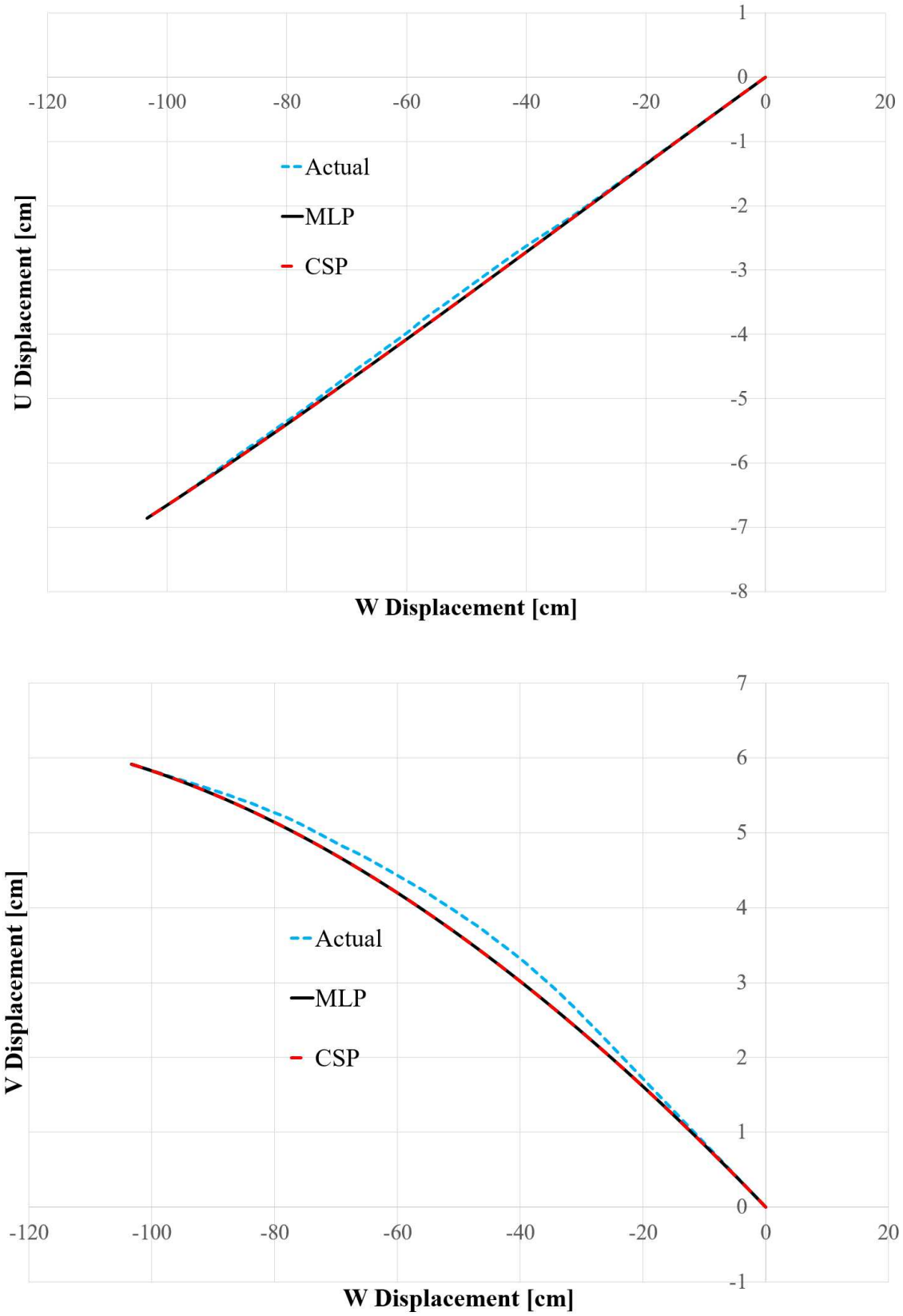

Figure 9.4: The actual simulated muon path (blue dashed) as well as the calculated MLP (black solid) and CSP (red dashed) as it traverses a cask. W is along the initial muon direction and U and V are the directions mutually orthogonal to the muon track.

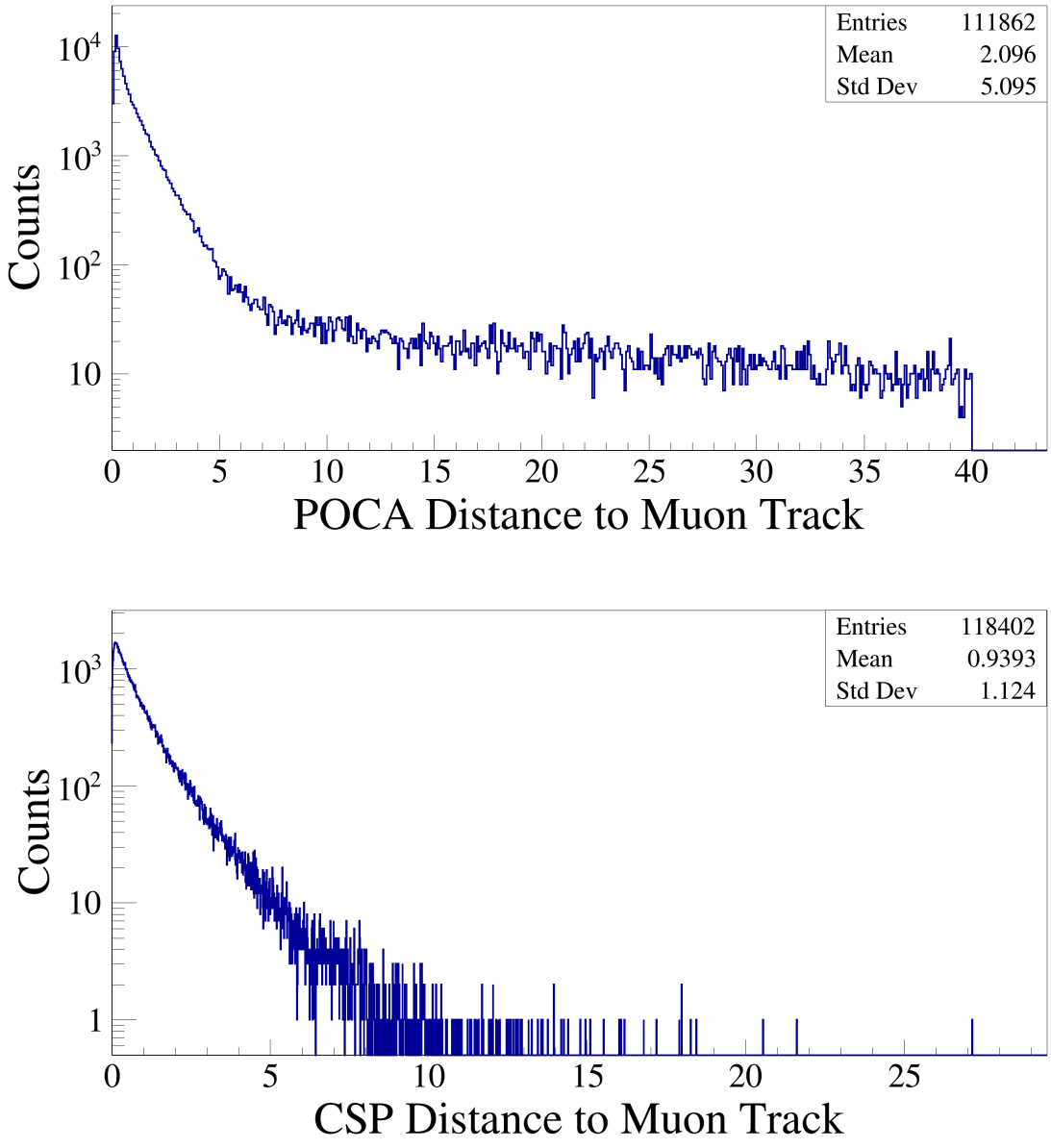

Figure 9.5: The.

Appendix A

Estimating Muon Momentum Groups using REM

The multi-group probability distribution function(pdf) for scattering angles between incident and exiting muon tracks is

$$f(\boldsymbol{\theta}, \boldsymbol{\Psi}) = \sum_i \alpha_i f(\theta|\psi_i)$$

where ψ_i contain the fit parameters for group i and

$$f(\theta|\psi_i) = \frac{\theta}{\theta_i^2} \exp\left[-\frac{\theta^2}{2\theta_i^2}\right]$$

with $\theta_i = \frac{13.6 \text{ MeV/c}}{\beta_i p_i} T$, $T = \sqrt{t}(1 + 0.038 \ln[t])$, t is the number of radiation lengths that the muon has passed through, $\beta_i c$ is the muon velocity for group i, and p_i is the muon momentum of group i, and α_i is the weighted amplitude of group i. If T is known, then optimal estimates for α_i and p_i can be made using sufficient statistics of θ and the regularized expectation-maximization (REM) algorithm. The REM algorithm is given by Li in [118]; derivations of A.1 and A.2 can be found at an author's supplemental website (`https://haifengl.wordpress.com/2014/07/17/the-regularized-em-algorithm/`), here only application of the algorithm to choosing momentum groups is shown.

First, the Bayesian prior for iteration k is found via

$$f(p_i|\theta_j;\boldsymbol{\Psi}^{(k)}) \equiv \frac{\alpha_i f(\theta_j|\psi_i)}{\sum\limits_m \alpha_m f(\theta_j|\psi_m)}.$$

The prior is used to calculate each iterations weighted amplitude

$$\alpha_i^{(k+1)} = \frac{\sum\limits_j f(p_i|\theta_j;\boldsymbol{\Psi}^{(k)})(1+\gamma\ln[f(p_i|\theta_j;\boldsymbol{\Psi}^{(k)})])}{\sum\limits_j\sum\limits_i f(p_i|\theta_j;\boldsymbol{\Psi}^{(k)})(1+\gamma\ln[f(p_i|\theta_j;\boldsymbol{\Psi}^{(k)})])}, \tag{A.1}$$

where γ is a mixing parameter for the Shannon entropy with the log likelihood and is greater than zero.

Li showed that if the pdf has the regular exponential-family form,

$$f(\theta|\psi_i) = \nu(\theta)e^{\psi_i^T\zeta(\theta)-\varphi(\psi_i)}$$

—where $\nu(\theta)$ is a known function, $\zeta(\theta)$ is a vector of sufficient statistics containing that data, ψ_i is a vector containing the fit parameters, and $\varphi(\psi_i)$ is a normalizing function of ψ_i defined by

$$\varphi(\psi_i) \equiv \ln\left[\int \nu(\theta)e^{\psi_i^T\zeta(\theta)}d\theta\right]$$

—then the expectation value of ψ_i is given by:

$$E[\zeta(\theta)|\psi_i^{(k+1)}] = \frac{\sum\limits_j \zeta(\theta_j)f(p_i|\theta_j;\boldsymbol{\Psi}^{(k)})(1+\gamma\ln[f(p_i|\theta_j;\boldsymbol{\Psi}^{(k)})])}{\sum\limits_j f(p_i|\theta_j;\boldsymbol{\Psi}^{(k)})(1+\gamma\ln[f(p_i|\theta_j;\boldsymbol{\Psi}^{(k)})])}. \tag{A.2}$$

The muon scattering pdf can be re-written as

$$f(\theta|\psi_i) = \nu(\theta)e^{\psi_i^T\zeta(\theta)-\varphi(\psi_i)}$$

where $\nu(\theta) = \theta$, $\zeta(\theta) = -\theta^2/2$, and $\psi_i = 1/\theta_i^2$. From these definitions, it is easy to calculate

$$\varphi(\psi_i) = \ln\left[\int_0^\infty \theta e^{-\frac{\theta^2}{2\theta_i^2}} d\theta\right] = \ln\left[\theta_i^2\right] = \ln\left[\frac{1}{\psi_i}\right].$$

The expected value of an exponential-family parameter is given by

$$E[\zeta(\theta)|\psi_i] = \nabla_{\psi_i}\varphi(\psi_i);$$

for the muon scattering pdf, the expectation value is

$$\begin{aligned} E[\zeta(\theta)|\psi_i] =& \nabla_{\psi_i}\varphi(\psi_i) \\ =& -\frac{1}{\psi_i} \\ =& -\frac{1}{\theta_i^2} \\ =& -\frac{\beta_i^2 p_i^2}{(13.6\text{ MeV/c})^2 T^2}. \end{aligned} \tag{A.3}$$

For a given detector geometry, calibration objects with known values of T can be used (as done in [79]) to determine what the momentum groups values and amplitudes are by iteratively solving A.1 and A.2. The values of A.3 are equal to the values determined by A.2, i.e.:

$$\frac{\sum_j -\frac{\theta_j^2}{2} f(p_i|\theta_j;\boldsymbol{\Psi}^{(k)})(1+\gamma\ln[f(p_i|\theta_j;\boldsymbol{\Psi}^{(k)})])}{\sum_j f(p_i|\theta_j;\boldsymbol{\Psi}^{(k)})(1+\gamma\ln[f(p_i|\theta_j;\boldsymbol{\Psi}^{(k)})])} = -\frac{\beta_i^2 p_i^2}{(13.6\text{ MeV/c})^2 T^2}$$

Once the solution converges, groups whose amplitudes are below some small threshold value can be removed from the model. The remaining groups are the optimal number of momentum groups necessary to model the muon spectrum for the configured detector. The final values from A.2, after convergence, can be used with A.3 to

determine the muon momenta. The relativistic quantity β_i can be approximated as 1, or $\beta_i^2 p_i^2$ can be written in terms of muon mass and momentum:

$$\beta_i^2 p_i^2 = \frac{p_i^4}{m^2 + p_i^2}.$$

Appendix B

Momentum Loss Estimation using the Multi-Group Model

Eyges pdf for multiple coulomb scattering of charged particles in a material can be written as

$$f(\theta|\psi_i) = \frac{\theta}{A_0} e^{-\frac{\theta^2}{2A_0}}, \tag{B.1}$$

with

$$A_0 = (13.6 \text{ MeV/c})^2 (1 + 0.038 \ln[t])^2 \int_0^t \frac{1}{p^2(\eta)\beta^2(\eta)} d\eta \tag{B.2}$$

—from Lynch's and Dahl's correction. The term $p^2\beta^2$ can be written in terms of the muon momentum and energy as

$$\beta^2 p^2 = \frac{p^4}{m^2 + p^2}. \tag{B.3}$$

Eyges suggested that a reasonable approximation assumed that the rate of momentum loss was independent of momentum and could be estimated as a function of t, allowing the momentum of the particles to be written as:

$$p(t) = p_0 - \epsilon t, \tag{B.4}$$

where p_0 was the initial particle momentum and ϵ was the momentum loss per radiation length. Equation B.4 can be combined with B.2 and B.3 to produce

$$\begin{aligned} A_0 =&(13.6 \text{ MeV/c})^2(1+0.038\ln[t])^2 \int_0^t \frac{m^2+(p_0-\epsilon\eta)^2}{(p_0-\epsilon\eta)^4}d\eta \\ =&(13.6 \text{ MeV/c})^2(1+0.038\ln[t])^2 \left[\frac{t}{p_0(p_0-\epsilon t)}\left(1+\frac{m^2}{(p-\epsilon t)^2}\left[1-\frac{\epsilon t}{p_0}+\frac{(\epsilon t)^2}{3p_0^2}\right]\right)\right]. \end{aligned}$$

The scattering pdf is then modified to

$$\begin{aligned} f(\theta|\psi_i) =&\frac{\theta p_0(p_0-\epsilon t)}{(13.6 \text{ MeV/c})^2 t(1+0.038\ln[t])^2 h(t,\epsilon)} \\ &* \exp\left[-\frac{\theta^2 p_0(p_0-\epsilon t)}{2(13.6 \text{ MeV/c})^2 t(1+0.038\ln[t])^2 h(t,\epsilon)}\right], \end{aligned} \tag{B.5}$$

where

$$h(t,\epsilon) = 1-\frac{\epsilon t}{p_0}+\frac{(\epsilon t)^2}{3p_0^2}. \tag{B.6}$$

The frame work from A can be used to iteratively calculate the values of ϵ and t, using A.2 and A.3. The expectation value can be calculated in the same way as A.3; however, the value of θ_i^2 has now been modified to

$$\theta_i^2 = \frac{(13.6 \text{ MeV/c})^2 t(1+0.038\ln[t])^2 h(t,\epsilon)}{p_i(p_i-\epsilon t)}.$$

Also, the regularizing term γ can be set to 0, since there is no modification to the number of groups at this point. The equation to be solved at each iteration is then

$$-E[\zeta(\theta)|\psi_i^{(k+1)}] = \frac{\sum_j \frac{\theta_j^2}{2} f(p_i|\theta_j;\boldsymbol{\Psi}^{(k)})}{\sum_j f(p_i|\theta_j;\boldsymbol{\Psi}^{(k)})} = \frac{p_i(p_i-\epsilon t)}{(13.6 \text{ MeV/c})^2 t(1+0.038\ln[t])^2 h(t,\epsilon)}. \tag{B.7}$$

If $(1 + 0.038\ln[t])^2$ and $h(t, \epsilon)$ are assumed to be slowly varying functions, such that

$$(1 + 0.038\ln[t^{(k)}])^2 \simeq (1 + 0.038\ln[t^{(k+1)}])^2 \text{ and}$$
$$h(t^{(k)}, \epsilon^{(k)}) \simeq h(t^{(k+1)}, \epsilon^{(k+1)}),$$

then B.7 can be modified to become

$$\begin{aligned}\Omega_i(\boldsymbol{\Psi}^{(k+1)}) &\equiv \frac{\sum_j \frac{\theta_j^2}{2} f(p_i|\theta_j; \boldsymbol{\Psi}^{(k)})}{\sum_j f(p_i|\theta_j; \boldsymbol{\Psi}^{(k)})}(1 + 0.038\ln[t^{(k)}])^2 h(t^{(k)}, \epsilon^{(k)})(13.6 \text{ MeV/c})^2 \\ &= \frac{p_i(p_i - \epsilon^{(k+1)}t^{(k+1)})}{t^{(k+1)}}. \end{aligned} \tag{B.8}$$

Equation B.8 can be used to create a least-squares residual over the momentum groups:

$$\chi^2 \equiv \sum_i \left(\Omega_i(\boldsymbol{\Psi}^{(k+1)}) - \frac{p_i(p_i - \epsilon^{(k+1)}t^{(k+1)})}{t^{(k+1)}} \right)^2. \tag{B.9}$$

Minimizing B.9, by setting partial derivatives equal to zero, allows $t^{(k+1)}$ and $\epsilon^{(k+1)}$ to be solved simultaneously using the matrix equation

$$\begin{bmatrix} \sum_i p_i^3 & -\sum_i p_i^2 \\ \sum_i p_i^4 & -\sum_i p_i^3 \end{bmatrix} \begin{bmatrix} \frac{1}{t^{(k+1)}} \\ \epsilon^{(k+1)} \end{bmatrix} = \begin{bmatrix} \sum_i \Omega_i(\boldsymbol{\Psi}^{(k+1)} p_i \\ \sum_i \Omega_i(\boldsymbol{\Psi}^{(k+1)} p_i^2 \end{bmatrix}$$

for a final solution of

$$t^{(k+1)} = \frac{\left(\sum_i p_i^3\right)^2 - \left(\sum_i p_i^2\right)\left(\sum_i p_i^4\right)}{\left(\sum_i p_i^3\right)\left(\sum_i \Omega_i(\boldsymbol{\Psi}^{(k+1)} p_i\right) - \left(\sum_i p_i^2\right)\left(\sum_i \Omega_i(\boldsymbol{\Psi}^{(k+1)} p_i^2\right)} \tag{B.10}$$

$$\epsilon^{(k+1)} = \frac{\left(\sum_i p_i^4\right)\left(\sum_i \Omega_i(\boldsymbol{\Psi}^{(k+1)} p_i\right) - \left(\sum_i p_i^3\right)\left(\sum_i \Omega_i(\boldsymbol{\Psi}^{(k+1)} p_i^2\right)}{\left(\sum_i p_i^3\right)^2 - \left(\sum_i p_i^2\right)\left(\sum_i p_i^4\right)} \tag{B.11}$$

The weights for each momentum group should also be functions of the quantity ϵt—to account for attenuation of the energy groups—while maintaining the sum $\sum_i \alpha_i(\epsilon, t) = 1$. There are multiple way to do this, the simplest is allow the weights to change by linear attenuation as

$$\alpha_i(\epsilon, t) = \frac{\alpha_i(p_i)\frac{p_i - \epsilon t}{p_i}}{\sum_m \alpha_m(p_m)\frac{p_m - \epsilon t}{p_m}},$$

where $\alpha_i(p_i)$ is the initial weight of the ith momentum group. Alternatively, exponential attenuation could also be modeled by

$$\alpha_i(\epsilon, t) = \frac{\alpha_i(p_i)\exp\left[\frac{-\epsilon t}{p_i - \epsilon t}\right]}{\sum_m \alpha_m(p_m)\exp\left[\frac{-\epsilon t}{p_m - \epsilon t}\right]}.$$

Better or more physically motivated models for attenuation groups should be investigated. Changes in the momentum group weights do affect the calculated values of ϵ and t, but the effects are accounted for in the Bayesian prior

$$f(p_i|\theta_j; \boldsymbol{\Psi}^{(k)}) \equiv \frac{\alpha_i(\epsilon^{(k)}, t^{(k)}) f(\theta_j|\psi_i)}{\sum_m \alpha_m(\epsilon^{(k)}, t^{(k)}) f(\theta_j|\psi_m)},$$

which is used at each iteration.

Appendix C

Most Likely Path Formalism and the Cubic Spline Path

Predicting the most likely path of charged particles in a medium has been considered for decades [121–123]. Schulte presented the first application of Bayesian likelihoods to predict the location of charged particles in a homogeneous medium [124]. The methodology of Schulte is not presented in full here, since the original paper covers it in depth. However, the end result estimates the most likely position and scattering angle of a particle inside of a homogeneous material as:

$$\boldsymbol{r}_1 = \left(\boldsymbol{\Sigma}_1^{-1} + \boldsymbol{R}_1^T \boldsymbol{\Sigma}_2^{-1} \boldsymbol{R}_1\right)^{-1} \left(\boldsymbol{\Sigma}_1^{-1} \boldsymbol{R}_0 \boldsymbol{r}_0 + \boldsymbol{R}_1^T \boldsymbol{\Sigma}_2^{-1} \boldsymbol{r}_2\right) \tag{C.1}$$

The $\boldsymbol{r}$ vectors give the position and direction of the muon along the most likely path $\boldsymbol{r}_1$, at the incident location $\boldsymbol{r}_0$, at the exiting location $\boldsymbol{r}_2$ and have the form

$$\boldsymbol{r} = \begin{bmatrix} u \\ \theta_u \\ v \\ \theta_v \end{bmatrix},$$

where u, θ_u, v, and θ_v have the same definitions as found in Chapter 3. The R matrices describe a rotation from the incident or outgoing muon tracks to the reference frame

at the location of $\boldsymbol{r}_1$ and have the form

$$\boldsymbol{R}_i = \begin{bmatrix} 1 & t_j - t_i & 0 & 0 \\ 0 & 1 & 0 & 0 \\ 0 & 0 & 1 & t_j - t_i \\ 0 & 0 & 0 & 1 \end{bmatrix},$$

where $j = i + 1$ and i can correspond the entrance point (0) or the MLP point (1). The $\boldsymbol{\Sigma}$ matrices are co-variance matrices that contain Eyges' modified integrals

$$\begin{aligned} A_0(t_j, t_i) =& E_0^2(1 + 0.038 \ln[t_j - t_i])^2 \int_{t_i}^{t_j} \frac{1}{p^2(\eta)\beta^2(\eta)} d\eta \\ A_1(t_j, t_i) =& E_0^2(1 + 0.038 \ln[t_j - t_i])^2 \int_{t_i}^{t_j} \frac{(t_j - \eta)}{p^2(\eta)\beta^2(\eta)} d\eta \\ A_2(t_j, t_i) =& E_0^2(1 + 0.038 \ln[t_j - t_i])^2 \int_{t_i}^{t_j} \frac{(t_j - \eta)^2}{p^2(\eta)\beta^2(\eta)} d\eta \end{aligned}$$

and are of the form

$$\boldsymbol{\Sigma}_j = \begin{bmatrix} A_2(t_j, t_i) & A_1(t_j, t_i) & 0 & 0 \\ A_1(t_j, t_i) & A_0(t_j, t_i) & 0 & 0 \\ 0 & 0 & A_2(t_j, t_i) & A_1(t_j, t_i) \\ 0 & 0 & A_1(t_j, t_i) & A_0(t_j, t_i) \end{bmatrix}.$$

The formalism presented by Schulte assumes that the momentum of the charged particle is known at both the entrance and exit locations. However, muon tomography does not currently record momentum information for both incident and exiting muons. A simple modification is to remove the momentum dependence and assume that momentum is constant while the muon traverses the material. This assumption

changes Eyges' integrals to

$$A_0(t_j, t_i) = E_0^2(1 + 0.038 \ln[t_j - t_i])^2 \frac{(t_j - t_i)}{p^2\beta^2} \tag{C.2}$$

$$A_1(t_j, t_i) = E_0^2(1 + 0.038 \ln[t_j - t_i])^2 \frac{(t_j - t_i)^2}{2p^2\beta^2} \tag{C.3}$$

$$A_2(t_j, t_i) = E_0^2(1 + 0.038 \ln[t_j - t_i])^2 \frac{(t_j - t_i)^3}{3p^2\beta^2}. \tag{C.4}$$

Let the notation be simplified by introducing

$$\xi(j, i) \equiv \frac{E_0^2}{p^2\beta^2}(1 + 0.038 \ln[t_j - t_i])^2$$

and rewritting

$$t_j = W_j \frac{\rho}{X_0} = W_j \upsilon,$$

where W_j is the distance that muon has traveled along its initial trajectory and υ is the scattering density of material that the muon has traversed (approximated as a homogeneous material per the derivation of Schulte). Simplified Eyges' integrals become

$$A_0(j, i) = \xi(j, i)\upsilon(W_j - W_i) \tag{C.5}$$

$$A_1(j, i) = \xi(j, i)\upsilon \frac{(W_j - W_i)^2}{2} \tag{C.6}$$

$$A_2(j, i) = \xi(j, i)\upsilon \frac{(W_j - W_i)^3}{3}. \tag{C.7}$$

The new co-variance matrices are then written as

$$\boldsymbol{\Sigma}_j = \xi(j,i)\upsilon \begin{bmatrix} \frac{(W_j-W_i)^3}{3} & \frac{(W_j-W_i)^2}{2} & 0 & 0 \\ \frac{(W_j-W_i)^2}{2} & (W_j - W_i) & 0 & 0 \\ 0 & 0 & \frac{(W_j-W_i)^3}{3} & \frac{(W_j-W_i)^2}{2} \\ 0 & 0 & \frac{(W_j-W_i)^2}{2} & (W_j - W_i) \end{bmatrix}. \quad \text{(C.8)}$$

Reconstruction of the MLP using this frame work with simulated muon tracks and known scattering densities of the materials is relatively straight forward.

Additional work has been performed in which the path of a charged particle was predicted using a cubic spline path (CSP) [120]. The path is a parametric curve that is a function of the positions and directions of the incident and exiting tracks. The path is described by

$$S(t) = (2t^3 - 3t^2 + 1)\boldsymbol{X}_0 + (t^3 - 2t^2 + t)\boldsymbol{P}_0 + (-2t^3 + 3t^2)\boldsymbol{X}_1 + (t^3 - t^2)\boldsymbol{P}_1, \quad \text{(C.9)}$$

where $\boldsymbol{X}$ are the track positions, $\boldsymbol{P}$ are the track directions, 0 and 1 correspond to the incident and exiting tracks (respectively), and t is the track parameter with range $[0, 1]$. Track directions are defined as

$$\boldsymbol{P}_i = \hat{\boldsymbol{P}}_i|\boldsymbol{X}_1 - \boldsymbol{X}_0|.$$

The CSP requires only position and direction information but no momentum information, similar to the data that most muon detectors provide. However, the application of CSP requires approximate knowledge of the outer geometry of the object being imaged. In the cask of fuel cask tomography, the geometry and position are well known.

Bibliography

[1] R. G. Lange et al., Energy Conversion and Management **49**, Space Nuclear Power and Propulsion (2008).

[2] G. H. Rinehart, Progress in Nuclear Energy **39** (2001).

[3] IAEA, *Status and Advances in MOX Fuel Technology*, Technical Reports Series 415 (IAEA, Vienna, 2003).

[4] *Treaty on the Non-Proliferation of Nuclear Weapons*, `https://www.un.org/disarmament/wmd/nuclear/npt/`, 1968.

[5] *The IAEA Mission Statement*, `https://www.iaea.org/about/mission`.

[6] *Development and Implementation Support Programme for Nuclear Verification 2018—2019*, `https://www.iaea.org/sites/default/files/18/09/sg-str-386-development-support-programme.pdf`.

[7] *NNSA's Introduction to International Safeguards*, `https://www.energy.gov/nnsa/missions/nonproliferation`.

[8] K. Ziock et al., IEEE Nuclear Science Symposium Conference Record (2005).

[9] K. P. Ziock et al., Office of Scientific and Technical Information (OSTI) (2005).

[10] P. A. Santi et al., Los Alamos National Laboratory Report No. LA-UR-09-03480 (2009).

[11] X. Liu et al., NDT & E International **80** (2016).

[12] V. Brdar et al., Phys. Rev. Applied **8** (2017).

[13] M. Osterlund et al., Proceedings of International Workshop on Fast Neutron Detectors and Applications — PoS(FNDA2006) (2007).

[14] G. Jonkmans et al., Annals of Nuclear Energy **53** (2013).

[15] M. Furlan et al., 2013 3rd International Conference on Advancements in Nuclear Instrumentation, Measurement Methods and their Applications (ANIMMA) (2013).

[16] A. Clarkson et al., Nuclear Instruments and Methods in Physics Research Section A: Accelerators, Spectrometers, Detectors and Associated Equipment **746** (2014).

[17] F. Ambrosino et al., Journal of Instrumentation **10** (2015).

[18] A. Clarkson et al., Journal of Instrumentation **10** (2015).

[19] L. Frazão et al., Journal of Instrumentation **11** (2016).

[20] S. Chatzidakis et al., IEEE Transactions on Nuclear Science **63** (2016).

[21] A. Erlandson et al., CNL Nuclear Review (2016).

[22] E. P. George, Commonwealth Engineer (1955).

[23] L. W. Alvarez et al., Science **167** (1970).

[24] G. Lynch, Lawrence Berkeley National Laboratory. LBNL Report: LBL-2180 (1973).

[25] K Nagamine et al., Nuclear Instruments and Methods in Physics Research Section A: Accelerators, Spectrometers, Detectors and Associated Equipment **356** (1995).

[26] H. Tanaka et al., Hyperfine Interactions **138** (2001).

[27] H. Tanaka et al., Nuclear Instruments and Methods in Physics Research Section A: Accelerators, Spectrometers, Detectors and Associated Equipment **507** (2003).

[28] H. K. M. Tanaka et al., Journal of Geophysical Research **115** (2010).

[29] N. Lesparre et al., Geoscientific Instrumentation, Methods and Data Systems **1** (2012).

[30] A. Anastasio et al., Nuclear Instruments and Methods in Physics Research Section A: Accelerators, Spectrometers, Detectors and Associated Equipment **732**, Vienna Conference on Instrumentation 2013 (2013).

[31] F Ambrosino et al., Journal of Instrumentation **9** (2014).

[32] H. K. M. Tanaka et al., Nature Communications **5** (2014).

[33] A. H. Bonneville et al., FastTIMES, 21(4):29-34 (2016).

[34] J. Flygare et al., IEEE Transactions on Nuclear Science **65** (2018).

[35] A. Bonneville et al., Philosophical Transactions of the Royal Society A: Mathematical, Physical and Engineering Sciences **377** (2019).

[36] A. Menchaca-Rocha, Proceedings of 10th Latin American Symposium on Nuclear Physics and Applications — PoS(X LASNPA) (2014).

[37] K. Morishima et al., Nature **552** (2017).

[38] K. N. Borozdin et al., Nature **422** (2003).

[39] W. C. Priedhorsky et al., Review of Scientific Instruments **74** (2003).

[40] G. Hogan et al., Proceedings of the 1999 Particle Accelerator Conference (Cat. No.99CH36366) ().

[41] N. King et al., Nuclear Instruments and Methods in Physics Research Section A: Accelerators, Spectrometers, Detectors and Associated Equipment **424** (1999).

[42] F. E. Merrill, Reviews of Accelerator Science and Technology **08** (2015).

[43] F. E. Merrill et al., Applied Physics Letters **112** (2018).

[44] S. Pesente et al., Nuclear Instruments and Methods in Physics Research Section A: Accelerators, Spectrometers, Detectors and Associated Equipment **604** (2009).

[45] M. Bogolyubskiy et al., 2011 IEEE Nuclear Science Symposium Conference Record (2011).

[46] J. Armitage et al., International Journal of Modern Physics: Conference Series **27** (2014).

[47] G. Russo et al., Journal of Instrumentation **9** (2014).

[48] K. Gnanvo et al., Nuclear Instruments and Methods in Physics Research Section A: Accelerators, Spectrometers, Detectors and Associated Equipment **652**, Symposium on Radiation Measurements and Applications (SORMA) XII 2010 (2011).

[49] S. Bouteille et al., Nuclear Instruments and Methods in Physics Research Section A: Accelerators, Spectrometers, Detectors and Associated Equipment **834** (2016).

[50] P. Baesso et al., 2012 IEEE Nuclear Science Symposium and Medical Imaging Conference Record (NSS/MIC) (2012).

[51] L. Schultz et al., Nuclear Instruments and Methods in Physics Research Section A: Accelerators, Spectrometers, Detectors and Associated Equipment **519** (2004).

[52] D. Mitra et al., 2009 IEEE Nuclear Science Symposium Conference Record (NSS/MIC) (2009).

[53] M. Stapleton et al., Journal of Instrumentation **9** (2014).

[54] S. Riggi et al., Nuclear Instruments and Methods in Physics Research Section A: Accelerators, Spectrometers, Detectors and Associated Equipment **728** (2013).

[55] L. Schultz et al., IEEE Transactions on Image Processing **16** (2007).

[56] M Benettoni et al., Journal of Instrumentation **8** (2013).

[57] E. Åström et al., Journal of Instrumentation **11** (2016).

[58] *Scanning and Imaging Shipping Containers Overseas: Costs and Alternatives* (Congressional Budget Office, 2016).

[59] P. Baesso et al., Journal of Instrumentation **9** (2014).

[60] V. Antonuccio et al., Nuclear Instruments and Methods in Physics Research Section A: Accelerators, Spectrometers, Detectors and Associated Equipment **845** (2017).

[61] K. Borozdin et al., Physical Review Letters **109** (2012).

[62] J. Perry et al., Journal of Applied Physics **113** (2013).

[63] H. Fujii et al., Progress of Theoretical and Experimental Physics **2013** (2013).

[64] X. Hu et al., ISIJ International **58** (2018).

[65] J. M. Durham et al., AIP Advances **5** (2015).

[66] E. Guardincerri et al., AIP Advances **6** (2016).

[67] E. Guardincerri et al., Philosophical Transactions of the Royal Society A: Mathematical, Physical and Engineering Sciences **377** (2019).

[68] E. Guardincerri et al., Nuclear Instruments and Methods in Physics Research Section A: Accelerators, Spectrometers, Detectors and Associated Equipment **789** (2015).

[69] C. Morris et al., *A new method of passive counting of nuclear missile warheads -a white paper for the Defense Threat Reduction Agency*, tech. rep. (2015).

[70] M. Tanabashi et al., Physical Review D **98** (2018).

[71] C. L. Morris et al., Reports on Progress in Physics **76** (2013).

[72] E. Guardincerri et al., Pure and Applied Geophysics **174** (2017).

[73] G. Saracino et al., Philosophical Transactions of the Royal Society A: Mathematical, Physical and Engineering Sciences **377** (2019).

[74] H. A. Bethe, Phys. Rev. **89** (1953).

[75] B. Rossi et al., Rev. Mod. Phys. **13** (1941).

[76] L. Eyges, Phys. Rev. **74** (1948).

[77] G. R. Lynch et al., Nuclear Instruments and Methods in Physics Research Section B: Beam Interactions with Materials and Atoms **58** (1991).

[78] Y.-S. Tsai, Rev. Mod. Phys. **46** (1974).

[79] C. L. Morris et al., AIP Advances **2** (2012).

[80] C. L. Morris et al., Nuclear Instruments and Methods in Physics Research Section B: Beam Interactions with Materials and Atoms **330** (2014).

[81] D. Reyna, arXiv e-prints, hep-ph/0604145 (2006).

[82] B. C. Nandi et al., Journal of Physics A: General Physics **5** (1972).

[83] C. A. Ayre et al., Journal of Physics G: Nuclear Physics **1** (1975).

[84] R. G. Kellogg et al., Phys. Rev. D **17** (1978).

[85] S. Tsuji et al., Journal of Physics G: Nuclear and Particle Physics **24** (1998).

[86] H. Jokisch et al., Phys. Rev. D **19** (1979).

[87] S. Matsuno et al., Phys. Rev. D **29** (1984).

[88] E. V. Bugaev et al., Phys. Rev. D **58** (1998).

[89] P. Grieder, *Cosmic Rays at Earth* (Elsevier Science, 2001).

[90] J. Radon, Ber. der Sachische Akademie der Wissenschaften **69** (1917).

[91] A. M. Cormack, Journal of Applied Physics **34** (1963).

[92] A. M. Cormack, Journal of Applied Physics **35** (1964).

[93] G. N. Hounsfield, The British Journal of Radiology **46** (1973).

[94] J. Ambrose, The British Journal of Radiology **46** (1973).

[95] M. Goitein, Nuclear Instruments and Methods **101** (1972).

[96] E. V. Benton et al., Science **182** (1973).

[97] A. C. Kak et al., *Principles of Computerized Tomographic Imaging* (Society for Industrial and Applied Mathematics, 2001).

[98] S. Kaczmarz, Bulletin International de l'Académie Polonaise des Sciences et des Lettres **35** (1937).

[99] EPRI, *The MC-10 PWR spent-fuel storage cask - testing and analysis, project 2406-4 : interim report*, English, tech. rep. (1987).

[100] J. M. Durham et al., Journal of Nuclear Materials Management **44** (2016).

[101] J. M. Durham et al., Phys. Rev. Applied **9** (2018).

[102] S. Agostinelli et al., Nuclear Instruments and Methods in Physics Research Section A: Accelerators, Spectrometers, Detectors and Associated Equipment **506** (2003).

[103] O. Sorkine et al., Proceedings of the Fifth Eurographics Symposium on Geometry Processing, SGP '07 (2007).

[104] D. Poulson et al., Nuclear Instruments and Methods in Physics Research Section A: Accelerators, Spectrometers, Detectors and Associated Equipment **842** (2017).

[105] *Software Distributed by Functional Imaging*, `http://cfi.lbl.gov/software/`.

[106] J. D. Galloway et al., JNMM-Journal of the Institute of Nuclear Materials Management **40** (2012).

[107] D. Poulson et al., Philosophical Transactions of the Royal Society A: Mathematical, Physical and Engineering Sciences **377** (2019).

[108] INTERNATIONAL ATOMIC ENERGY AGENCY, *IAEA Safeguards Glossary*, International Nuclear Verification Series 3 (INTERNATIONAL ATOMIC ENERGY AGENCY, Vienna, 2002).

[109] M. A. McKinnon et al., *Testing and analyses of the TN-24P PWR spent-fuel dry storage cask loaded with consolidated fuel*, tech. rep. (1989).

[110] M. Kojo et al., Progress in Nuclear Energy **52** (2010).

[111] M. Brantberger et al., Swedish Nuclear Fuel and Waste Management Co. Report R-06-34.

[112] D. Bennett et al., Journal of Nuclear Materials **379** (2008).

[113] L. Cederqvist et al., *Design, production and initial state of the canister*, tech. rep. (Swedish Nuclear Fuel and Waste Management Co., 2010).

[114] Y. Benhammou et al., 2011 IEEE Nuclear Science Symposium Conference Record (2011).

[115] J. Perry, "Advanced applications of cosmic-ray radiography", PhD thesis (2013).

[116] S. Chatzidakis et al., Journal of Applied Physics **123** (2018).

[117] C. L. Morris et al., Science & Global Security **16** (2008).

[118] H. Li et al., Proceedings, The Twentieth National Conference on Artificial Intelligence and the Seventeenth Innovative Applications of Artificial Intelligence Conference, July 9-13, 2005, Pittsburgh, Pennsylvania, USA (2005).

[119] Z. Liu et al., IEEE Transactions on Image Processing **28** (2019).

[120] C.-A. C. Fekete et al., Physics in Medicine and Biology **60** (2015).

[121] U. Schneider et al., Medical Physics **22** (1995).

[122] D. C. Williams, Physics in Medicine and Biology **49** (2004).

[123] T. Li et al., Medical Physics **33** (2006).

[124] R. W. Schulte et al., Medical Physics **35** (2008).